Electronic Thesis and Dissertation Repository

10-6-2017 2:30 PM

Metal Sulfides as Anode for Lithium Ion and Sodium Ion Battery

Ali Abdulla, *The University of Western Ontario*

Supervisor: Andy (Xueliang)Sun, *The University of Western Ontario*
A thesis submitted in partial fulfillment of the requirements for the Master of Engineering
Science degree in Mechanical and Materials Engineering
© Ali Abdulla 2017

Recommended Citation

Abstract

Nanomaterials have been studied intensively in the last decades due to their unique physical and chemical properties and their potential for applications in different domains. Among these applications, energy storage has become the center of focus by many research groups and companies to develop high efficiency and reliable energy devices such as the commercial lithium-ion batteries (LIBs). However, LIBs has not yet met the growing requirements of the high demand for increasing energy density. More efforts are requested to improve the performance of the batteries by designing better electrode materials and increasing the battery safety. Another type of batteries has emerged such as sodium ion batteries(SIBs) that tends to have bright future for large-scale energy applications due to its low cost.

In this thesis, different types of Metal-Organic Frameworks (MOFs) including Zeolitic Imidazolate Framework-8 (ZIF-8) and (ZIF-67) and Materials from Institute Lavoisier (MIL-88) are synthesized. Meanwhile, the morphologies and structures of MIL-88 have been optimized and defined through adjusting the hydrothermal process and the effects of different parameters such as process time, and temperature, solvent type, reactant concentration, and additives on the physical and chemical characteristics are also investigated.

Furthermore, carbon coated cobalt sulfides derived from MOFs is studied for the application of anode in lithium ion batteries (LIBs) and sodium ion batteries (SIBs). This high surface area, high porosity, and good electric conductivity material show high specific capacity results as an anode in LIBs and SIBs. Physical and chemical characterization is also conducted to investigate the materials' properties. The material shows very high structural integrity during the synthesis process.

Other metal sulfides such as are synthesized using MOFs templates and further studied for batteries applications. ZnS exhibited high performance as anode for LIBs and SIBs by delivering high specific capacity and stable cycling performance

Keywords: Metal-Organic Framework, Metal Sulfides, Anode, Lithium-Ion and Sodium Ion Battery

Co-author statement

Chapter 1:

Title: Literature Review of Transition Metal Sulfides for Lithium-ion and Sodium-ion Battery Applications

Authors: Ali. Abdulla, Yang. Zhao, Keegan. Adair, Xueliang. Sun

Ali Abdulla designed and wrote the chapter and made the discussion

Yang Zhao helped to design the chapter and made discussion during chapter writing and revision the chapter.

Keagan Adair revised chapter writing.

Xueliang Sun is the supervisor guided the organization and revision of the whole story.

Chapter 3:

Title: Fabrication of Different Types of Metal-Organic Frameworks

Authors: Ali. Abdulla, Yang. Zhao, Yulong. Liu, Jianneng. Liang, Ruying. Li, Xueliang. Sun

Ali Abdulla designed and carried out all the experiments, collected and analyzed the data, and wrote the chapter.

Yang Zhao helped designing experiments, collecting and analyzing the data and made discussion during the chapter.

Xueliang Sun the supervisor guides the experiment, designed the whole story and revised the chapter and gave the funding.

Yulong Liu did XRD tests and helped to analyze the data.

Jianneng Liang did XRD tests and helped to analyze the data.

Ruying Li helped to do experiments.

Chapter 4:

Title: Carbon coated Cobalt Sulfide for LIBs and SIBs Anode material

Authors: Ali. Abdulla, Yang. Zhao, Xia. Li, Zhongxin. Song, Yulong. Liu, Ruying. Li, Xueliang. Sun

Ali Abdulla designed experiments, collected the data, wrote the chapter and made discussion in the chapter.

Yang Zhao helped designing experiment, helped to analyze the data, made discussion and revised the chapter.

Xueliang Sun the supervisor guided the experiment, designed the whole story and revised the chapter and gave funding.

Yulong Liu did XRD tests and helped to analyze the data.

Xia Li carried out the BET test.

Zhongxin Song did Raman spectra.

Ruying Li helped to do experiments.

Chapter 5:

Title: Metal sulfides derived from MOFs: synthesis, characterization, electrochemical performances.

Authors: Ali. Abdulla, Yang. Zhao, Yulong. Liu, Jianneng. Liang, Ruying. Li, Xueliang. Sun.

Ali Abdulla designed and carried out all the experiments, collected and analyzed the data, and wrote the chapter.

Yang Zhao helped designing experiments, collecting and analyzing the data and made discussion during the chapter.

Xueliang Sun the supervisor guides the experiment, designed the whole story and revised the

chapter and gave the funding.

Yulong Liu did XRD tests and helped to analyze the data.

Jianneng Liang did XRD tests and helped to analyze the data.

Ruying Li helped to do experiments.

Dedication

I would like to dedicate my thesis to my family who gave me their limitless love and support during my study.

Acknowledgments

This work would not have been possible without the unlimited support from the people and organizations that I am about to acknowledge humbly

First of all, I would like to show my sincerest thanks and gratefulness to my thesis supervisor professor. Xueliang (Andy) Sun, for giving me the opportunity to be involved in such fantastic learning experience. His guidance through my research with all enthusiasm, immense knowledge, passion, and fantastic personality helped me go through this research. A student could not have asked for a better supervisor.

My special thanks to my mentor, Yang Zhao, who trained me from the very beginning of nanomaterials synthesis, characterizations, and teamwork. He has been through my whole work step by step. His knowledge, limitless patience, and support helped me to learn a lot of new techniques and concept. He stepped with me from the very first moment into my research, and whenever I had asked for help from him, he was there with all kindness and passion. I wish him the very best and success in his life.

Many thanks to Mrs. Ruying (Kathy) Li, who was there when I needed anything in the labs for experiments and always made sure that I have it. She is very kind, and knowledgeable person who also love to help others. She was always a mom to our group by showing her care and love. I am so grateful to you for being a part of this work.

I would like to thank all my group members, the ones who are still working and studying to accomplish their goals and the others who already graduated before I finished and left to pursue their dreams. They have always been helpful and provided a conducive and friendly environment for research. Thank you all, and I wish them all the very best in their lives.

I would like to take this opportunity also to show my sincere appreciation to my supervision committee Prof. Jun Yang for being there I needed his support. I would like to express my gratefulness and pleasure to the examiner including prof. George Knopf, Prof. Jeffrey Wood, and Dr. Mihnea Ioan Ionescu for taking time and giving the effort to look at this thesis and take a part of the examination.

I could not find the proper words to describe how blessed I am to have my family giving me their unlimited love and support. My dear Parents who always encourage me to pursue my dreams and provided me the whole support I needed since I came to this life. Thank you for being there for me, and I wish that I could pay back what you have given me of the immense support.

My thanks to my brother and sisters who for their care and love during studying abroad and I wish them all the best and success in their studies and lives.

I will not forget to take the chance to thank all my friends here and back home in Libya for their love and cheers. Also, special thanks to my roommate Ali Fouad for being fantastic friend and brother during this journey since the first day I came to Canada.

I am so grateful to the Ministry of Higher Education in Libya for giving this golden opportunity to pursue my master degree by giving me this fantastic scholarship and funding. I am grateful to the University of Benghazi who was the main reason to be here by nominating me in the first place for this scholarship program.

I own my sincere acknowledgment to the Natural Science and Engineering Research Council of Canada (NSCRC), and General Motors (GM). My thanks to the Mechanical and Materials Engineering department at Western University for giving this opportunity to pursue my Master's degree in such high ranked, professional and advanced scientific castle.

Finally, I would like to thank everyone who supported me through my study and was part of making this dream come true.

Table of Content

List of Tables

List of Figures

List of Abbreviations

2D- Two Dimensional

3D- Three Dimensional

ALD- Atomic Layer Deposition

B- Bulk

BET- Brunauer, Emmett, And Teller

CTAB- Cetyltrim Ethyl Ammonium Bromide

CV- Cyclic Voltammetry

CVD- Chemical Vapor Deposition

DEC- Diethyl Carbonate

DEGDME- Diethylene Glycol Dimethyl ether

DMF- Dimethylformamide

DPC- Dodecahedral Porous Carbon

EC- Ethylene Carbonate

EDS- Energy Dispersive X-Ray Spectrometry

EIS- Electrochemical Impedance Spectroscopy

EM- Ethyl Methyl Carbonate

FL- Few-Layer

GNs- Graphene Nanosheets

GO- Graphene Oxide

HRTEM- High-Resolution Transmission Electron Microscopy

NSs- Nanospheres

LTMS- Layered Transitional Metal Sulfides

MIL-88- Materials from Institute Lavoisier

MLD- Molecular Layer Deposition

MOFs- Metal-Organic Frameworks

MTMOs- Mixed Transition Metal Oxides

MTMSs- Mixed Transition Metal Sulfides

MWCNTs- Multi-Walled Carbon Nanotubes

NC- Nitrogen-Doped Carbon Coating

NCs- Nanocrystals

NG- N- Doped Graphene

NWs- Nanowires

OLA- Oley amine

ORR- Oxygen Reduction Reaction

PC- Porous Carbon ()

PEDOT- Poly (3,4-Ethylenedioxythiophene

PEO- Poly (Ethylene Oxide)

PNAI- Polyaniline

PTFE- Polytetrafluoroethylene

PVP- Polyvinyl Pyrrolidone

RGO- Reduced Graphene Oxide

SC- Core-Shell

SEI- Surface-Electrolyte Interphase

SEM- Scanning Electron Microscopy

SWCNTs- Single-Walled Carbon Nanotubes

TEM- Transmission Electron Microscopy

TGA- Thermogravimetric Analysis

XRD- X-Ray Diffraction

ZIF-67- Zeolitic Imidazolate Framework-67

ZIF-8- Zeolitic Imidazolate Framework-8

Chapter 1 Introduction

1. Introduction

Today's society need for energy is growing significantly in a way that alert the research to look at different sources of energy not only because of the limited conventional resources which is mainly fuel but also the considerable risk that our planet is going to in the long-term. Significant effort has been made to take advantage of many clean energy resources that are provided by nature such as solar, wind, and electrical vehicle which will reduce the negative impact of the greenhouse gas emissions. These different types of energy cannot be use unless a reliable storage device for clean energy storing is available. Lithium-ion battery (LIBs) has high capacity, high energy density and long recharging life, and this reliable battery has been commercialized by Sony in 1991. LIBs mainly consists of four main parts which are positive electrode (cathode), negative electrode (Anode), liquid electrolyte as ions medium and separator. These parts have been intensively studied for development; unfortunately, none has met the requirements for large energy consumption applications and there is still massive room for more enhancement. Graphite as commercial LIBs anode has very stable potential and long cycling life, however, its low capacity and safety problems grew concerns of whether it can meet the development of LIBs and the new energy density targets. Other challenge regarding the lithium-ion battery supply in the future. Lithium element has a limited abundant on earth and with the rapid growth of energy consumption, it is expected that lithium-ion battery fabrication cost is going to significantly jump up in the near future. This problem has raised a question about looking for alternative battery and research have come with different new systems such as sodium ion battery, lithium sulfur, sodium sulfur, lithium air, and sodium-air. Sodium ion battery has drawn great attention due to the high sodium abundant. Also, sodium ion system is similar to lithium-ion battery in terms of principle of work. However, it has its own problems. Sodium atom is very big in compare to lithium atom which need a material with excellent structural properties to host the sodium atoms during electrochemical process. Metal sulfides is among many materials have been studied for energy application as anode material

hosting charging lithium and sodium atoms. Metal sulfides has high capacity and unique structural characteristics that are desirable in energy applications.

It is imperative to know properties such as high capacity, electric and electronic conductivity, high surface area, and chemical and physical stability that should be investigated when looking for a material as anode for battery applications. Hence, metal organic framework is one of these materials that have a unique properties and meet anode materials requirements. Metal-organic frame (MOF) work is a combination of metal ions linked by organic ligands owing crystal structure with high porosity. This material has very unique properties such as the nearly highest surface area material has been reported as well as the wide range of different structures and metals. These attractive properties render this material and their derivatives for many applications among them chemical separation, filtering, sensing, energy storage and conversion, and catalysis. One of the common applications of MOFs is the energy storage and conversion mainly for batteries. This field has become very hot area of research due to the urgent need to reliable storage device for clean energy storing. Lithium-ion, sodium ion, and lithium-sulfur batteries have employed the MOFs for their electrodes and it shewn very promising potential. However, poor conductivity of MOFs is one of the challenges in this area. Many strategies have been investigated in order to improve MOFs conductivity by doping techniques such as N or C doping. Another way is to synthesis nanocomposites of MOF and Carbon materials including nanotubes(CNTs), Graphene(G), or Reduced Graphene Oxides (RGO) etc.

In this research, several kinds of MOFs materials are studied for better understanding of the properties and moving forward to exploit these characteristics for battery applications. Using MOFs materials as a template to design metal sulfide is the second step where the properties of both will be obtained in one material. Moreover, investigating the challenges after obtaining metal sulfide from MOFs template is also planned and will be stated in the thesis objectives in details.

Thesis Objectives

The challenges in the LIBs and SIBs applications were reviewed and highlighted where they could be overcome by designing better anode materials. MOFs was studied as

the promising materials with unique properties such as high specific area, tunable porosity, and controllable structures. The recent development and understanding of metal sulfides with the designed nanostructure, mainly derived from MOFs, were also reviewed and considered a strong candidate as anode material for LIBs and SIBs. However, the challenges remained in term of relatively large volume change and low conductivities. Among the potential approach, the carbon coating is beneficial to address the issues of low conductivity as anode applications for LIBs and SIBs. Another strategy is to design nanostructured materials facing one of the significant problems of volume expansion. The specific objectives are the following.

(1) Different types of MOFs have been synthesized, and the physical and chemical properties of them have been further investigated. Moreover, the morphologies and structures of MIL-88 have been optimized through the hydrothermal process in detail.

 (2) ZIF-67 was used as a template to fabricate the carbon coated cobalt sulfides with unique structures. Furthermore, the physical and chemical properties have been carried out. When used as anode materials for both LIBs and SIBs, as-prepared carbon coated cobalt sulfides show high capacity and stable cycling performances.

(3) Other types of metal sulfides, including zinc sulfides, tin sulfides, and iron sulfides have been synthesized by the wet chemical method and CVD method using ZIF-8, Tin-MOFs, and MIL-88 as a template. The electrochemical properties including the cycling performances and rate performances of all these metal sulfides are also evaluated.

Thesis Organization

This thesis includes six chapters and satisfies the requirements for "Integrated-Article form" as outlined in the Thesis Regulation Guide by the School of Graduate and Postdoctoral Studies (SGPS) of the University of Western Ontario. Specifically, the thesis is organized as follows:

Chapter 1 gave literature reviews of lithium-ion batteries and sodium ion batteries including the working principle, recent development, and challenges that currently render their developments and applications. Recent progress of metal sulfides as anode materials was summarized in detail. Different approaches to resolve the challenges facing metal sulfides in

batteries applications are highlighted. The conclusion and future perspective of the development of these materials are stated.

Chapter 2 listed different synthesis method and characterization techniques used in this thesis. Electrochemical evaluation devices and techniques are presented as well.

Chapter 3 presented the synthesis process of ZIF-8 and ZIF-67. Moreover, the hydrothermal process of MIL-88 is optimized, and the effect of different parameters on the structure are studied in detailed. Finally, a brief conclusion and the achievements and challenges are emphasized.

Chapter 4 described an approach to developed cobalt sulfides with carbon coating derived from MOFs as anode materials for LIBs and SIBs. This approach delivered a material with unique properties and structure, which was investigated by using several characterization techniques. It was discovered that $C@Co_9S_8$ possess high surface area and porosity and stable thermal stability. Excellent electrochemical performances represented that the $C@Co_9S_8$ is a promising anode material for LIBs and SIBs.

Chapter 5 studied three types of metal sulfides, including Zinc, Tin, and Iron sulfides, as anodes for LIBs and SIBs. Synthesis processes and physical characterization was performed to investigate the morphology and confirm the structure. It was found that ZnS delivered promising electrochemical performance as an anode in LIBs and SIBs.

Chapter 6 summarized the results, draw a conclusion of the whole work and highlighted the potential future directions of the future work that required in this field.

Chapter 2

2. **Literature Review of Transition Metal Sulfides for Lithium-ion and Sodium-ion Battery Applications**

Abstract

This chapter is a literature review of Transition metal sulfides (TMSs) and their applications in lithium-ion batteries (LIBs) and sodium ion batteries (SIBs). TMSs including CoS_x, FeS_x, MoS_2, SnS_x, WS_2, et al. have recently attracted significant attention in the applications of high-performance LIBs and SIBs. Originating from their high theoretical capacity, various structures, and limited volume expansion compared to the conventional metal oxide and alloys, TMSs are believed to be an optimistic alternative to the traditional electrode materials. Recent developments in the tional design of novel micro/nanostructured TMSs for LIBs and SIBs are summarized in this chapter, and their energy storage mechanisms are compared to metal oxide anodes. In particular, the significant effects of the TMSs morphology, micro/nanostructure, and crystallinity on battery performance are highlighted. Furthermore, the future trends and prospects, as well as potential problems, are presented to further develop advanced TMSs anodes for promising and large-scale commercial LIBs and SIBs applications.

Note: This chapter will be submitted as a review paper: Ali Abdulla, Yang Zhao, Xueliang Sun, entitled: A Comprehensive Review of Transition Metal Sulfides for Lithium-ion and Sodium-ion Battery Applications

2.1. Introduction

The global energy shortage and environmental issues have led to rapidly increasing requirements for highly efficient sources of clean energy, such as solar, wind power and biomass [1]. Therefore, the development of novel energy storage and conversion systems is urgently required for efficient utilization of renewable energy [2]. Lithium-ion batteries (LIBs) are one of the best developed and commercialized battery technologies for portable electronic devices such as laptops, mobile phones, medical devices, and electric vehicles. They possess various outstanding features, including high energy density, no memory effect, low maintenance and low self-discharge [3, 4]. At present, the energy density of commercial LIBs is less than 200 Wh kg^{-1}, which is insufficient for the growing energy demands of emerging technologies. One of the primary methods to achieve higher energy densities is to explore new electrodes materials with high reversible capacities and excellent stability. The typical cathode and anodes materials used in modern LIBs are lithium cobalt oxide ($LiCoO_2$) and graphite, respectively, as shown in **Figure 2.1a**. In the case of anode materials, graphite has distinct advantages such as low cost, long lifetime and high stability. However, its low theoretical capacity of 372 mAh g^{-1} and low Li-ion transport rate limits its further applications [5]. Therefore, a great deal of research has been carried out to explore alternative materials to replace graphite as potential anodes for LIBs. Different types of materials have been investigated such as novel carbon nanomaterials (carbon nanotube, graphene, mesoporous carbon, et al.), alloy materials (Si, Sn, P, et al.), metal oxides (SnO_x, transition metal oxide, et al.) and metal sulfides.

Meanwhile, it has been claimed that alternative battery technologies should be explored due to the expected shortage and high cost of lithium shortly. Among these new systems, sodium-ion batteries (SIBs) have received significant attention due to the abundance and low cost of sodium resources for large-scale energy storage applications. SIBs are very similar to LIBs regarding working principle and chemical reactivity, and even share similar electrode materials (**Figure 2.1b**). However, the relatively low energy density and large size of sodium ions (55% larger than Li$^+$) contribute to the severe challenges to overcome to improve the electrochemical performances of anode and cathode materials in SIBs. Graphite serves as the typical anode material for LIBs. However, it is unsuitable for sodium ion intercalation due to the insufficient interlayer spacing [6]. Thus, the development of novel anode materials for SIBs is still an ongoing challenge, and more work is required before commercialization.
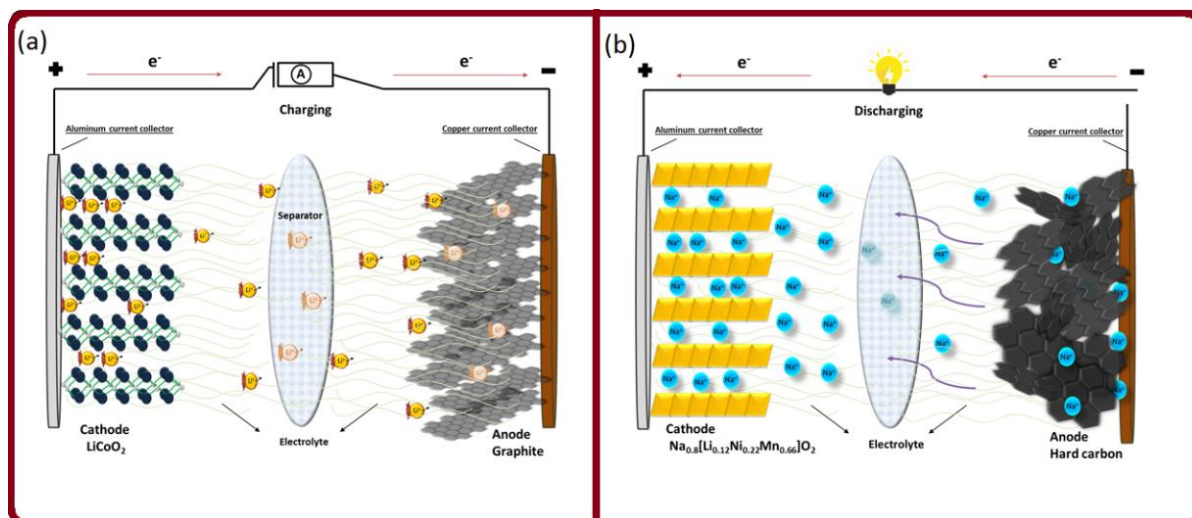
Figure 2-1 Schematic diagrams of (a) a lithium-ion battery and (b) a sodium-ion battery.

2.2. Transition Metal Sulfides

As discussed above, one of the critical components of LIBs and SIBs is the choice of electrode materials. Various materials have been studied as anodes according to their electrochemical and physical properties (specific capacity, chemical, and thermal stability, electronic and ionic conductivity, et al.). Since graphite is insufficient for the advancement of high energy density LIBs and incapable of employment in SIBs, other types of anode materials have been explored as an alternative such as novel carbon nanomaterials, metal oxides and alloys, phosphates and sulfides [7-12]. Among these candidates, transition metal sulfides (TMSs) have been widely studied for batteries applications due to their high capacity, several structures, and relatively low volume expansion compared to the traditionally used metal oxides and alloys [13]. Although TMS have higher reaction voltages compare to metal oxides as shown in **Figure 2 (a, b)**, they can be matched to cathodes with high reaction voltage to maintain or improve the energy density of the battery [14]. However, TMSs suffer from issues such as poor cycling performance resulting from the volume expansion and low conductivity. Another problem is the dissolution of polysulfide in the electrolyte which can form passivating layers on the surface leading to low ion transfer kinetics[15]. In this case, various strategies have been developed to solve these problems including surface modifications, the design of novel nanostructures and development of new synthetic routes.

Due to the promising properties of TMSs, significant efforts have been made to explore these hot materials. **Figure 1.2 (c, d)** shows the publication numbers (based on a web of science) of TMSs in the application of batteries (**Figure 1.2c**) and other areas (**Figure 1.2d**). It can be seen that the number of publications on TMS has experienced rapid growth over the last six years. Recently, there have been several review papers published on TMS focusing on specific aspects, such as hollow structures or LIBs and supercapacitors applications [16-18]. Unfortunately, few review papers make a comprehensive summary and comparison of TMSs for the application of both LIBs and SIBs in detail. Therefore, a comprehensive review of the recent achievements and development of TMSs as anodes for both LIBs and SIBs is urgently required to accelerate further improvement and application of these types of anode materials. Furthermore, the comprehensive comparison of TMSs for both LIBs and SIBs is an exciting topic for the future direction of different batteries systems, even for other applications. By this motivation, this review mainly focuses on the different kinds of TMSs employed as anode materials for both LIBs and SIBs. Particularly CoS_x, FeS_x, MoS_2, SnS_x, and WS_2 and their Li/Na-storage mechanisms, synthesis methods, reasonable structure design, and strategies for addressing the issues that have arisen.
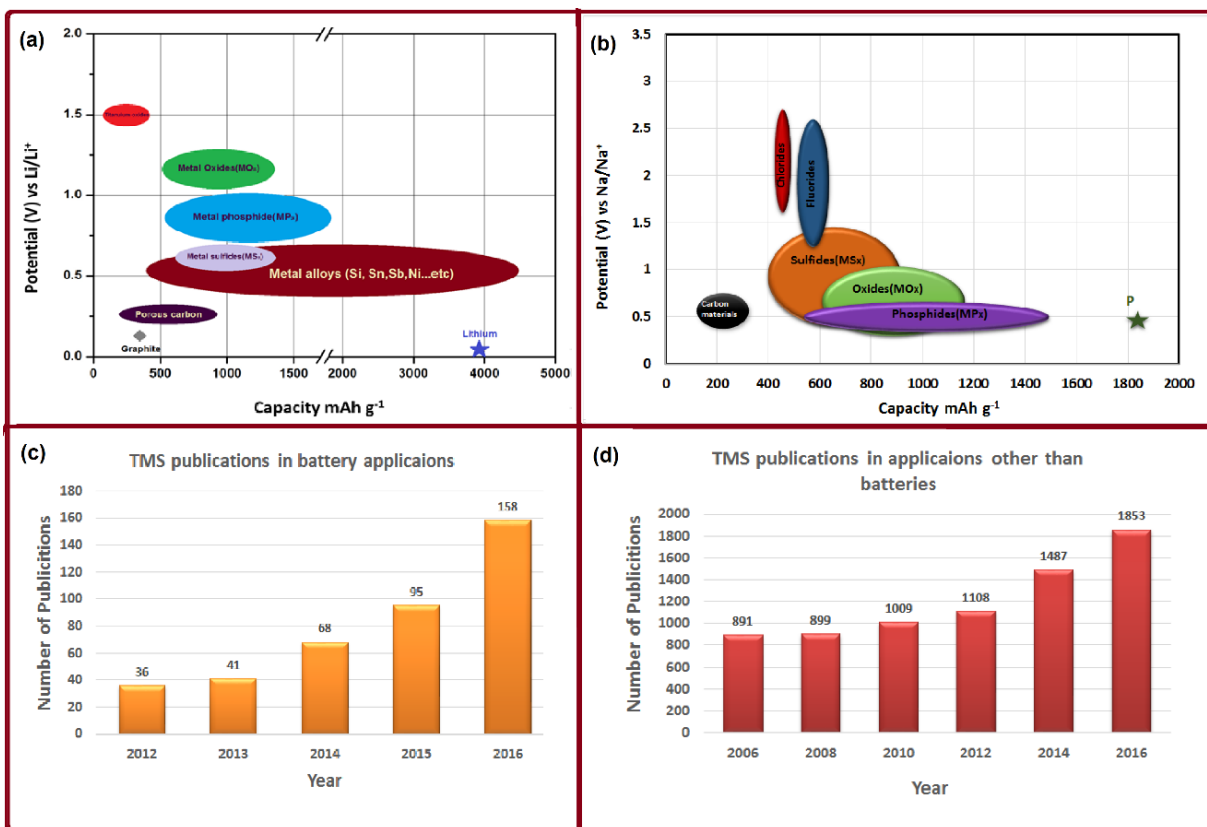
Figure 2-2 Voltage *vs.* capacity for anode materials have been investigated for the next generation of rechargeable (a) Li-ion battery (b) Na-ion battery. Schematic charts show the

number of scientific reports published during the last six years on metal sulfides (c) in batteries applications (d) in different applications analyzed from the Web of Science.

2.2.1. Lithium/Sodium Storage Mechanism of TMSs

TMSs can be classified into two groups according to their crystal structures and reaction mechanism with Li^+ or Na^+. One type of TMS is the typical conversion anode materials or non-layered TMSs, such as the sulfides of Co, Fe, Ni, Zn, Cu, and Mn, which possess various morphologies and chemical structures. Another type is the layered transitional metal sulfides (LTMS), including MoS_2, SnS_x, ZrS, VS_x, and WS_x. These kinds of LTMSs are composed of two-dimension (2D) layered structures in which the metal atoms are located in between two hexagonal chalcogenide layers occupying either octahedral or octahedral interstitial sites.

The reaction mechanisms of conversion anode materials for TMSs have been understood with their electrochemical behavior, in which the M corresponds to Co, Fe, Ni, Zn, Cu, and Mn. In the application of both LIBs and SIBs, at the initial charge cycle, Li_xMS_2 will be formed resulting from the intercalation of Li^+ ions into MS_2 followed by further decomposition into $2Li_2S$ and M. Then a reversible conversion reaction between M and Li_2S is maintained in the following processes. Similar mechanism proceeds in SIBs in which sodium ions will react with MS_2 to form Na_xMS_2, which further reacts with Na to produce $2Na_2S$ and M, which will be carried out in the following charge/discharge process. The conversion reactions in LIBs/SIBs during charging/discharging can be generalized as follow[17]:

$$MS_2 + xLi\ (Na) \rightarrow Li_xMS_2\ (Na_xMS_2) \tag{1}$$

$$Li_xMS_2\ (Na_xMS_2) + (4-x)\ Li\ (Na) \rightarrow M + 2Li_2S\ (Na_2S) \tag{2}$$

$$M + 2Li_2S\ (Na_2S) \leftrightarrow M + 2S + 4Li\ (Na) \tag{3}$$
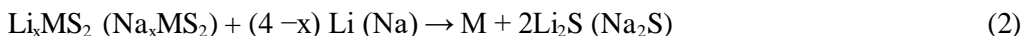
However, LTMS have been considered as a favorable electrode material for batteries delivering excellent cycling performance. The structure of LTMSs has the unique advantage in which the layers are conjoined by weak Vander Waals force[19]. Therefore, guest ions (Li^+ or Na^+) can undergo reversible insertion in between the layered structure of LTMS [17]. However, the vast volume expansion of MS_x during a complete charge transfer as a result of reducing M^{4+} to M^{3+}, along with Li^+/Na^+ ion diffusion in the van der Waal's gap is the challenge needed to be solved. **Table 2.1**. Below show different metal sulfides reported in the literature and their theoretical capacities based on information from references and some were calculated.

Table 2-1 **Calculation of the theoretical capacities of metal sulfides for LIBs and SIBs**

Element	Theoretical capacity in LIB mAh g^{-1}	Number of transferring moles of electron Li$^+$	Ref	Theoretical capacity in SIBs mAh g^{-1}	Number of transferring moles of electron Na$^+$	Ref
Bi_2S_3	625.64	12e$^-$	[20]	625.64	12e$^-$	[21]
CoS	589.08	2e$^-$	[22]	589.08	2e$^-$	[23]
CoS_2	871.21	4e$^-$	[24]	871.21	4e$^-$	[25]
Co_3S_4	703.	8e$^-$	[26]	-	-	
Co_9S_8	544.96	16e$^-$	[27]	544.96	16e$^-$	[23]
CuS	560.75	2e$^-$	[28]	-	-	
FeS	609.86	2e$^-$	[29]	-	-	
FeS_2	893.76	4e$^-$	[30, 31]	893.76	4e$^-$	[32, 33]
Fe_3S_4	770.32	8.5e$^-$	[34]	-	-	
Fe_7S_8	662.47	16e$^-$	[34]	-	-	
$GaS_{1.2}$				-	-	
Ga_2S_3	1137.66	10e$^-$	[35]	-	-	
MnS	615.91	2e$^-$	[36, 37]	615.91	2e$^-$	[36]
MoS_2	669.88	4e$^-$	[38]	669.88	4e$^-$	[39]
$NiS_{1.03}$	584.56	2e$^-$	[40]	-	-	
NiS_2	873.07	4e$^-$	[41]	-	-	
Ni_3S_2				446.40	4e$^-$	[42, 43]
Ni_3S_4	704.69	8e$^-$	[40]	-	-	
Ni_7S_6				533.27	12e$^-$	[42]
Sb_2S_3	473.4 - 946	3-6e$^-$	[44]	946.97	12e$^-$	[45]
SnS	782.3-1138	2-6.4e-	[46]	728.51	15e$^-$	[47]
SnS_2	645.1-1231.7	4 - 8.4e$^-$	[48, 49]	846.91	3.75e$^-$	[50, 51]
VS_4	1196.8	8 e$^-$	[52]	299.2	2e$^-$	[53]

WS$_2$	432.4	4e$^-$	[54]	108.1-432.4	1-4 e$^-$	[55, 56]
ZnS$_2$	550.19-	2e$^-$	[57]	550.19	2e$^-$	[58]

2.3. TMSs application in LIBs and SIBs

2.3.1. Cobalt Sulfide Co$_x$S$_y$

Cobalt sulfides are one of the most widely studied TMSs due to their high capacity, controllable structure, and rich variety of stoichiometric compositions such as CoS, CoS$_2$, Co$_3$S$_4$, and Co$_9$S$_8$. They have been explored for use in many applications, including water splitting catalysis [59], electrocatalysis for oxygen reduction reaction [60], dye-sensitized solar cells [61, 62]. Also, these materials are widely studied as electrode materials for energy storage [13] in lithium-ion batteries [63-68], sodium-ion batteries [69, 70] and supercapacitors [71-73]. However, the primary challenges faced by cobalt sulfide-based electrodes can be divided into the categories of (1) significant volume expansion, (2) low conductivity and (3) dissolution of the polysulfide in organic electrolytes [27, 74, 75].

Several approaches have been developed to solve these problems of TMSs, such as the design of hollow nanostructures, which has been applied for other types of anode materials like metal oxides and alloys. It is believed that the hollow inner can provide a void space which can accommodate the volume expansion of metal sulfides and improve the Li$^+$ access by decreasing the ion diffusion path length [11, 76-78]. For example, Jin et al. reported hierarchical worm-like CoS$_2$ assembled by ultrathin nanosheets with high conductivity synthesized through a solvothermal route. The as-prepared CoS$_2$ delivers a high reversible capacity of 883 mAh g^{-1} at a current density of 100 mA g^{-1} after 100 cycles. It was also shown to yield a capacity of 501 mAh g^{-1} even at a high current density of 2000 mA g^{-1} [79]. Another unique mesoporous hollow Co$_9$S$_8$ nanospheres have been synthesized by similar solvothermal reaction followed by sintering process [80]. When applied for LIBs, the reversible capacity increased to as high as 1414 mAh g^{-1} after 100 cycles at 100 mA g^{-1} after initial capacity fading during the first 15 cycles. This capacity recovery was attributed to the pseudo-capacitive behavior of a gel-like polymer layer that occurs during cycling at a voltage range of 0.01-1.4V. For the rate capability, this hollow spheres also show high reversible capacities of 904, 810, 751, 699, 635 and 426 mAh g^{-1} at a current density of 0.1, 0.2, 0.5, 1, 2 and 5 A g^{-1} respectively. Furthermore, a thin layer of carbon coating has been applied on

the Co_9S_8 nanospheres which leads to an enhanced capacity of 896 mAh g^{-1} after 800 cycles at a current density of 2 A g^{-1}, indicating that the carbon coating can accommodate the volume change effects on the structure and provide a highly reversible lithiation/delithiation process for long cycling life in addition to improving conductivity. Therefore, hollow structured materials are in favor for battery applications due to there high accessibility to the electrolyte and useful capability to mitigate volume expansion by providing more space while hosting the charging ions.

Conductive coatings or nanocomposites with different nanocarbon can be utilized to increase the conductivity of cobalt sulfides, and enhance the electrochemical performance. Peng et al. reported the synthesis of hierarchical CoS_2 hollow nanospheres (HSs) with a nitrogen-doped carbon coating (NC@CoS_2) via a simple solution-based method [81]. The electrochemical performances demonstrate that the ultra-thin layer of NC favorably plays a crucial role in improving the electrochemical performance of the NC@CoS_2 HSs. It provides short Li$^+$ diffusion length and more structural stability by attributing to the particle protection against the volume expansion, enhancing the electric conductivity. Finally, NC layer can have a positive effect on reducing the polysulfide dissolution into the electrolyte. Three samples were used with the different amount of the additive for best results which were donated as NC@CoS_2-1, NC@CoS_2-2, and NC@CoS_2-3 based on 0.06, 0.03, and 0.09 g of PVP, respectively. As a result, after 100 cycles, NC@CoS_2-1 shows a high reversible capacity of 657.2 mAh g^{-1}, while NC@CoS2-2 can deliver only a relatively low capacity of 537.2 and 467.5 mAh g-1, and NC@CoS_2-3, respectively; **see Figure 2.3.I and m**.
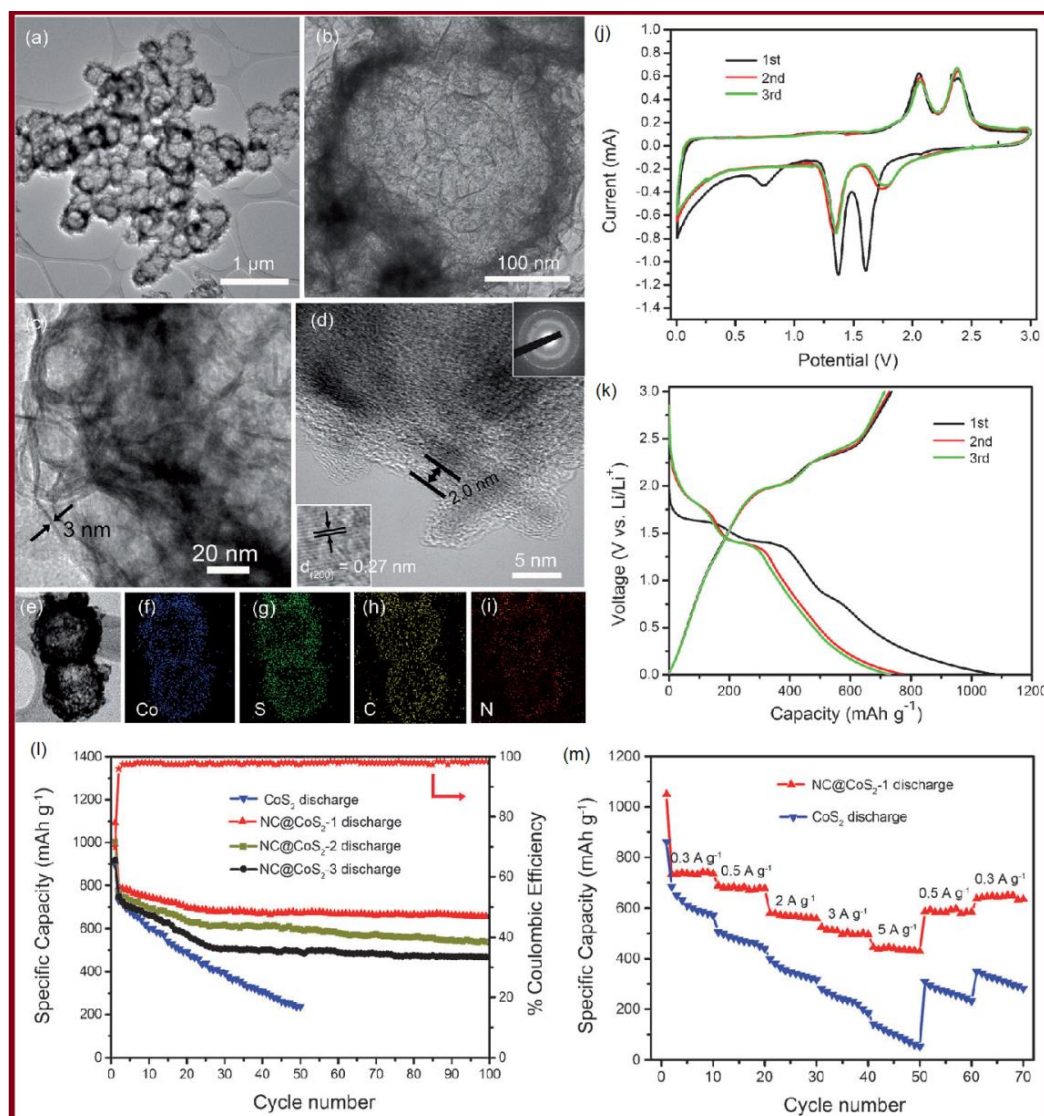
Figure 2-3 (a)–(c) TEM and (d) HRTEM images of NC@CoS$_2$-1 with the inset image displaying the SAED pattern of NC@CoS$_2$-1; (e) TEM image of NC@CoS$_2$-1; corresponding EDX elemental mappings of: (f) Co, (g) S, (h) C, and (i) N for NC@CoS$_2$-1.(j) Representative CV spectra of NC@CoS$_2$-1 for the first three cycles at a scan rate of 0.1 mV s^{-1} between 0.005 and 3 V; (k) discharge/charge voltage profiles of NC@CoS$_2$-1 for the first three cycles; (l) comparative cycling performance of NC@CoS$_2$-1, NC@CoS$_2$-2, NC@CoS$_2$-3, and CoS$_2$ at a current density of 200 mA g^{-1}; (m) cycling stabilities of NC@CoS$_2$-1 and bare CoS$_2$ at various current densities[81].

In addition to carbon coatings, MWCNTs have been further introduced as a conductive matrix to fabricate MWCNTs@C@Co_9S_8 nanocomposites [65]. The rationally designed nanocomposites indicate high stability with a capacity of 662 mAh g^{-1} after 120 cycles at the high current density of 1 A g^{-1} and excellent rate performance while surprisingly the electrode performs exceptional long cycling life with a reversible capacity of ~1065 mAh g^{-1} after 700 cycles at a current density of 2A g^{-1}. The capacity restoration in the extended cycling is attributed to the structural reinforcement, and the reactivation of the active materials   Another outstanding performance was obtained from MOF derived hollow cobalt sulfide electrode synthesized through the wet chemical process[66]. This design has high structural stability due to the excellent interaction between the CNTs and hollow cobalt sulfide because of which the electrode maintained stable cycling performance was delivered a high discharge capacity of ~937 mAh g^{-1} after 160 cycles and the structure architectures successfully contribute to accommodating the volume change during cycling.

Graphene, as a novel 2D nanomaterial [82, 83], has been widely studied in various applications, such as water purification[84], biomedical[85, 86], solar cells, fuel cells, photoelectrochemical, photocatalysis [87, 88], and energy storage and conversion devices [89-92], due to its high electrical conductivity, thermal conductivity, high surface area, etc. In this case, it has been considered as the promising candidates as conductive additives for metal sulfides. Typically, a cobalt sulfide/graphene nanosheets (GNS) composite containing several phases of CoS, CoS_2, and Co_9S_8 are manufactured via a one-pot solvothermal route [93]. After 50 cycles, the as-prepared nanocomposites retain a reversible capacity of 954 mAh g^{-1} at a current density of 100 mA g^{-1}, which is considerably improved over that of bare cobalt sulfide (359 mAh g^{-1}). Another interesting 2D structure has been reported by Du et al., in which porous Co_3S_4 nanosheets were inserted into flexible layered graphene sheets via a simple freeze-drying process and subsequent treatment with hydrazine [64]. This rationally designed material demonstrates high performance with a capacity of 710 mAh g^{-1} at a current density of 0.5 A g^{-1} after 200 cycles and excellent rate capabilities as well. The significant functions of graphene or reduced graphene oxide have been widely proven to be performance enhancing additives for electrode materials in the applications of LIBs and SIBs. Our previous review has also summarized the crucial roles of graphene for tin-based anode materials in LIBs [94]. As the similar concept for cobalt sulfides, the electron transfer rate, electronic conductivity and charge mobility of cobalt sulfides can be enhanced significantly. The high surface area of graphene leads to a greater extent of electrolyte access and shorten the lithium-ion diffusion path during cycling. Additionally, the volume expansion is expected to be accommodated by the high flexibility of graphene which aids in cycling stability and performance.

Metal-organic frameworks (MOFs) are considered as active templates for the fabrication of nanomaterials with controlled structure, high surface area, and high conductivity [8]. In our previous review, we pointed out the unique properties of MOFs, and it used as an excellent template to produce metal oxide or mix transition metal oxide. Among the many types of MOFs, Co-based structures such as ZIF-67 (Co) has also been used as the template for the synthesis of porous carbon/cobalt sulfide composites [95]. **Figure 2.4 (a-c)** shows the schematic diagram of the synthesis of MOF-derived cobalt sulfide and its morphology. Two different samples are synthesized based on the type of carbon matrix used in the composite where the first C/CoS_2 composite with bulk carbon matrix is marked as BC/CoS_2 -650, which is synthesized by replacing Nano ZIF-67 precursors with bulk crystals and the second C/CoS_2 composite marked as NC/CoS_2 -1000 with larger CoS_2 particles is prepared by increasing the carbonization temperature to 1000 °C. Electrochemical cycling and rate performance in comparison with other two cobalt sulfides composites are demonstrated in **Figure 2.4 (d, e)**. NC/CoS_2-650 can successfully deliver capacities of 560 mAh g^{-1} and 410 mAh g^{-1} after 50 cycles at current densities of 100 mA g^{-1} and 2500 mA g^{-1}, respectively which is attributed to the structure reliability of the inside CoS_2 nanoparticle, presence of the carbon matrix that provide sufficient space to contain the volume expansion and finally is that the polysulfide effect is eliminated by the presence of abundant N in the material.
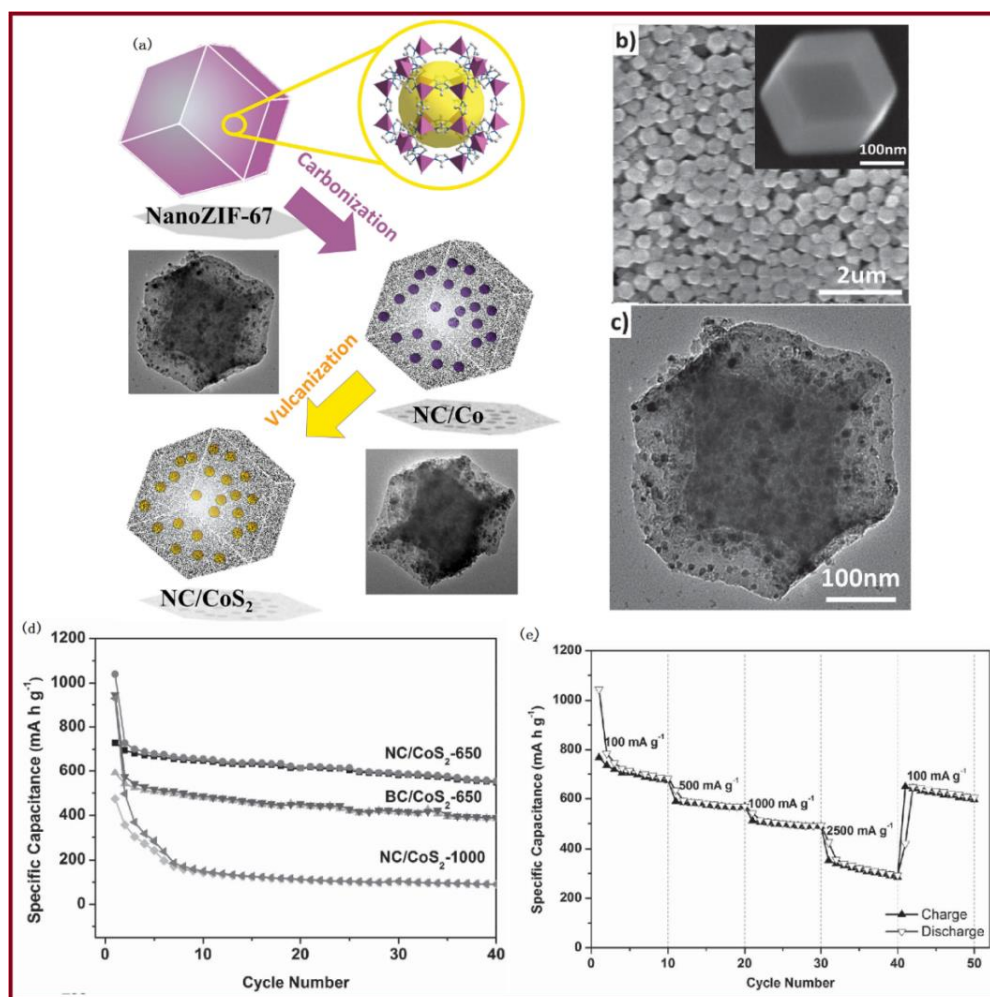
Figure 2-4 (a) Schematic illustration of the synthesis of ultra-small CoS_2 nanoparticles in N-rich carbon. (b) SEM images of NanoZIF-67. (c) Transmission electron microscopy. (d) Cycle-life performances of NC/CoS_2-650, NC/CoS_2-1000, and BC/CoS_2-650 at 500 mA g^{-1}. (e) charge/discharge capacity at various current densities of NC/CoS_2 -650[95].

Cobalt sulfide composites derived from MOFs have been further studied for application in SIBs. Recently, Zhang et al. reported the synthesis of a 3D core-shell cobalt sulfide/dodecahedral porous carbon (cs-Co_xS_y/DPC) using ZIF-67 as a template [23]. A high initial discharge capacity of 600 mAh g^{-1} can be achieved at a current density of 0.5 A g^{-1}. However, it rapidly decays to around 380 mAh g^{-1} in the second cycle as a result of surface-electrolyte interphase (SEI) formation. Moreover, this material exhibits a reversible capacity of 300 mAh g^{-1} after 50 cycles and excellent rate performance which may be attributed to the high structure porosity which facilitates Na^+ diffusion in addition to the high flexibility of the carbon to accommodate volume expansion. MOFs

are desirable materials for energy storage applications due to their intrinsic porosity, high surface area, and tunable structures. Well defined nanostructured materials can facilitate the Li^+/Na^+ diffusion kinetics and increase the electrolyte accessibility, thus leading to stable cycling performance and structural stability.

As mentioned in the first section, the size of sodium ions is 55% larger than that of a lithium ion, which leads to more challenging in developing suitable anode materials capable of reversible sodiation. Sufficient space for reversible intercalation and control over volume expansion is a required property for electrode candidates in SIBs. Therefore, the exploration of the proper material that can successfully avoid these problems is an ongoing process and has been carried out by many research groups. Emphasising and improving the chemical and mechanical stability, the conductivity of the anode material and more importantly the structural capability to contain sodium ions without losing the active material due to the volume change is currently the focus of research [96, 97]. The same materials of Co_3S_4 porous nanosheets that mentioned in the above LIBs application. It also shows promising results in SIBs, which delivered a capacity of 329 mAh g^{-1} after 50 cycles at 0.5 A g^{-1} and rate performances of 423, 353, 307, 237, and 154 mAh g^{-1} at the current density of 0.5, 1, 2, 5, and 10 A g^{-1}, respectively[64]. Another sandwich-like cobalt sulfide–reduced graphene oxide (CoS/rGO) composite has been fabricated through hydrothermal method [98]. When applied as an anode in SIBs, it shows enhanced performance which retains a capacity of 230 mAh g^{-1} at a current density of 100 mA g^{-1} after 100 cycles while the bare CoS is fading from 601 mAh g^{-1} in the 1st cycle to 68 mAh g^{-1} in 40 cycles (See **Figure 2.5**). This shows the impact of the graphene oxide composition on the performance improvement and stability of CoS which offers structure flexibility to accommodate the volume change and further pulverization in the active material nanostructure. Another phase of Co_9S_8 based composites have been reported by Ko et al. via a one-pot spray pyrolysis process [99]. It was found that the as-prepared Co_9S_8-carbon composite obtains a capacity of 404 mAh g^{-1} after 50 cycles at a current density of 0.5 A g^{-1}. Furthermore, when increasing the current into 1.5 A g^{-1}, a capacity of 326 mAh g^{-1} is maintained. Another typical research reported the design of CoS_2/multi-walled carbon nanotube (MWCNT) nanocomposite using hydrothermal method [69] by Shadike and colleagues. They demonstrate the improvement of the anode performance in SIBs in both ether-based electrolyte ($NaCF_3SO_3$-DGM electrolyte) and carbonate-based electrolyte ($NaClO_4$-EC/PC electrolytes) [69]. The electrode exhibits a capacity of 568 mAh g^{-1} in the ether-based electrolyte while maintained a capacity of 411 mAh g^{-1} in carbonate electrolytes at current density 100 mA g^{-1} after 100 cycles. Rate test results display that CoS_2-MWCNT obtained better performance in the ether-based electrolyte than in the carbonate-based electrolytes indicating the advantage of using the ether-based electrolyte in

Na–FeS$_2$ system. This work demonstrates the effective contribution of CNTs additives to the electrode materials for buffering volume change and increase the reversible capacity also states that ether based has lower potential to react with possible sodium polysulfide products which negatively could affect the cycling performance.
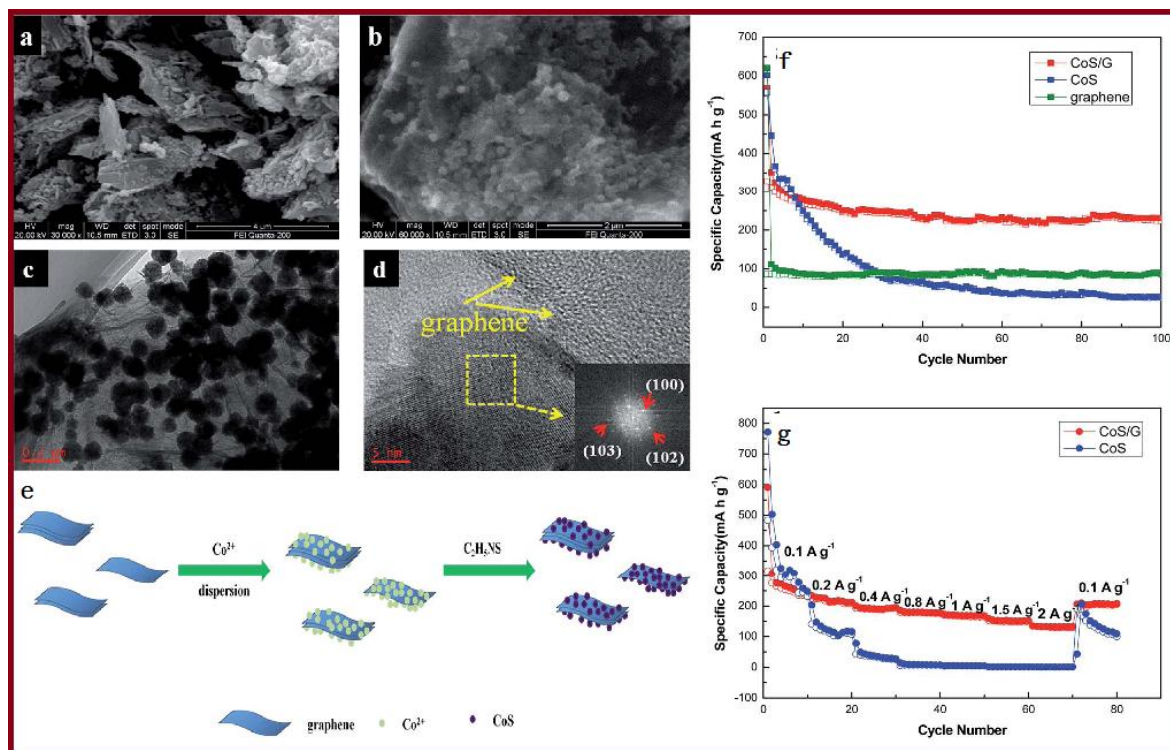
Figure 2-5 SEM (a and b), TEM (c) and HRTEM (d) images of CoS/rGO, the insets of HRTEM (d) show the corresponding FFT pattern of CoS/rGO. (e) Schematic illustration of the formation of CoS/rGO composite. (f) Cycling performance of CoS, graphene and CoS/rGO electrodes at 0.1 A g^{-1} for 100 cycles, respectively; (g) rate performance of CoS and CoS/rGO electrodes[98].

Briefly, cobalt sulfide in the application of LIBs and SIBs has been summarized in detail in this section. Its high specific capacity and stable structure have drawn high attention for LIBs and SIBs especially in the anode, but the low electrical conductivity and slow ionic diffusion in their bulk forms lead to poor lithium/sodium storage performance. In particular, different CoS, CoS$_2$, Co$_3$S$_4$, and Co$_9$S$_8$ have been widely studied in the literature, and some average performances are listed in **Table 2.2 a and b** for both batteries[100]. Theoretically, CoS$_2$ indicates the highest theoretical capacity of 871.21mAh g^{-1}for LIBs and SIBs. Meanwhile, in the reported literature, Co$_9$S$_8$ shows the best excellent performances for LIBs and SIBs. The reasons can be explained as

tends to have larger surface area and pore size distribution that facilitate the electrolyte accessibility and Li^+/Na^+ ions insertion. Also in the hollow structure design, Co_9S_8 demonstrates better electrochemical performance than CoS_2 that could be attributed to the conductive paths provided by the structure which eventually results into better Li^+/Na insertion/ desertion. Co_3S_4 is barely reported for LIBs and SIBs while it is more reported in other application such as supercapacitors and oxygen reduction reaction (ORR) [101-104]. Therefore, three main strategies were mainly adopted to overcome the challenges that face the development of cobalt sulfides. Firstly, designing some unique TMS nanostructures (hollows, core shells, and polyhedral) with high porosity and small particle sizes could improve the Li^+ or Na^+ mobility during cycling and deliver better stability. Secondly, Co_xS_y derived from MOF are scarcely investigated although it has indicated interesting results due to the unique characteristics of MOFs such as the high surface area, porosity, and conductivity and because of which it is considered as a desirable candidate for energy storage applications. Finally, Co_xS_y/carbon composites and coatings have been widely reported for both batteries, and it is a useful treatment to buffering the volume change of cobalt sulfides by providing additional spaces and flexibility for expansion.

2.3.2. Iron sulfide FeS_x

Compared with cobalt, iron (Fe) shows more advantages including low toxicity, low cost and high abundance in the earth's crust. In battery applications, Fe-based anodes exhibit promising properties, such as lower operating voltages and higher energy density [105]. Similarly, different stoichiometry and crystal structures are determined by the proportion of sulfur such as troilite-FeS, greigite-Fe_3S_4, and pyrite-FeS_2. **Figure 2.6** shows the range of theoretical and practical capacities for different phases of iron sulfide based on previously reported literature. Amongst the iron sulfides, pyrite-FeS_2 is one of the most widely studied phase owing to its high theoretical capacity of 893 mAh g^{-1}. Like other metal sulfides, FeS_x also suffers from substantial volume changes and low conductivity. The volume expansion has an adverse effect on the electrochemical performance, often leading to an irreversible structural collapse and detachment of active materials, which results in reduced cycling stability [106].
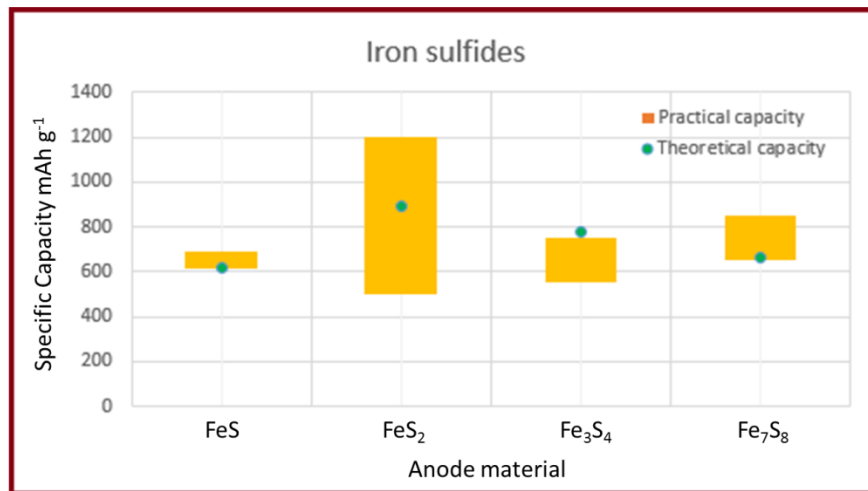
Figure 2-6 Schematic charts for iron sulfides theoretical and practical capacities.

To increase the conductivity of FeS_x, the most common strategy employed is a coating or combining the active material with carbon nanomaterials such as carbon nanotubes or graphene[107]. To show the benefits of this approach, Liu et al. reported a low-temperature approach to derive a carbon encapsulated spherical Fe_7S_8 nanocrystals with a core-shell structure (Fe_7S_8@C) composite [108]. The Fe_7S_8@C electrodes retain a capacity of 815 mAh g^{-1} after 50 cycles at 200 mA g^{-1} and good stability at higher rates with capacities of 850, 735, 693, 629, 583 mAh g^{-1} at current densities of 200, 813, 1425, 1967, 2284 mA g^{-1}; respectively. This high performance could be contributed to the presence of carbon that acts as a supporting structure to accommodate the volume change and improve ionic conductivity. Wen et al. reported a hydrothermal approach to synthesize a composite of FeS_2 microparticles with reduced graphene oxide (FeS_2/RGO) in four simple synthetic procedures to improve the capacity and cycling performance of the iron sulfide (Seen in **Figure** 2.**7a**) [109]. It starts with the absorption of Fe^{+3} on GO surface in the first stage to the addition of the sulfur source in the second stage. Then from a hydrothermal reaction between $(NH_2)_2CS$ and reacted with Fe^{+3} to produce small cubic FeS_2 crystals in the third stage to the final stage which is the reduction of GO to RGO and continues the growth of FeS_2. **Figure 2.7 b, c, d, and e** show the superior performance of their rational design of FeS_2/RGO composite in comparison with FeS_2/RGO mixture, pure RGO, and pristine FeS_2. The hybrid materials deliver a capacity of 1101.41 mAh g^{-1} after 60 cycles while capacities of 584.42 (FeS_2/RGO mixture), 417.25 (pure RGO) and 264.01 mAh g^{-1} (pristine FeS_2) remaining for the

other materials, respectively. It is believed that the interconnected networks are retained in FeS$_2$/RGO composite while the FeS$_2$/RGO mixture is just physically mixed by grinding the FeS$_2$ with reduced graphene oxide. The correlation between FeS$_2$ particles and RGO sheets as a result of the hydrothermal reaction is more functional for effectively improving the electrochemical performances. Another interesting design is reported by Xue's group to synthesize RGO-wrapped FeS$_2$ microspheres through a one-step solvothermal method [110]. The as-prepared FeS$_2$/rGO exhibited a capacity of 970 mAh g^{-1} after 300 cycles at a current density of 890 mA g^{-1}. Also, high capacity of 237 mAh g^{-1} at a high current of 20 A g^{-1} and impressive cycling performance with 380 mAh g^{-1} capacity retention after 2000 cycles at 10 C was obtained. The excellent electrochemical performance of RGO (graphene) modified FeS$_2$ composites refers to i) a thin layer of graphene can effectively prevent the dissolution of polysulfide in the electrolyte which results in poor cycling and rate capability; ii) RGO (graphene) plays a key role in offering high flexibility to the composite which can effectively enhance structural stability and prevent cell failure caused by extreme volume expansions.
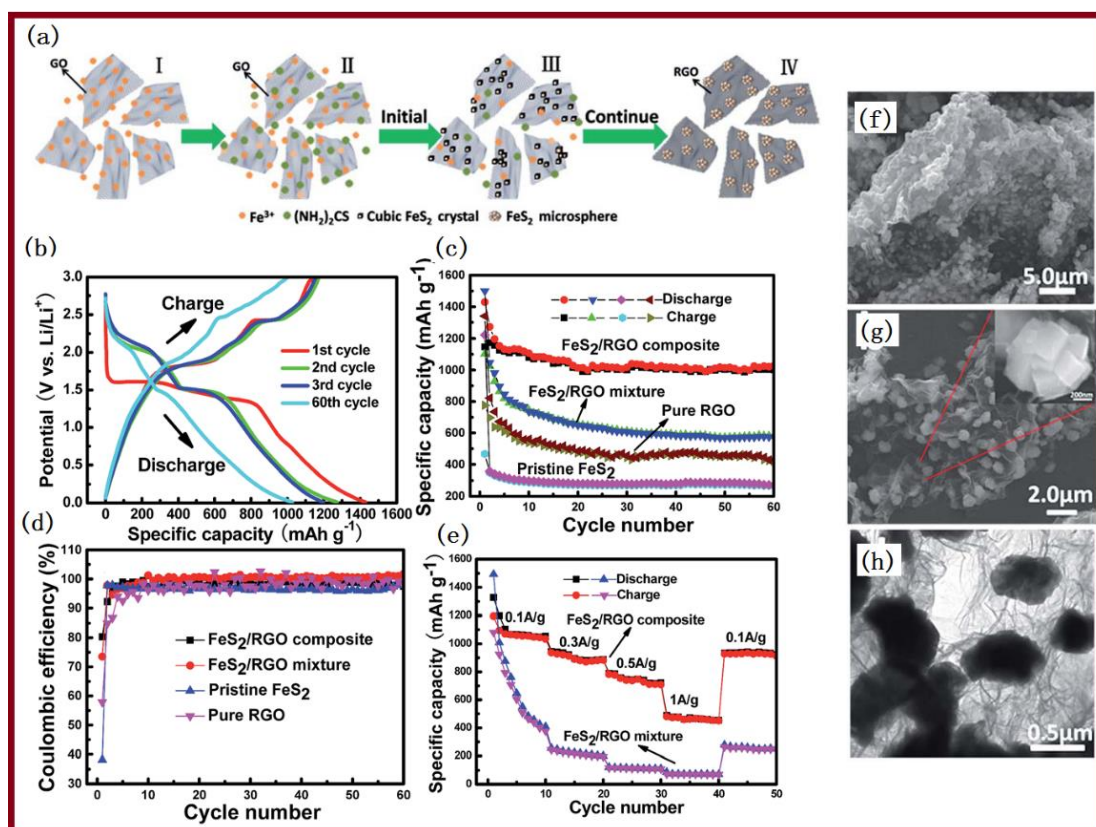
Figure 2-7 Scheme (a) the illustration of the formation of the FeS$_2$/RGO composite. (b) charge and discharge curves of the FeS$_2$/RGO composite at a current density of 100 mA g^{-1}, (c) cycling performance and (d) coulombic efficiencies of pristine FeS$_2$, pure RGO,

FeS$_2$/RGO mixture and FeS$_2$/RGO composite at a current density of 100 mA g^{-1}, and (e) rate performance of the FeS$_2$/RGO mixture and the FeS$_2$/RGO composite at different current densities. (f and g) SEM images of the FeS$_2$/RGO composite, (h) TEM image[111].

Exerting control over structural properties such as surface area, porosity and morphology have proven to be another favorite method to develop high-performance active materials. For instance, Xia and co-workers reported the synthesis of FeS$_2$ nanocrystals with particle sizes of 10 to 35 nm via a hydrothermal method [30]. After 40 cycles, the two FeS$_2$ NC-based electrodes retain a reversible capacity of about 427 mAh g^{-1} whereas pyrite FeS$_2$ microparticles FeS$_2$ MPs electrode retain a reversible capacity of 154 mA h g^{-1}. The nanocrystals yielded better electrochemical performance compared with microparticles which highlight the effect of the structure-function by Liu et al. [112]. They used a solvothermal route to design pyrite FeS$_2$ nanocubes, and this material was tested for LIBs anode where satisfaction results were obtained. This cubic structure owned a particle size of around 80-120 nm and exhibited a capacity of 540 mAh g^{-1} at a current density of 1 A g^{-1} after 150 cycles. Even increasing current density into 5 A g^{-1}, it still can maintain discharge capacity of 220 mAh g^{-1} which is claimed to be as a benefit to the high surface area of the pyrite FeS$_2$, small particle size and the uniform distribution of particles in the structure. Pyrite FeS$_2$ was also synthesized via a solvothermal method and used as the anode in LIBs system with ether-based electrolyte [113]. It is claimed that carbonate-based electrolytes have a negative impact on the performance of the pyrite. Therefore, an ether-based electrolyte was used for this investigation and yielded a high efficiency by providing more active sites for interaction between the electrolyte and the polysulfide. FeS$_2$ microspheres exhibited a capacity of 680 mAh g^{-1} at 100 mA g^{-1} and even at a high current density of 1000 mA g^{-1}, the electrode performs a columbic efficiency of 90% after 100 cycles.

Zheng et al. reported the synthesis of hollow Fe$_3$S$_4$ nanostructures with uniform structure and porosity through a simple approach (see **Figure 2.8**) [114]. Their work demonstrated the use of hollow nanostructured Fe$_3$S$_4$ for electrochemical energy storage and water treatment applications. The novel material delivered a capacity of 750 mAh g^{-1} after 100 cycles at a current density of 0.2 A g^{-1} which can be attributed to the structure that offers short diffusion paths and facilitates the intercalation of Li$^+$. Also, the rate capability of this material was tested and maintained capacities of 510, 390, 320 and 250 mAh g^{-1} at current densities of 0.2, 0.5, 1 and 2 A g^{-1}, respectively.
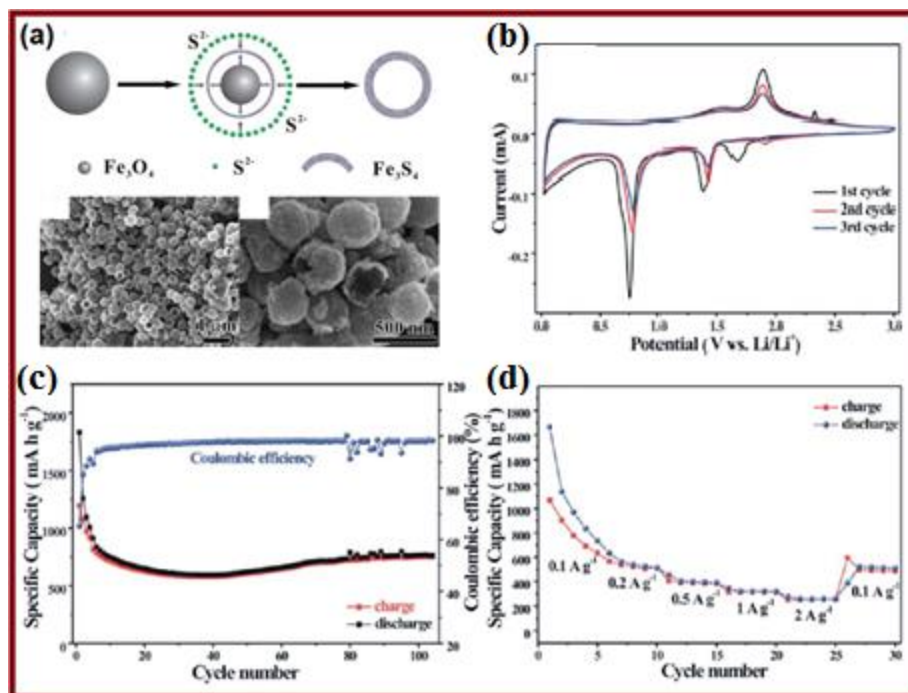
Figure 2-8 (a) Synthesis schematic of Fe_3S_4 hollow spheres and SEM images of the Fe_3S_4. (b) the first three consecutive cyclic voltammograms at a scan rate of 0.05 mV s^{-1}; (c) cycling performance and coulombic efficiency at a current density of 0.2 A g^{-1} at room temperature; (d) rate performance according to the cycling rate sequence: 0.1, 0.2, 0.5, 1, 2 and 0.1 A g^{-1}[114].

Application of iron sulfides as anode materials in SIBs have been scarcely explored, although early results show great promise for the use of TMSs in these systems. Designing new nanostructured materials with unique physical and electrochemical properties is of the utmost importance for future energy storage applications. For example, Li and co-workers successfully reported a reversible self-assembly method to control the design of FeS_2 nanocrystals. They indicate that the concentration of iron precursor is a critical factor in the final structure of the pyrite, where an increased concentration of precursor yields dendritic pyrite nanocrystals (nanodendrites), whereas decreasing the concentration leads to nanocubic structures [115]. Hu et al. used a hydrothermal method to synthesis pyrite microspheres to be applied as an anode material in sodium ion batteries [116]. Interestingly, this material proved very high stability for a long cycling lifetime which could maintain a capacity of around 200 mAh g^{-1} for 20 000 cycles at a high current density of 1000 mA g^{-1} and retain a columbic efficiency of 100%. The as-prepared FeS_2 has a unique morphology with a high porosity which improves the electrochemical reaction kinetics and

contributes to high cycling stability. Walter et al., reported very high-performance pyrite nanocrystals (NCs) that were synthesized through a solution-phase chemical approach [33]. FeS_2 NCs delivered capacity of over 500 mAh g^{-1} for 400 cycles at a current density of 1000 mA g^{-1} (see **Figure 2.9**). It is found that the addition of FEC to the electrolyte can contribute to an increase in the columbic efficiency from 83 to 95%. Bulk FeS_2 was tested for comparison which indicated poor cycling performance and quick capacity fading. However, it was obvious that FeS_2 NCs with small particle size, optimized shape, and surface modification showed better performance as cathode material in LIBs and as anode material in SIBs applications.
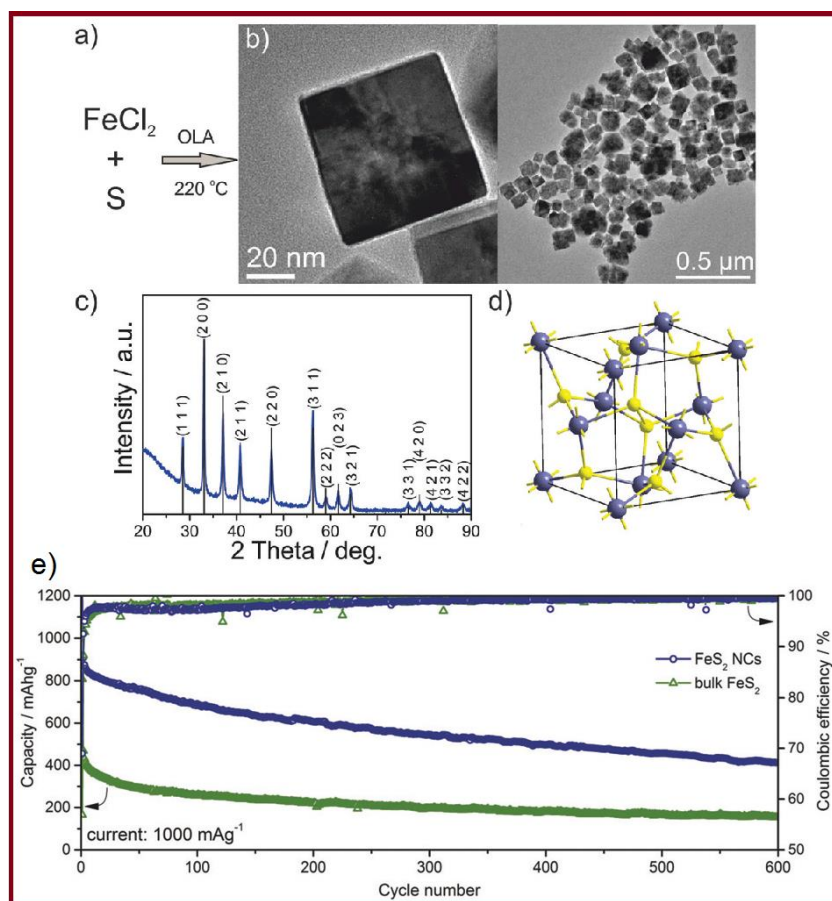
Figure 2-9 Synthesis and characterization of FeS_2 NCs: (a) reaction scheme; (b) transmission electron microscopy (TEM) images; (c) X-ray diffraction (XRD) pattern indexed to pure-phase pyrite FeS_2 (ICDD database, PDF no.: 00-071-2219; space group N205, Pa3, a = 5.4179 Å); (d) schematic representation of the unit cell of pyrite FeS_2 electrochemical performance of FeS_2 NCs tested as anode material for SIBs. (e) Capacity retention for FeS_2 NCs and bulk FeS_2[33].

To sum up, iron sulfides shows high capability for battery applications owing to its high theoretical capacity, low cost, and non-toxicity. However, the deterioration of active materials due to the volume change is a serious issue that leads to poor cycling performance, and the low conductivity of iron sulfide affect its practical application. To overcome these drawbacks, surface coating and nanocomposites of FeS_x and nanocarbons can significantly enhance the ionic conductivity and accommodate the volume change of FeS_x, especially for sodium, which has a large ion radius and has difficulty with reversible intercalation in tradition electrode materials. The fabrication of materials with high surface area and porosity has proven to be another effective strategy to improve the electrochemical performance in both LIBs and SIBs.

2.3.3. Molybdenum sulfide (MoS₂)

Molybdenum sulfide has a layered structure that is very similar to graphene in which sandwich-like Mo-S layers are adjacently connected via van der Waals interactions [117-124]. Meanwhile, it has been realized that MoS_2 is a very promising electrode material for LIBs and SIBs because of its high capacity and low reaction voltage [125, 126]. Moreover, the layer spacing of 2D MoS_2 (0.615 nm) is much larger than that of graphite (0.335 nm), which should be favorable for Li^+/Na^+ insertion. Also, the geometric construction of the MoS_2 active materials is capable of buffering the volume expansion in the intercalation processes [127]. However, poor cycling and imperfect rate capability due to the low conductivity are the most prominent obstacles that impede MoS_2 applicability in batteries. Hence, researchers are attempting to solve these issues to improve the electrochemical performance of MoS_2, and many of the most recent progress is discussed in detail the in following sections.

Many groups have explored the utilization MoS_2 in energy storage applications focusing on the design of novel nanostructured materials. Previously, template-assisted strategies for the synthesis of hierarchical MoS_2 micro boxes constructed by ultrathin nanosheets has been reported [128]. As-prepared MoS_2 micro boxes deliver an initial capacity of ~1100 mAh g^{-1} and a columbic efficiency of 98%, with capacity retention of 900 mAh g^{-1} maintained after 50 cycles at current density of 100 mA g^{-1} when cycled between 0.05 and 3.0 V. Moreover, the MoS_2 micro boxes can obtain a high discharge capacity of 700 mAh g^{-1} at a rate of 1 A g^{-1} which can be attributed to the highly active sites between the electrode and the electrolyte as a result of the high surface area of this unique structure which assists lithium ions diffusion through the ultrathin nanosheets. Ma et al. successfully report a hydrothermal method and further annealing process with the assistance of various cationic surfactants to produce few-layer molybdenum disulfide/graphene composites (FL-MoS₂/GNS) [129]. The electrochemical performance is considerably improved over that of pure

MoS_2, with the FL-MoS_2/GNS exhibiting a high reversible capacity of 1183 mAh g^{-1} and capacity retention of 101% after 100 cycles at a current density of 100 mA g^{-1} while a capacity retention of 37% and a charge capacity of 327 mAh g^{-1} is obtained by MoS_2 after 100 cycles. Furthermore, FL-MoS_2/GNS still retains a capacity of 901 mAh g^{-1} at a high current density of 1000 mA g^{-1}. **Figure 2.10a** shows the synthesis of a 3D-structured MoS_2/CNTs nanohybrid conducted by Li and co-workers [130]. The MoS_2/CNTs active material delivers an initial discharge and charge capacities of 1747 and 1460 mAh g^{-1}, respectively. Very promisingly, the high discharge and charge capacities of 1679 mAh g^{-1} and 1655mAh g^{-1} with the columbic efficiency of 96% and 113% are perfectly retained after 425 cycles (see **Figure 2.10j**), respectively. The MoS_2/CNTs is tested for rate capability as well and successfully maintained as high capacities as 1822, 791, 505 mAh g $^{-1}$ at current densities of 1, 40, 70 A g^{-1}, respectively, and even when the current density was increased to 100 A g^{-1}, MoS_2/CNTs still can deliver an unprecedented discharge capacity of 505 mAh g^{-1} (**Figure 2.10k**). It is claimed that this superior performance is a result of two factors; first, the capacity and conductivity were significantly enhanced due to the presence of CNTs which is highly conductive material and structural stability is much better leading to stable cycling was obtained. Second, this material took advantage of the high surface to volume ratio which shortens the Li^+ diffusion path and maintains long cycling performance.
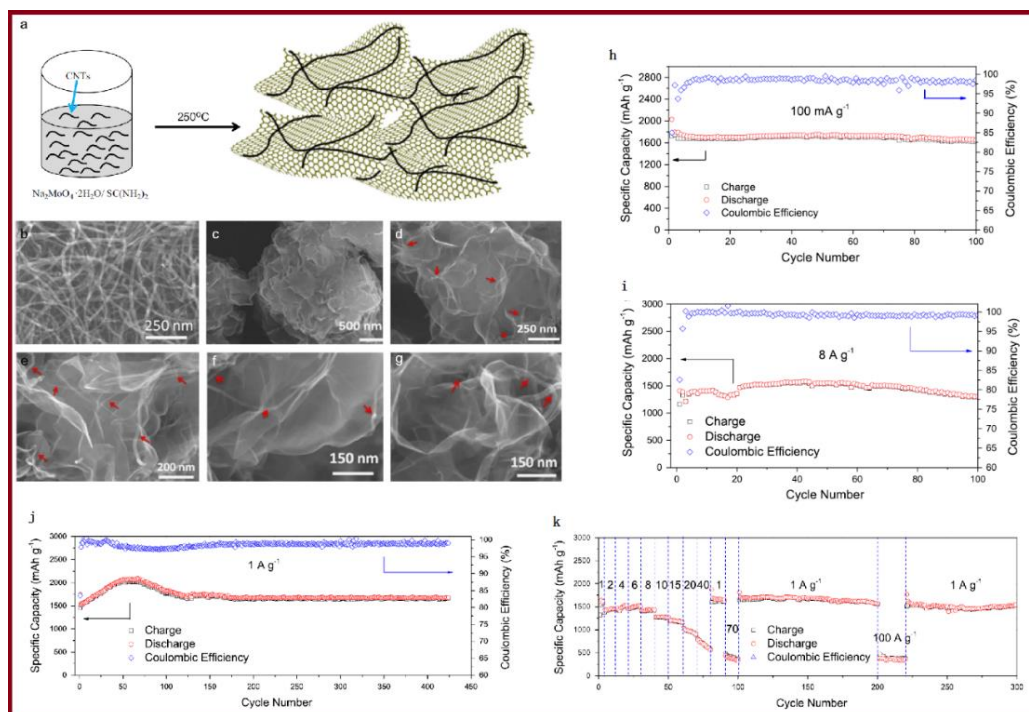
Figure 2-10 (a) Schematic illustration of synthesis process for MoS_2/CNT nanohybrid. FESEM images of (b) surface functionalized CNTs, (c) MoS_2, and (d–g) MoS_2/CNT

nanohybrid. Arrows indicate CNTs in the final product. (h–j) cycle performance of MoS$_2$/CNT nanohybrid in LIB in the same voltage range of 0.01–3.0 V at the current densities of 100mA g^{-1}, 8 A g^{-1}, and 1 A g^{-1}, (k) rate capabilities of the nanohybrid[130].

Another composite has been synthesized with flower-like molybdenum disulfide (f-MoS$_2$) hierarchical structures on a reduced graphene oxide/oxidized multi-walled carbon nanotube backbone (f-MoS$_2$/RGO/o-MWCNT), using a hydrothermal method[38]. The as-prepared composites are shown to possess excellent electrochemical characteristics with a capacity retention of 93% and reversible capacity of 1190 mAh g^{-1} after 100 cycles at a current density 100 mA g^{-1}. When the current density was increased to 250, 500, 1000, and 2000 mA g^{-1}, f-MoS$_2$/RGO/o-MWCNT exhibited specific capacities of 1095, 972 840 and 635 mAh g^{-1}, which far surpasses that of MoS$_2$/RGO and MoS$_2$/o-MWCNT. Although the active materials have some similarity in term of the composition, the vital role of the unique structure design is that it provides a short diffusion path for electrolyte ions. Hence it helps Li$^+$ fast insertion/desertion during cycling. The 3D structure high surface area contributes to more active sites and contact between the electrolyte and active materials. Also, it was claimed that the space within the structure between MoS2 and MWNCTs enables more electrolyte access to the surface of the electrode which results into stable cycling.

To further exploit the advantages of carbonaceous materials, doping techniques have emerged as an effective strategy to improve the performance of the composites using elements such as boron, nitrogen, and sulfur. Our group also designed ultrathin MoS$_2$/N-doped graphene (MoS$_2$/NG) nanosheets using this novel approach [131]. It is found that the structural stability of MoS$_2$ is improved when nitrogen-doped graphene is added which helps accommodate the volume change during the intercalation process. It is explained that MoS$_2$/NG has a high surface area and which grants access to more active sites and improves electrolyte accessibility, thereby, a significant capacity increase was observed throughout the electrochemical testing. MoS$_2$/NG delivered a capacity of 1285.3 mAh g^{-1} after 50 at a current density of 100 mA g^{-1} and high capacity of 850 mAh g^{-1} at a current density of 1 A g^{-1}.

For sodium storage, MoS$_2$ has been the most widely investigated material amongst all metal sulfides. For example, Bang et al. reported a liquid-phase exfoliation method to prepare single-layer MoS$_2$ nanosheets with high exfoliation efficiency [132]. This synthetic method delivered stable structure with satisfactory electrochemical properties for sodium storage. When cycled at a current density of 20 mA g^{-1}, the anode exhibited initial discharge and charge capacities of 254 and 164 mAh g^{-1}, respectively, followed by high coulombic efficiency over the next 100 cycles with

discharge/charge capacities of 165 and 161 mA h g^{-1}. Furthermore, a graphene-like MoS_2 nanoflower structure ($FG-MoS_2$) was synthesized through hydrothermal means was reported by Hu et al. [133]. Moreover, a well-crystallized MoS_2 ($CG-MoS_2$) was obtained after annealing the FG-MoS_2 at 700 ^oC for 3 hours, and a bulk MoS_2 sample ($B-MoS_2$) was prepared for comparison. The best cycling performance was achieved by $FG-MoS_2$, which surprisingly experienced a capacity increasing from 220 to 295 mAh g^{-1} in 300 cycles at a current density of 0.2 A g^{-1} that might refer to the expansion and exfoliation of the interlayer in which more sodium active sites are provided. Rate performance was also evaluated, and $FG-MoS_2$ showed high rate capability with capacities of 350, 300, 195 mAh g^{-1} at current densities of 0.05, 1, 10 A g^{-1}, respectively. Although this material showed better electrochemical performance when compared to $CG-MoS_2$ and $B-MoS_2$, it was noticeable that all samples demonstrated stable performance which means that MoS_2 is an inherently a suitable host material for sodium. Choi and co-workers reported the design of 3D MoS_2-graphene microspheres (3D MoS_2-G) that consist of nanospheres agglomerations via a one-pot spray pyrolysis process [134]. **Figures 2.11 a-e** show the unique structure of the obtained materials with high surface area and controlled sphere size. It is hypothesized that the presence of graphene and carbon coating can reduce the volume expansion of the MoS_2 nanospheres and further improve ionic conductivity. **Figure 2.11 g** showed the cycling performance at a current density of 200 mA g^{-1} for the 1st, 2nd and 50th cycles for the 3D MoS_2-G and crumpled MoS_2-G. It is evident that 3D MoS_2-G delivered a higher initial discharge and charge capacity of 797 and 573 mAh g^{-1}, respectively, compared to that of 415 and 511 mAh g^{-1} for the crumpled MoS_2-G, correspondingly. Also, 3D MoS_2-G showed better rate performance and long cycling life at high current of 1.5 A g^{-1} which delivered a capacity of 323 mAh g^{-1} after 600 cycles (see **Figure 2.11 h-j**). Later, Li et al. reported the use of poly(ethylene oxide) (PEO) as an intercalating agent, which acts as an additive to enhance the interlayer space of MoS_2 layers and enhances sodiation kinetics during cycling. The composite ($PEO_{2L}-MoS_2$) was synthesized via an exfoliation–restacking method to enhance the intercalation properties of MoS_2 and optimize the distance between the MoS_2 layers [135]. $PEO_{2L}-MoS_2$ demonstrated satisfiable performance for SIBs applications, delivering a capacity of 148 mAh g^{-1} after 70 cycles at a current density of 50 mA g^{-1}. Concerning the rate performance, $PEO_{2L}-MoS_2$ shows high capability with capacities of 185, 162, 143, 127 and 112 mAh g^{-1} under current densities of 50, 100, 250, 500 and 1 A g^{-1}, respectively.
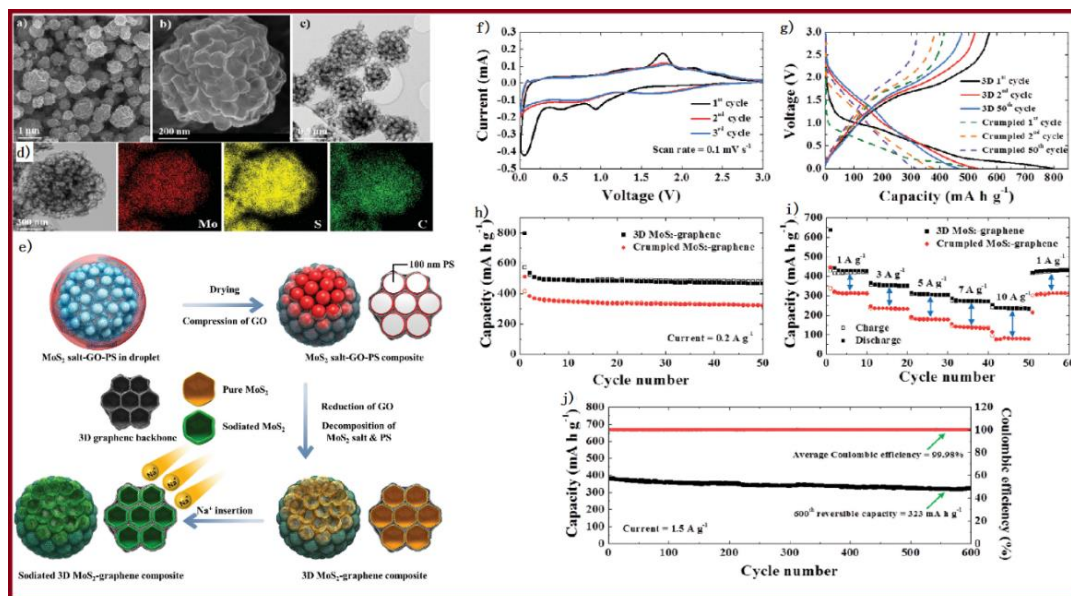
Figure 2-11 Morphologies of the 3D MoS$_2$ –graphene composite microspheres. (a,b) FE-SEM images. (c) TEM image. (d) Elemental mapping images of Mo, S, and C components. (e) Schematic diagram of the formation mechanism of the 3D MoS$_2$ –graphene composite microsphere by the one-pot spray pyrolysis and description of the Na$^+$ insertion process. (f) CV curves of the 3D MoS$_2$ –graphene composite microspheres; (g) charge/discharge curves at a current density of 0.2 A g^{-1}. (h) Cycling performances at a current density of 0.2 A g^{-1}; (i) high rate performances; and (j) long-term cycling properties and Coulombic efficiencies of the 3D MoS$_2$ –graphene composite microspheres at a current density of 1.5 A g^{-1}.

In a brief conclusion, it has been shown that MoS$_2$ is a very promising candidate for anode applications in LIBs and SIBs[136]. There has been a great deal of research has conducted for LIB applications. However, the use of MoS$_2$ in SIBs technology is still in a state of infancy. Historically, two main strategies have been utilized in the development high-performance of MoS$_2$; 1) Controlled fabrication of stable micro/nanostructures with high surface area and porosity, 2) Design of rational MoS$_2$-carbon composites and coatings which are capable of accommodating the volume change and activate the reaction sites, especially with sodium ion insertion.

2.3.4. Tin sulfide SnS$_2$

Tin sulfide has received enormous attention for battery applications due to its layered structure with stacking via van der Waals forces and large interlayer spacing of 0.59 nm [51]. Amongst many phases of tin sulfides, SnS$_2$ and SnS are suggested as the best candidates for batteries implementation due to their high theoretical capacity and structures that facilitate reversible charging/discharging reactions [137-139]. In LIBs and SIBs, SnS$_2$ and SnS experience two stages of reaction: initially, an irreversible conversion reaction occurs in which SnS$_x$ forms Na$_2$S/Li$_2$S and Sn metal; the second stage is the reversible alloying reaction of Sn with lithium or sodium ions yielding high capacities shown in **Table 2.1** [137, 140]. Unfortunately, the capacity fade of SnS$_x$ electrode materials is still a big challenge, due to the large volume expansion, e.g. (over 420% volume expansion upon the formation of Na$_{15}$Sn$_4$), the dissolution of sulfur in the electrolyte and poor electrical conductivity during the electrochemical alloy formation [141, 142]. In order to solve these challenges, one effective strategy is to design various SnS$_x$ nanostructures with different morphologies, such as hierarchitectures [138], nanowalls [143], nanoplates [144], nanobelts [145], nanowires [146], nanoflakes [147], nanospheres [148] and nanoflowers [149]. Other studies focus on the combination of SnS$_x$ with carbonaceous materials such as novel carbon [150] and graphene [137]. Different strategies and approaches will be discussed in details in the following sections.

As mentioned above, SnS$_x$, as important member Sn-based materials, has been widely studied as anode material for LIBs. For example, Wang et al. reported a hydrothermal method to synthesis 2D SnS$_2$ nanoplates as high-performance anode material for LIBs [151]. During the synthesis process, the temperature and pH of the reaction have significant effects on the morphology and performance. It was indicated that the higher crystallinity and thicker structure has the best electrochemical storage. However, it did not excel with regards to rate performance because of the increase in path length for Li-ion diffusion. The results also showed that the pH affects the nucleation rate of SnS$_2$, and the products with the slowest nucleation rate yielded the best electrochemical performance. Hence, SnS$_2$ prepared at 200℃ and 10.5 pH was found to be optimal for high performance in LIBs. In general, it could be observed that thin layered structures and high crystallinity are desired characteristics to obtain good rate capability. The 2D SnS$_2$ is cycled at the potential range of 0.005–1.20 V at a current density of 100 mA g^{-1} and a high capacity of 521 mAh g^{-1} is obtained after 50 cycles, corresponding to a capacity retention of 90% of the initial capacity. Furthermore, 2D SnS$_2$ demonstrates high rate capability exhibiting average discharge capacities of 564, 532, 510, 491, 472, and 397 mAh g^{-1} at current densities of 0.2, 0.4, 0.6, 0.8, 1 and 2 A g^{-1}, respectively. It is believed that the 2D nanostructure of SnS$_x$ has a significant

influence on the electrochemical performances. To compare the effects of nanostructures, SnS_2 nanosheets and nanoflowers are investigated by Bhaskar's group, in which both materials is synthesized through one-pot solvothermal methods [139]. After 100 cycles, it is found that the SnS_2 nanoflower structure exhibits a higher capacity of 542 mAh g^{-1} while SnS_2 nanosheets delivers a capacity of 436.5 mAh g^{-1}. For further evaluation, rate performance was explored for both nanostructured at current densities ranging from 100 to 3000 mA g^{-1}. At current densities of 200, 500, 1000, 2000 and 3000 mA g^{-1}, SnS_2 nanoflowers exhibit high capacities of 733.6, 668.6, 612.1, 525.2 and 466.1 mAh g^{-1}, respectively, whereas SnS_2 nanosheets experience rapid capacity loss from 733.9 to 196 mAh g^{-1} between current densities of 200 to 3000 mA g^{-1}. It is claimed that the better cycling and rate performance of the nanoflowers is a result of higher electrolyte accessibility with less charge transfer resistance. In another solvothermal process, 3D SnS_2 hierarchitectures were synthesised with high specific capacity of 549.5 mAh g^{-1} after 100 cycles at current density of 0.1 mA g^{-1} in the potential range of 0.01–3 V. [138]. This structure also showed high rate capability with capacities of 706.7, 582.4, 432.8, 210.8 mAh g^{-1} at current densities of 100, 200, 500 and 1000 mA g^{-1}, respectively, which returned to 471 mAh g^{-1} when the current density was decreased to 100 mA g^{-1}. Thus, it is believed that such 3D structure with high porosity could be better design than 2D because 3D porous structure provides sufficient inner sites for electrode electrolyte contact that guarantee continuous ions diffusion and help releasing the mechanical stress caused by the severe volume expansion during charging/discharging.

Metal sulfide in composites with high conductive materials has been widely studied for batteries applications to overcome the challenges of capacity fading and volume change[49, 152]. Mei et al. reported the synthesis of ultra-small SnS_2 nanocrystals decorated on flexible reduced graphene oxide (SnS_2 nanocrystals@RGO) via a simple reflux method [141]. The as-prepared composites deliver a high specific capacity of 1034 mAh g^{-1} after 200 cycles at a current density of 0.1 A g^{-1}, and it exhibits superior performance in comparison to other tin sulfides composites have been reported before [153, 154] (see **Figure 2.12 d**). Furthermore, the electrode achieved a reversible capacity of 570 mAh g^{-1} and 415 mAh g^{-1} at current densities of 3A g^{-1} and 5A g^{-1}, respectively, even after 450 cycles (see **Figure 2.12 e**). Additionally, the rate capability of SnS_2 nanocrystals@RGO is tested and shows high capacities as shown in **Figure 2.12 f**. This high electrochemical performance may be attributed to the high surface area of SnS_2 nanocrystals and functional properties of reduced graphene oxide regarding buffering the volume expansion and enhancing the electrochemical conductivity.
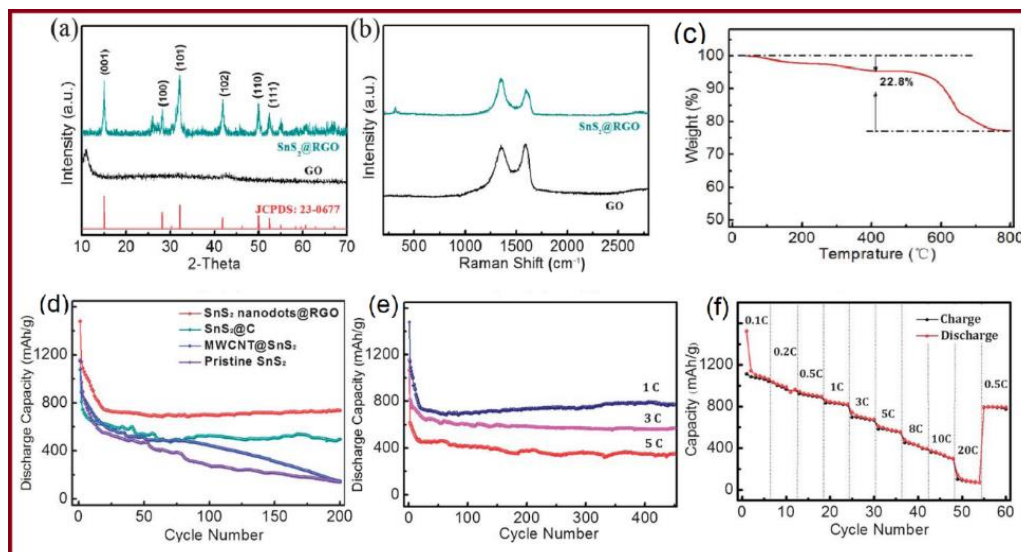
Figure 2-12 (a) XRD patterns of the ultra-small SnS_2 nanocrystals@RGO and GO (the bottom of the image indicates the JCPDS data (JCPDS 23-0677) for SnS_2); (b) the Raman spectra of the SnS_2 nanocrystals@RGO and GO.(c) TGA of the as-prepared SnS_2 nanocrystals@RGO composite from room temperature to 800 C in air; (d) Discharge capacity vs. cycle number of the SnS_2 nanocrystals@RGO, pristine SnS_2, SnS_2@C and MWCNT@SnS_2 electrodes at a rate of 1 C. (e) Cycling behaviours of the SnS_2 nanocrystals@RGO electrode at high rates of 1, 3, and 5C. (f) Cycling performance of the SnS_2 nanocrystals@RGO electrode at various current densities.

Kong and co-workers also study the composite of SnS_2@graphene nanocable structures which could successfully accommodate the volume expansion and enhance Li^+ diffusion through the host material during cycling [155]. This composite exhibits outstanding cycling performance with a capacity retention of 93.5% and capacity as high as 720 mAh g^{-1} at a current density of 200 mA g^{-1} after 350 cycles. Also, rate performance is evaluated with current densities of 1 A g^{-1} and 5 A g^{-1}, showing that the SnS_2@GT electrode can still achieve charge capacities of 580 mAh g^{-1} and 247 mAh g^{-1}, respectively.

Besides the use of carbon matrices, conductive polymers, like PANI, PPY or PEDOT, have also been introduced to improve the conductivities of SnS_x anode materials. A typical two-dimensional nanocomposite, polyaniline-coated SnS_2 (SnS_2@PANI) nanoplates, has been designed via an in situ oxidative polymerization of aniline on the surface of ultrasonic exfoliated SnS_2 nanoplates, which is shown in **Figure 2.13** [156]. The electrochemical results show that the

SnS$_2$@PANI indicates high stable charge capacity of 730.8 mAh g^{-1} after 80 cycles. On the other hand, pristine SnS$_2$ exhibits a capacity retention of 32.8% with a charge capacity of 311.2 mAh g^{-1} at the 80th cycle (see **Figure 2.13 f, g**). **Figure 2.13 i** shows the rate performances of SnS$_2$@PANI and SnS$_2$. It can be observed that SnS$_2$@PANI exhibits better rate performance than pristine SnS$_2$ upon increasing the current density between 200 mA g^{-1} to 5000 mA g^{-1}. It is shown that when current densities are set as at 200, 500, 1000, 2000, and 5000 mA g^{-1}, reversible capacities of 821.8, 726.8, 661.1, 559.2, and 356.1 mAh g^{-1}, respectively, can be obtained by the SnS$_2$@PANI which is apparently better than pristine SnS$_2$.
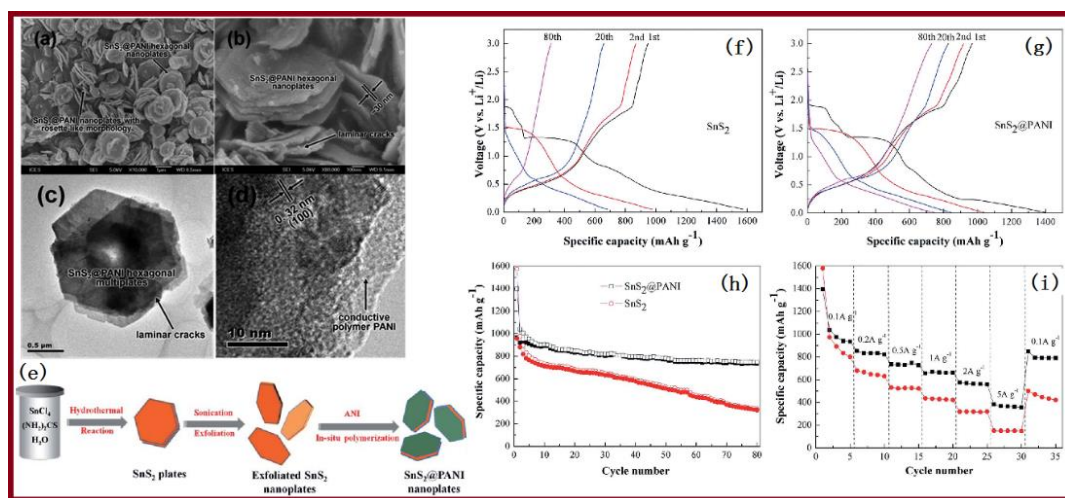
Figure 2-13 (a and b) SEM images of the as-synthesized SnS$_2$@PANI nanoplates at different magnifications. (c) TEM image of the as-synthesized SnS$_2$@PANI nanoplates. (d) HRTEM images of the SnS$_2$@PANI nanoplates. (e) Schematic illustration of the formation of SnS$_2$@PANI nanoplates. Galvanostatic discharge–charge curves of (f) SnS$_2$ and (g) SnS$_2$@PANI cycled at the 1st, 2nd, 20th, and 80th discharge and charge cycles between 0.01 V and 3 V (vs. Li$^+$/Li) at a current density of 100 mA g^{-1}; (h) cycling stability of SnS$_2$ and SnS$_2$@PANI at a current density of 100 mA g^{-1}; (i) rate performance of SnS$_2$ and SnS$_2$@PANI at various current densities between 100 mA g^{-1} and 5000 mA g^{-1}[156].

Similar to MoS$_2$, tin sulfide has been recently reported in sodium ion batteries, but it is still in the early stage. To improve cycling stability and performance, many groups have adopted the approach of designing carbon nanocomposites with tin sulfide due to the enhanced electrochemical and physical properties. For instance, Wu et al. reported a precipitation synthesis of stannous sulfide@reduced graphene oxide (SnS@RGO) composite for SIBs applications [157]. As an anode material, SnS@RGO delivered a high reversible capacity of 386 mAh g^{-1} at 20 mA g^{-1} after 100

cycles in a potential range of 0.01 and 2.0 V. Moreover, when the current density was increased in order to evaluate the rate capability, SnS@RGO still can achieve high capacities of 240 mAh g^{-1} even when cycled at 400 mA g^{-1}. The high performance of SnS_2 composites led to further investigations, such as the development of an ultrathin 2-D film of SnS_2-coated graphene oxide platelets which was synthesized via a decomposition process followed by sulfidization treatment [158]. The GO-SnS_2 delivered a charge capacity of 450 mAh g^{-1} for 100 cycles at a current density of 500 mA g^{-1} and excellent rate capability also was achieved which obtained a high capacity of 340 mAh g^{-1} even at the high rate of 2000 mA g^{-1}. This excellent performance of this material can be attributed to the advantage of the graphene coating of improving the conductivity and offer more flexibility to accommodate the volume change and reduce the consequence strain that occurred as result of the volume expansion. Liu et al. developed the hydrolysis of lithiated SnS_2 followed by a hydrothermal method to obtain SnS_2/graphene nanocomposite [50]. Three samples are prepared with different graphene mass which they were produced and labeled as follow, 10, 20 and 30 mg of graphene corresponding to SnS_2/G-10, SnS_2/G-20, and SnS_2/G-30 (**Figure 2.14 a-d**). Cycling test was done at a current density of 200 mA g^{-1}, and voltage window between 0.01 and 2.5 V. in whichSnS_2/G-20 exhibited the best cycling performance with a capacity of 618.9 mAh g^{-1} after 100 cycles (see **Figure 2.14 f**). In contrast, other samples show inferior performance and lower capacities under the same conditions. Moreover, SnS_2/G-20 achieved excellent rate capability with 99% columbic efficiency and when the current density was increased to 500, 1000, 2000, and 4000 mA g^{-1}, it still can maintain capacities of 532, 461, 381, and 326 mAh g^{-1}, respectively.
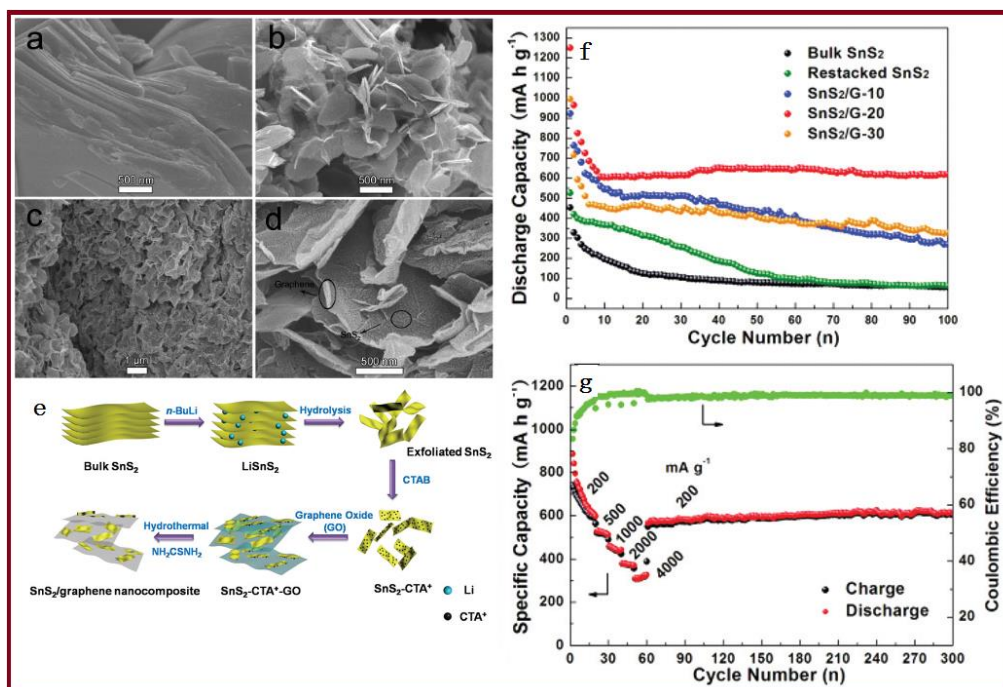
Figure 2-14 SEM images of (a) bulk SnS_2, (b) pure restacked SnS_2, and (c, d) the SnS_2/G-20 nanocomposite. (e) Schematic illustration of the preparation of the SnS_2/graphene nanocomposite. (f) Cycling behavior of the synthesized samples: bulk SnS_2, restacked SnS_2, SnS_2/G-10, SnS_2/G-20, and SnS_2/G-30 at 200 mA g^{-1}. (g) Rate capability and coulombic efficiency of the SnS_2/G-20 electrode.

In conclusion, tin sulfide is a very promising candidate for anode applications in LIBs and SIBs due to their high capacity. However, volume change is a severe problem that eliminates its contribution to storage applications. Therefore, many research groups work on the development of tin sulfides and come up with some solutions such as designing better nanostructures and merge this material with conductive and flexible materials such as carbon to improve the conductivity and reduce the volume expansion.

2.3.5. Tungsten sulfide (WS_2)

Among the TMSs that have been widely reported for energy storage is the 2D-layered WS_2, which has gathered considerable interest owing to the high theoretical capacity and van der Waals forces that facilitate guest ions insertion [159, 160]. However, the small interlayer distance between WS_2 layers and the low electrical conductivity are detrimental to its electrochemical performance.

Therefore, many groups have explored modification of the layered structure and conductivity by designing composites with carbon nanosheets or graphene.

Working on designing unique structures has drawn great attention from different research groups. For example, Feng et al. reported the synthesis of tungsten disulfide (WS_2) nanoflakes via a rheological phase reaction [161]. Regarding the structure effect, it is observed that the nanoflakes exhibited better electrochemical performance than nanotubes and nanoparticles. The high ability of nanoflake structure allows Li^+ intercalate into the structure whether into the nanoflake clusters, defect sites in nanoflakes, or the hollow core which are the possibilities of lithium intercalation is stated by the author. This material delivers a capacity of 680 mAh g^{-1} after 20 cycles at a current density of 47.5 mA g^{-1}. Hard-templating has proven to be another practical approach for the fabrication of high-performance LIB materials, as exemplified by the synthesis of mesoporous WS_2 derived from 2D hexagonal SBA-15 prepared by a vacuum assisted impregnation route [162]. It is indicated that the mesoporous WS_2 exhibited significantly higher performance than bulk WS_2, with a capacity of 805 mAh g^{-1} at a current of 0.1 A g^{-1} after 100 cycles. The mesoporous WS_2 electrode is also able to deliver much higher capacities of 821, 774, 719, 661, 605, 556 and 504 mAh g^{-1} at current densities of 0.1, 0.2, 0.5, 1, 2, 5 and 10 A g^{-1}. It is claimed that WS_2 with a highly-ordered mesoporous network can show good electrochemical performance owing to the high surface area imposed by the hard template and the nanocrystalline structure which shortens the lithium ions diffusion path and improve the rate capability.

Surface coating and additive doping are also very effective strategies to elevate the performance of metal sulfides materials due to the abilities to alleviate volume change and improving the ionic conductivity. For instance, Chen et al. reported a nitrogen-doped graphene and few-layer WS_2 composite (WS_2–NGC) for application in LIBs [54]. They optimized the performance of the material by exploring the effect of different surfactant cetyltrim ethyl ammonium bromide (CTAB)) and precursor (WS_2) concentration ratios in three samples corresponding to 1: 2 for WS_2–NGC1, 2: 2 for WS_2–NGC2 and 5: 2 for WS_2–NGC5. Of the prepared active materials, the WS_2–NGC2 was shown to yield the highest capacity and best rate performance. WS_2–NGC1, WS2–NGC2, WS2–NGC5 and pristine WS_2 was cycled and delivered capacities of 838, 905, 734, 519 mAh g^{-1} respectively. The author claims that the superior performance of WS_2–NGC2 not only corresponds to the concentration ratio of the surfactant and precursor but its physical structure. The close integration of the composite elements facilitates the lithium-ion diffusion and improves the electrolyte accessibility to the inner surfaces of the composite, therefore providing more active sites for reversible reactions. Furthermore, control over

the interactions between WS_2 and graphene layers was investigated when a uniform graphene-like few-layer WS_2 supported on reduced graphene oxide (RGO) was obtained via a hydrothermal method by K. Shiva et al.[163]. In this work, three materials were prepared: bare WS_2, WS_2: RGO=80:20, and WS_2: RGO=70:30 corresponding to the ratio between WS_2 and RGO. The WS_2– RGO composite exhibited a capacity of 450 mAh g^{-1} after 50 cycles at a current density of 100 mA g^{-1}. Rate performance was further investigated with WS_2: RGO=80:20 found to be the better performance in general over WS_2: RGO=70:30 which was ascribed that the RGO over 20% increases the electron movement resistance (see **Figure 2.15**).
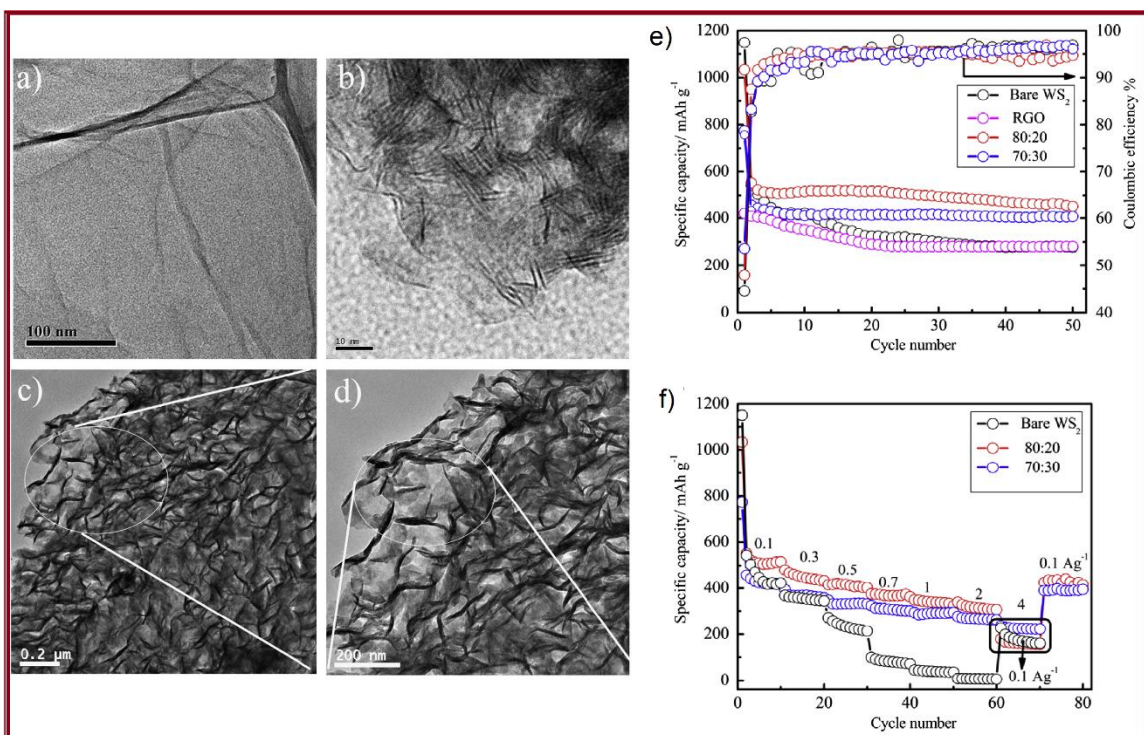
Figure 2-15 Transmission electron micrographs for (a) RGO, (b) bareWS$_2$ and (c–d)WS$_2$– RGO (80:20) composites; (e) The galvanostatic cycling performance of bare WS_2, RGO, 80:20 and 70:30 at a current density of 100mA g^{-1} and Coulombic efficiencies of bare WS_2, 80:20 and 70:30. (f) The specific capacities of bare WS_2, 80:20 and 70:30 at various discharge currents of 0.1,0.3,0.5,0.7,1,2, and 4 A g^{-1} [163].

Carbon coating has also been reported by Du et al. in which they developed a double carbon coating layer on WS_2 through a self-assembly process[164]. The carbon coating that consists of two layers of an oleylamine (OLA)-derived surface carbon layer and an external electronically

conductive and flexible RGO shell that can prevent direct contact between the electrolyte and the active materials. Moreover, as it is a well-known strategy, carbon coating can protect the volume change and structure collapse that is usual of metal-based materials. Upon testing the electrochemical performance of this material, a capacity of 486 mA h g^{-1} was obtained after 200 cycles at a current density of 0.5 A g^{-1}. Even when the current density was increased to 10 A g^{-1}, a capacity of 126 mAh g^{-1} is still delivered successfully.

WS$_2$ has also been utilized as an anode material for sodium-ion batteries. Su et al. reported a hydrothermal synthesis of WS$_2$@graphene nanocomposites[56]. The 3D structure exhibited a high capacity of 329 mAh g^{-1} after 500 cycles which is an order of magnitude better than the 32 mAh g^{-1} delivered by bare WS$_2$. This superior cycling performance could be attributed to the positive effect of the graphene sheets on the conductivity as well as its role in accommodating substantial changes in volume. In another report, Liu et al. studied WS$_2$ Nanowires (NWs) designed for application as an anode material in SIBs [55]. **Figure 2.16** shows that the WS$_2$ NWs exhibit a capacity of 483.2 mAh g^{-1} after 50 cycles at a current rate of 100 mA g^{-1}, and at current rates of 1000, 2000, and 5000 mA g^{-1}, this material could maintain capacities of 430.2, 368.2, and 236.1 mAh g^{-1}, respectively. The authors claim that when cycling in voltage window between 0.01-2.5 V, part of the sodiation reaction is irreversible, leading to the capacity fading and aggregation. Upon changing the cycling range to 0.5-3 V, the reaction mechanism changes from conversion to intercalation, and a definite improvement in the cycling stability is observed which maintains a specific capacity of 415 mAh g^{-1} without fading up to 500 cycles at a current density of 200mA g^{-1}. Furthermore, Zhu et al. reported the use of 3D porous interconnected WS$_2$/C nanocomposites with excellent cycling performance[165]. WS$_2$/C delivered specific capacities are 267 and 219 mAh g^{-1} after 200 cycles and 300 cycles at a current density of 1C, respectively. This high rate capability could be attributed to the interconnection between the 3D porous WS$_2$ nanostructures and the presence of the carbon matrix in the composite which is capable of accommodating the volume change of the active material during cycling.
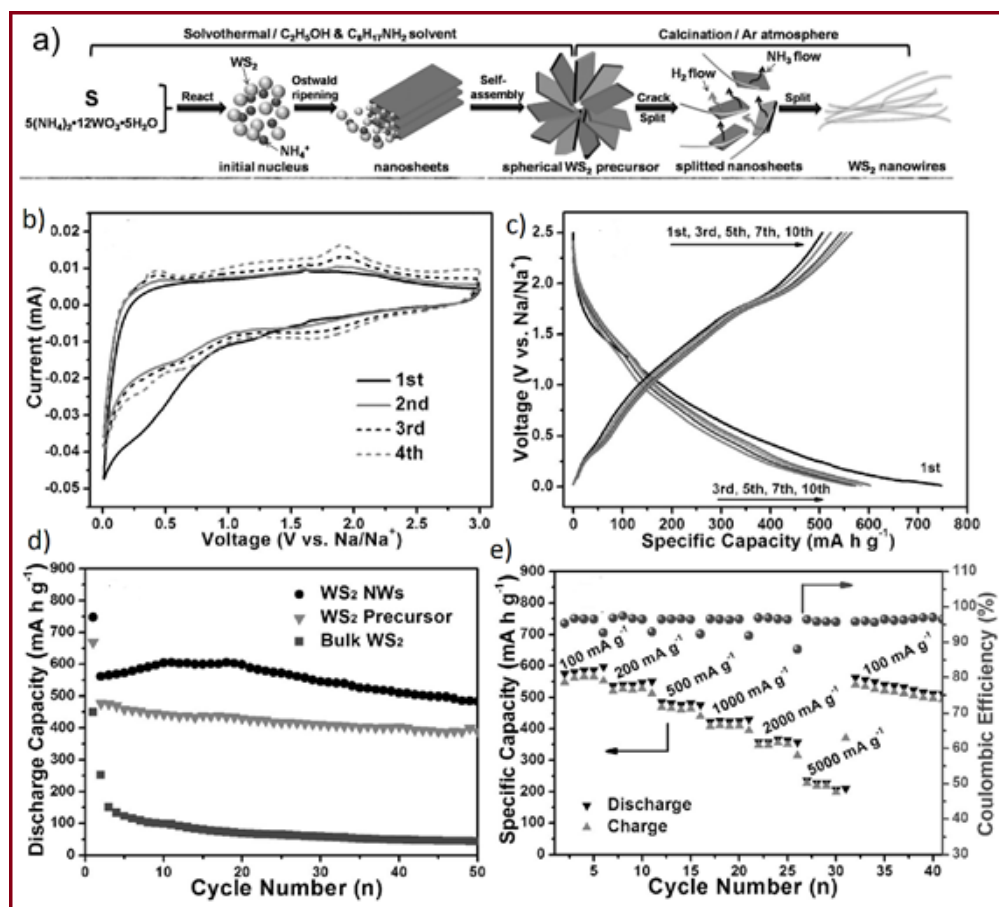
Figure2-16 Synthesis and characterizations of WS$_2$ NWs: a) Schematic formation process of WS$_2$ NWs; b) Cyclic voltammetry curves of the WS$_2$ NWs electrode scanned in the voltage range of 0.01–3.0 V versus Na/Na$^+$ at a rate of 0.1 mV s^{-1}; c) selected galvanostatic discharge/charge profiles of WS$_2$ NWs at a current density of 100 mA g^{-1}; d) cycling performance of the WS$_2$ NWs, WS$_2$ precursor, and bulk WS$_2$ evaluated within a potential window of 0.01 and 2.5 V at 100 mA g^{-1}; e) rate performance and coulombic efficiency of WS$_2$ NWs tested between 0.01 and 2.5 V[55].

2.3.6. Other metal sulfides

Besides the previously mentioned metal sulfides, many other metal sulfides also have been studied for energy storage applications with great promise for increasing the energy density of commercial LIBs. For example, Liu and co-workers reported aa two-step method to synthesis coral-like a-MnS composites with nitrogen-doped carbon (NC)[37]. In this study, the effect of polyvinylpyrrolidone (PVP), as well as annealing temperature in determining the morphology of the final product, was investigated. PVP as an amphiphilic surfactant can assist the distribution of

several nanocrystals in water or organic solvents, and its pyrrolidone groups have high ability to organize with metal ions. It is also essential in the hydrothermal process that metal ions coordinate with the pyrrolidone groups of PVP so that they can distribute homogeneously along the PVP chains and attribute to the uniform structure. It is also approved that PVP plays as a source of carbon and a stabilizing agent. When coral-like a-MnS composite was tested, A capacity of 699 mAh g^{-1} even after 400 cycles was obtained by the optimized (annealed at the best conditions) material at a current density of 0.5A g^{-1}. Another 3-D graphene cross-linked with mesoporous MnS clusters have been synthesized for LIB applications with high specific discharge and charge capacities of 987 and 976 mAh g^{-1} are delivered after 30 cycles, which corresponds to a 97% capacity retention.[166]. The composite exhibited significantly improved performance when compared to pristine MnS that experienced a sharp capacity fading in which delivers low capacity of about ~100mAh g^{-1} at a current density of 50mA g^{-1}. The better performance of the composite is attributed to the addition of graphene which offers high surface area, conductivity, and flexibility. Very recently, atomic layer deposition (ALD) was also applied to synthesis MnS thin films with a highly controlled structure and tested as a LIB anode material[167]. ALD technique is very advanced deposition method for designing thin films, coatings and protection layers that guarantee a uniform deposition thickness and controlled composition ratio. As deposited MnS thin film delivers high discharge and charge capacities of 1205 and 1180 mAh g^{-1}, respectively, achieved after 40 cycles which are apparently superior to the previous reports. The importance of a rationally designed structure was expressed by Xu and co-workers who synthesized MnS hollow microspheres on reduced graphene oxide sheets (MnS/RGO) through a hydrothermal method [36]. MnS/RGO exhibited a capacity of 830 mAh g^{-1} at 0.5 A g^{-1} after 100 cycles when tested for application in LIBs. Furthermore, Xu et al. tested the MnS/RGO material as an anode for SIBs and observed a capacity of 308 mAh g^{-1} at a current density of 0.1 A g^{-1} after 125 cycles.

Nickel sulfide is another interesting material owing to its high theoretical capacity of 870 mAh g^{-1} and has rarely been investigated for battery applications. However, its low conductivity would undesirably affect the cycling performance and still presents the issue of volume change. Mahmood et al. reported the phase-controlled synthesis of nickel sulfide/nitrogen-doped graphene composites for LIB applications[36]. **Figure 2.17 a-c** show the results of the electrochemical performance of this unique material and other optimized materials. Ni_3S_4 /NG-250 °C (250 °C refers to the annealing temperature) exhibited an incredible capacity of 1323.2 mAh g^{-1} after 100 cycles which is the best compared to the other nickel sulfide materials tested. **Figure 2.17d** illustrates the superior rate performance of Ni_3S_4 /NG-250 °C at rates between 0.2C and 4C and exemplifies the cycling stability of the prepared nanocomposite.
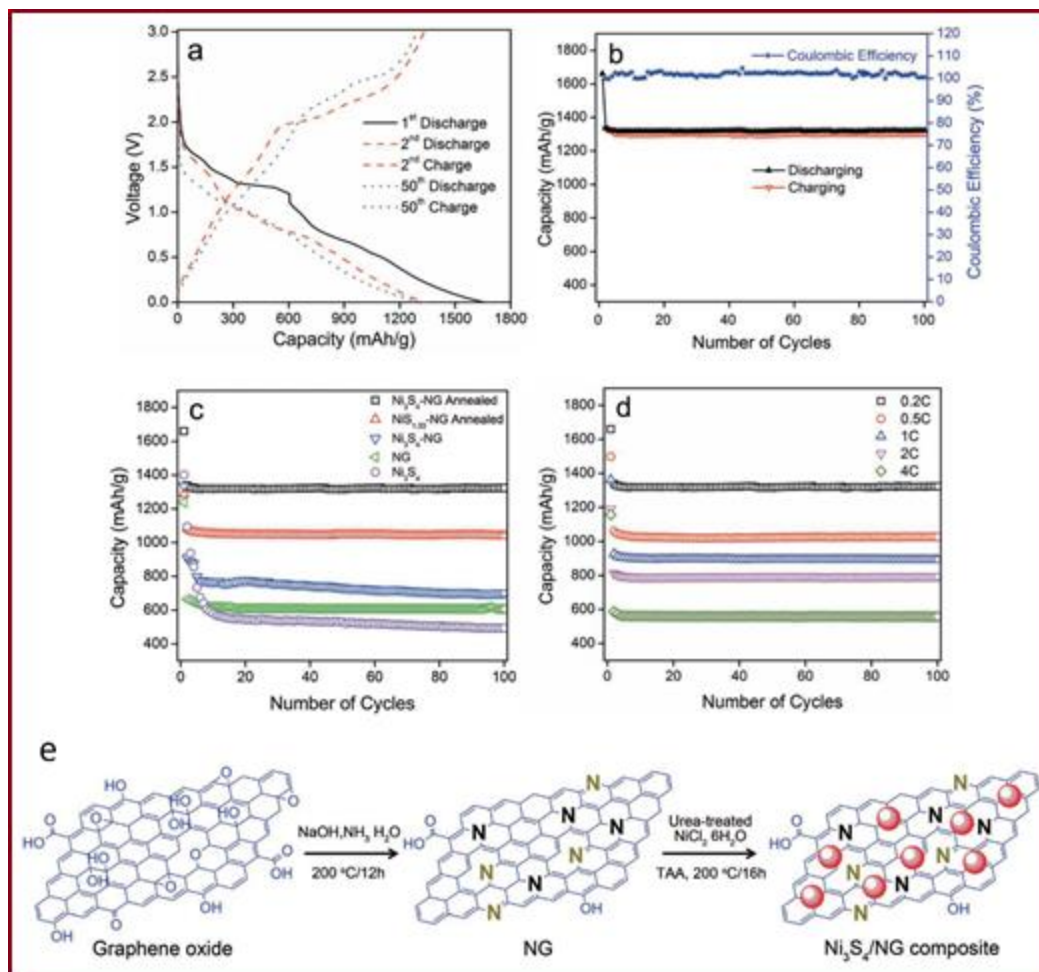
Figure 2-17 (a) Charge-discharge curves of Ni₃S₄ /NG-250 °C composite at 0.2C in the range of 0–3 V. (b) Cyclic behavior and Coulombic efficiency of Ni₃S₄ /NG-250 ° C composite at 0.2C in the range of 0–3 V. (c) Comparison of discharge capacities of Ni₃S₄ , NG, Ni₃S₄ /NG, Ni₃S₄ /NG-250 °C and NiS ₁.₀₃ /NG-350 °C at 0.2C in the range of 0–3 V. (d) Comparison of discharge capacities of Ni₃S₄ /NG-250 °C composite at different C rates in the range of 0–3 V. (e) Schematic illustration of the preparation of the Ni₃S₄ /NG composite[168].

The reason behind the higher performance of Ni₃S₄ /NG-250 in compare to NiS₁.₀₃/NG-350 is that Ni₃S₄ /NG-250 has lower electrolyte resistance that facilitates lithium ions diffusion; also it is claimed based on the chemical reaction equations that Ni₃S₄ /NG-250 inserts more Li+ ions than NiS₁.₀₃/NG-350. The development of a nickel disulfide/graphene composite through hydrothermal reaction was also reported by Chen et al. [41]. This composite demonstrated very

high stability which could be attributed to the flexibility and enhanced conductivity of the graphene matrix. An initial reversible capacity of 720 mAh g^{-1} at 50 mA g^{-1} was recorded for the 1st cycle which subsequently increased to 809 mAh g^{-1} after 150 cycles. As for the rate and performance, Ni$_3$S$_2$/N-doped graphene composite exhibited capacity of 375 mAh g^{-1} at 1000 mA g^{-1}. Park et al. reported a 3D graphene–Vulcan carbon–Bi$_2$S$_3$ nanocomposite was synthesized via an ultrasonic route [20]. The 3D-structured graphene and the attached Vulcan carbon have a direct impact on the cycling performance, leading to a high surface area composite that can provide additional active sites for electrochemical storage. This composite delivered a capacity of 702 mAh g^{-1} at a current density of 100 mA g^{-1} after 100 cycles. Another interesting material is Gallium Sulfide, which is not very well reported. In one case reported by Meng et al., they deposited gallium sulfide (GaS$_x$, x = 1.2) thin films by atomic layer deposition (ALD) onto single-walled carbon nanotube (SWCNT) powders. The ALD GaSx maintained a capacity of 766 mAh g^{-1} at the 100th cycle with the columbic efficiency of 99.8% (see **Figure 2.18**). ALD is a unique technique to deposit thin films and coating with a controllable thickness which it can be used to design different nanostructures for electrode materials and applied in a surface modification to deliver more stable structures.

Xu et al. reported a VS$_4$–graphene nanocomposite anode for LIBs [52]. This composite showed promising performance with delivered capacities of 630 and 314 mAh g^{-1} at high rates of 10 and 20 A g^{-1}, and a reversible capacity of 727 mAh g^{-1} after 50 cycles corresponding to 89% of its first cycle capacity.
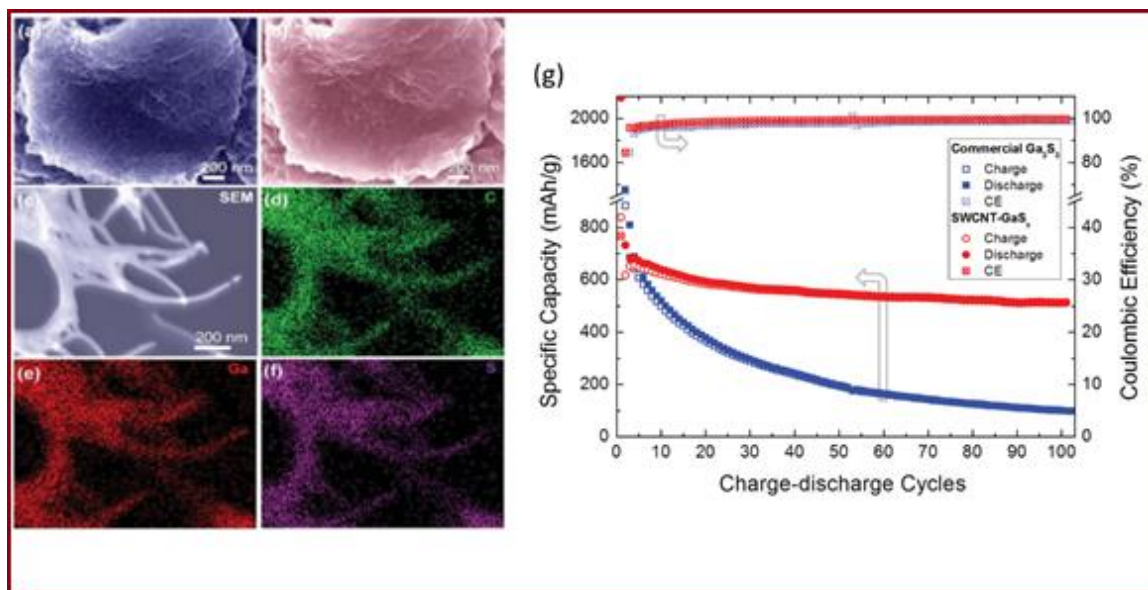
Figure 2-18 a–c) SEM and d–f) EDX mapping images of a) SWCNTs and b,c) 150-cycle ALD GaS$_x$ coated SWCNTs, and EDX mapping of d) carbon, e) gallium, and f) sulfur on 150-cycle ALD GaS$_x$ coated SWCNTs. (g) Cycling performance and columbic efficiency of commercial Ga$_2$S$_3$ and SWCNT-GaS$_x$ composite at 600 mA g^{-1}.

Sb$_2$S$_3$ and Sb$_2$S$_3$@C were developed and electrochemically tested and after 100 cycles[169]. Sb$_2$S$_3$@C still can deliver a reversible capacity of 699.1 mAh g^{-1}, which corresponds to 95.7% of the initial reversible capacity while Sb$_2$S$_3$ maintained only 550.2 mAh g^{-1} after the same cycling period. For the rate, Sb$_2$S$_3$@C exhibited capacities of 724, 695, 680, 642, 578, and 429 mAh g^{-1}, at current densities of 100, 200, 400, 800, 1600, and 3200 mA g^{-1} which was better than the pristine Sb$_2$S$_3$. These results emphasize the function of carbon coating in improving the conductivity and therefore, cycling performance. Vanadium Sulfide growth on reduced graphene oxide (VS$_4$/rGO) was reported for sodium energy storage by Sun and co-workers[53]. VS$_4$/rGO had a reversible capacity of 362 mAh g^{-1} at 100 mA g^{-1} and retained a capacity of 240.8 mAh g^{-1} after 50 cycles. Nickel sulfide hollow nanospheres/reduced graphene oxide composite prepared by a spray drying process was also successfully investigated[43]. The electrochemical performance was carried out and shown in **Figure 2.19**. This kind of structure (hollow amorphous) and composite with carbon matrices is an effective strategy to overcome the problems of volume change and irreversible structural damage.[170]. Moreover, ZnS nanospheres were prepared and tested in a SIB was reported by Su et al. [171]. ZnS nanospheres deliver reversible capacities of 515, 480, 465, and 423

mA h g^{-1} at current densities of 80, 160, 320, and 640 mA g^{-1}, respectively after 100 cycles. An ether-based electrolyte performance was also investigated.

As illustrated by the previously mentioned materials, other metal sulfides such as MnS, Ni$_x$S$_y$, Sb$_x$S$_y$, ZnS…etc; are strong candidates for LIBs and SIBs anode materials due to their high theoretical capacities and diverse structures[172-175]. However, poor cycling is standard issue in metal-based anode materials as observed in these reports. Many techniques were successfully improved electrochemical performance, such as the deposition of metal sulfides on carbon matrices or coating with carbon using techniques including CVD or ALD. Also, emphasizing the functionality of the structural properties such as surface area, orientation, and porosity is very important in determining the materials capability for energy storage applications.
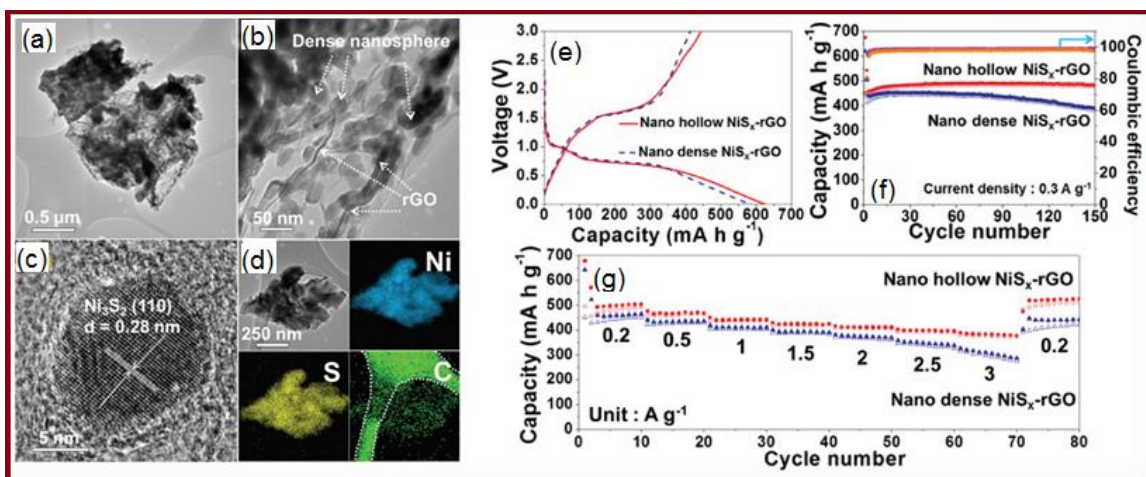
Figure 2-19 (a) and (b) TEM images, (c) HR-TEM image, and (d) elemental mapping images. Electrochemical properties of the nickel sulfide hollow and dense nanospheres/rGO composite powders:(e) initial charge-discharge curves, (f) cycling performances and Coulombic efficiencies, and (g) rate performances[43].

Table 2-2 Summary of nanostructured metal sulfide materials for LIBs

Anode material	Structure	Synthesis method	Capacity (mAh g^{-1}) / cycles	Rate (A g^{-1})	Ref.
CoS$_2$	Nanoparticle	novel strategy	250/20	0.1	[176]
CoS$_2$/RGO	Nanocomposite	novel strategy	640/50	0.1	[176]

Co₃S₄ NTs/G	Nanocomposite	hydrothermal method	720/100	0.2	[26]
Co₃S₄– PNS/GS	Porous nanosheets	freeze-drying and subsequent hydrazine treatment	710 /200	0.5	[64]
Co₉S₈	Hollow nanospheres	solvothermal method	1414/100	0.1	[80]
Co₉S₈@C	Hollow nanospheres	solvothermal method	896/800	2	[80]
CoS@PCP /CNTs	3D hollow cobalt sulfide des@porous carbon polyhedra/ carbon nanotubes hybrids	simultaneous pyrolysis and sulfidation of ZIF-67	1668/100	0.2	[76]
FeS	Microsheet networks	solution-based synthesis	677 /20	0.1	[177]
C@FeS	Nanosheets	surfactant-assisted solution-based synthesis technique	233 /100	10	[178]
pyrite FeS₂	Nanocubes	solvothermal method	540 /150	1	[112]
FeS₂/RGO	Nanocomposite	hydrothermal method	1101 /60	0.1	[109]
FeS₂/rGO	FeS₂ microspheres wrapped with reduced GO sheets	solvothermal method	970 /300	0.89	[110]
Fe₇S₈@C	Nanospheres	simple solid–solid reaction	695 /50 397 /200	0.1	[179]

MoS₂/CNT	3D Interconnected carbon nanotube /layered MoS₂ nanohybrid network	novel strategy	1893 /100	0.1	[130]
MoS₂	Nanoparticles and flakes	an aqueous reduction route	382 /100	0.1	[180]
2D MoS₂/graphene	2D layered/composite	an aqueous reduction route	1063 /100	0.1	[180]
C-MoS₂	Highly uniform nanorods	sulfidation + chemical vapor deposition (CVD)	621 /80	0.2	[181]
MoS₂	Hierarchical MoS₂ microboxes	template-assisted strategy	900/50	0.1	[128]
Ag/Fe₃O₄– MoS₂	Ag and Fe₃O₄ nanoparticles on MoS₂ nanosheets	liquid-phase exfoliation+ further coating process	1026 /100	1	[182]
SnS₂	2D SnS₂ nanoplates	hydrothermal method	521 /50 340 /30	1 3	[151]
SnS₂/ RGO	SnS₂ nanocrystals on RGO nanosheets	refluxing method	1034 /200	0.1	[141]
SnS₂@graphene	Nanocable network	novel strategy	720 /350	0.2	[155]
SnS₂@PANI	Nanoplates	ultrasonic exfoliation method	730.8/80 356.1 /80	0.1 5	[156]
C@SnS	Carbon-Coated 3D Porous Interconnected SnS	electrostatic spray deposition technique	607 /200 535 /300	1	[140]

WS$_2$@C/RGO	composite	self-assembly process	486 /200	0.5	[164]
ZnS/ porous carbon (PC)	ZnS nanoparticles embedded in PC matrices	metal–organic frameworks (MOFs) strategy	438 /300	0.1	[57]
MnS/graphene	3-D graphene cross-linked with mesoporous MnS	solvothermal approach	980 /30	0.05	[166]
α-MnS–NC	Coral composite + nitrogen-doped carbon	In situ two-step method	699 /400	0.5	[37]
MnS/RGO	MnS hollow microspheres/RGO composites	Ostwald ripening process	640 /400	1.0	[36]
VS$_4$–graphene	Nanocomposite	hydrothermal method	727 /50	4	[52]
Bi$_2$S$_3$+ graphene+ C	(3D) graphene–Vulcan carbon–Bi$_2$S$_3$ nanocomposite	sonochemical method	702 /100	0.1	[20]
Bi$_2$S$_3$/GO/ PEDOT	Bi$_2$S$_3$/graphene oxide (GO) composite enwrapped by a poly(3,4-ethylenedioxythiophene) (PEDOT) coating	hydrothermal method	220 /50	0.1	[21]

Ni₃S₄ NPs/ NG	Composite of nickel sulfides, grown on nitrogen-doped graphene (NG) sheets	hydrothermal	558.2 /100	4	[40]
NiS₂/graphene	Composite	hydrothermal reaction	810 /1000	0.5	[41]
SWCNT-GaS$_X$ x = 1.2	core-shell, nanostructured SWCNT-GaSx composite	atomic layer deposition (ALD)	766 /100	0.12	[35]
Sb₂S₃	Bulk crystalline	Sigma Aldrich	~800 /50	0.25	[44]
MgS/AB Acetylene black	Nanocrystalline	solid state reaction of MgH₂ of S via ball milling	629 /80	0.05	[114]

Table 2-3 Summary of nanostructured metal sulfide materials for SIBs

Anode material	Structure	Synthesis method	Capacity (mAh g⁻¹) /cycles	Rate (A g⁻¹)	Ref.
CoS/rGO	Sandwich-like composite	hydrothermal method	230 /100	0.1	[98]
cobalt sulfides/dodecahedral porous carbon	3-dimensional core-shell	facile synthetic route in situ derived from ZIF-67	300 /50	0.5	[183]

CoS$_2$/ multi-walled carbon nanotube (MWCNT)	Nanocomposite	hydrothermal method	568 /100	0.1	[69]
Co$_9$S$_8$-C	Co$_9$S$_8$ nanoparticles + amorphous Carbon composite	one-pot spray pyrolysis process	404 /50	0.5	[99]
FeS$_2$	Microspheres	solvothermal route	170 /12000	20	[116]
FeS$_2$	Nanocrystals	thermal reaction	500 /400	1	[33, 115]
MoS$_2$	Nanosheets	exfoliation technique	161 /100	0.1	[132]
MoS$_2$/RGO	Composites	microwave assisted reduction	305/50	0.1	[184]
3D MoS$_2$-graphene	Microspheres composite	one-pot spray pyrolysis process	322 /600	1.5	[134]
Graphene-like MoS$_2$	Nanoflowers	hydrothermal method and treated by freeze drying	300 /1500	1	[133]
SnS$_2$@Graphene	Nanosheet arrays	solvothermal route	378 /200	1.2	[185]
SnS$_2$/C	Nanospheres	solid-state reaction	570 /100	0.05	[51]
GO-SnS$_2$	Nanocrystals	set of sequential wet-chemistry steps	320 /150	2	[158]
WS$_2$@graphene	Nanocomposite	hydrothermal	148 /500	0.32	[56]
WS$_2$ NWs	Nanowires	solvothermal method	483.2/50	0.1	[55]

WS$_2$/C	3D porous interconnected WS$_2$/C nanocomposite	electrostatic spray deposition (ESD)	219 /300	1	[165]
Ni/rGO	Hollow nanospheres	Spray-drying+nanoscale Kirkendall diffusion process	449 /150	0.3	[43]
MnS/RGO	Hollow microspheres	hydrothermal method	308 /125	0.1	[36]
rGO/Sb$_2$S$_3$	Composite	solution-based synthesis technique	670 /50	0.05	[186]
Sb$_2$S$_3$@C	One-Dimensional Rod	solvothermal method	699.1/100	0.1	[169]
ZnS	Nanospheres	thermal decomposition	423 /100	0.64	[58]
VS$_4$/rGO	Composite	hydrothermal synthesis	240.8 /50	0.1	[53, 187]
Ni$_3$Co$_6$S$_8$–RGO	Composite	spray pyrolysis + sulfidation process	498/100	0.5	[188]

2.4. Conclusion and outlook

Metal sulfides are considered as a unique class of materials in many aspects. Owing to their high theoretical capacity, unique structural properties, and practical synthesis, TMSs hold great potential for applications in energy storage and conversion. However, TMSs for batteries face some problems that need to be solved. For instance, capacity fading associated with the volume change and low conductivity is still a big challenge to overcome. In this case, we have reviewed the properties and applications of TMS for batteries (LIBs & SIBs), in which the detailed discussion was carried on through demonstrating different approaches and strategies. Firstly, one primary strategy has been applied for TMSs is the exploration of new rational structure designs. Different morphologies of TMSs have been successfully investigated to improve the performances and lifetime regarding relieving the volume expansion during electrochemical cycling. Secondly, due

to the low conductivity of TMSs, highly conductive materials including nanocarbon (graphene and carbon nanotubes) and conductive polymers have been introduced to form conductive composites. These functional additives can significantly enhance the conductivity of the composites, which further play an essential role in the electrochemical performances. Thirdly, surface modification is another useful approach to solve many of the problems. One of the most popular coatings in this area is carbon coated on the surface of TMSs, which has proven to be very cheap and successful approach to improving the electrochemical performance by increasing the conductivity, enhancing the surface chemistry of the active materials and accommodate the volume expansion effect. Interestingly, some studies emphasize the role of the electrolyte, including carbonate-based and ether-based, which also significantly affects the performances, particularly for SIBs.

Although many outstanding results have been achieved using TMS as anode materials for both LIBs and SIBs, there are still challenges to be overcome in the future. Further improvements are required to achieve higher specific capacities and longer lifetimes for TMSs. First, the active design and controllable fabrication of TMSs with unique structure and morphology are still undergoing, in which the relationship between structure and performances need to be further studied and emphasized. Meanwhile, the mass production of TMSs is still one of the challenges for making it into the practical application of batteries. Secondly, one of the most severe issues between the electrode and liquid electrolyte in LIBs and SIBs is the interfacial reactions, in which the SEI formation on anode materials will irreversibly consume electrolyte, leading to the fading of battery performances. In this case, surface modification and coating on TMSs is another approach to reduce the side reactions and enhance the performance of the materials. Besides usual carbon coating, surface coating by atomic layer deposition/molecular layer deposition (ALD/MLD) with tuned thickness and uniform coating layers is considered an ideal coating technique to ameliorate the surface, which is expected to improve the electrochemical performances significantly. Lastly, new approaches to synthesize TMSs need to be further explored. Recently, one of the novel approaches that has received increasing attention in this field is the use of MOFs as a template for TMSs with high surface area and porosity, even hierarchical nanostructure with the formation of carbon matrix. On the other hand, ALD can not only be used for surface modification, but also for the synthesis of thin film TMSs with controllable thickness and uniform distribution [35, 167, 189-191]. Almost any type of TMSs can be deposited on any substrate which open doors for different materials to be used in energy storage applications. Also, it is well-known that the mixed transition metal oxides (MTMOs) are the derivative of a metal oxide for batteries application, which shows significant enhancement and has attracted increasing attention in the past years. Our previous review paper has summarised the detailed development and understanding of MTMOs as anode materials for

LIBs. Following a similar idea, a combination of two or more different metals with metal sulfides is going to resolve some electrochemical imperfections in these materials such as low conductivity, low capacity, and slow ion kinetics. The final product will collect the characteristics of every single metal and deliver it in one composite [20, 45, 192]. In this case, analogical methods to optimize the synthesis parameters, material properties and electrochemical mechanism of MTMSs can be switched over to mixed transition metal sulfides to gain a fundamental understanding, which will be another interesting topic and further expand the potential materials for high performances LIBs and SIBs.

It is believed that TMSs are promising candidates for both LIBs and SIBs and further research is required to improve the battery performances. With rational and careful design, it is expected that TMSs can be more practical as anode materials for both LIBs and SIBs in the future.

Acknowledgments

References

1. Zhao, Y., et al., *Recent Developments and Understanding of Novel Mixed Transition-Metal Oxides as Anodes in Lithium-Ion Batteries.* Advanced Energy Materials, 2016. **6**(8).

2. Wang, J., Y. Li, and X. Sun, *Challenges and opportunities of nanostructured materials for aprotic rechargeable lithium-air batteries.* Nano Energy, 2013. **2**(4): p. 443-467.

3. Armand, M. and J.M. Tarascon, *Building better batteries.* Nature, 2008. **451**(7179): p. 652-657.

4. Wu, H.B., et al., *Nanostructured metal oxide-based materials as advanced anodes for lithium-ion batteries.* Nanoscale, 2012. **4**(8): p. 2526-42.

5. Chan, C.K., et al., *High-performance lithium battery anodes using silicon nanowires.* Nat Nanotechnol, 2008. **3**(1): p. 31-5.

6. Wen, Y., et al., *Expanded graphite as a superior anode for sodium-ion batteries.* Nat Commun, 2014. **5**: p. 4033.

7.   Yan, Y., et al., *A Sandwich-Like Hierarchically Porous Carbon/Graphene Composite as a High-Performance Anode Material for Sodium-Ion Batteries.* Advanced Energy Materials, 2014. **4**(8): p. n/a/a.

8.   Zhao, Y., et al., *Metal organic frameworks for energy storage and conversion.* Energy Storage Materials, 2016. **2**: p. 35-62.

9.   Arico, A.S., et al., *Nanostructured materials for advanced energy conversion and storage devices.* Nature Materials, 2005. **4**(5): p. 366-377.

10.   Tarascon, J.M. and M. Armand, *Issues and challenges facing rechargeable lithium batteries.* Nature, 2001. **414**(6861): p. 359-367.

11.   Roy, P. and S.K. Srivastava, *Nanostructured anode materials for lithium-ion batteries.* J. Mater. Chem. A, 2015. **3**(6): p. 2454-2484.

12.   Jiang, J., et al., *Recent advances in metal oxide-based electrode architecture design for electrochemical energy storage.* Adv Mater, 2012. **24**(38): p. 5166-80.

13.   Rui, X., H. Tan, and Q. Yan, *Nanostructured metal sulfides for energy storage.* Nanoscale, 2014. **6**(17): p. 9889-924.

14.   Zu, C.-X. and H. Li, *Thermodynamic analysis of energy densities of batteries.* Energy & Environmental Science, 2011. **4**(8): p. 2614.

15.   Hu, Z., et al., *Advances and Challenges in Metal Sulfides/Selenides for Next-Generation Rechargeable Sodium-Ion Batteries.* Adv Mater, 2017.

16.   Shi, J., et al., *Recent Advances in Controlling Syntheses and Energy-Related Applications of MX2 and MX2/Graphene Heterostructures.* Advanced Energy Materials, 2016. **6**(17): p. 1600459.

17.   Xu, X., et al., *Nanostructured transition metal sulfides for lithium-ion batteries: Progress and challenges.* Nano Today, 2014. **9**(5): p. 604-630.

18.   Yu, X.-Y., L. Yu, and X.W.D. Lou, *Metal Sulfide Hollow Nanostructures for Electrochemical Energy Storage.* Advanced Energy Materials, 2016. **6**(3): p. 1501333.

19.   Ramakrishna Matte, H.S.S., et al., *MoS2 and WS2 Analogues of Graphene.* Angewandte Chemie, 2010. **122**(24): p. 4153-4156.

20.   Park, S.-K., et al., *Design and tailoring of three-dimensional graphene–Vulcan carbon–Bi2S3 ternary nanostructures for high-performance lithium-ion-battery anodes.* RSC Adv., 2015. **5**(65): p. 52687-52694.

21.   Mukkabla, R., M. Deepa, and A.K. Srivastava, *Enhanced Lithium-Ion Storage Capability of a Bismuth Sulfide/Graphene Oxide/Poly(3,4-ethylene dioxythiophene) Composite.* Chemphyschem, 2015. **16**(15): p. 3242-53.

22. He, J., et al., *Self-assembled CoS2 nanoparticles wrapped by CoS2-quantum-dots-anchored graphene nanosheets as a superior-capability anode for lithium-ion batteries.* Electrochimica Acta, 2015. **182**: p. 424-429.

23. Zhian Zhang, Y.G., Yanqing Laia,*, Xiaodong Shia, Wei Chena, Jie Lia, *Cobalt sulfides/dodecahedral porous carbon as anode materials for Na-ion batteries.pdf.* RSC. Advances, 2015. **5**(125): p. 103410-103413

24. Su, Q.M., et al., *In Situ Transmission Electron Microscopy Observation of Electrochemical Behavior of CoS2 in Lithium-Ion Battery.* ACS Applied Materials & Interfaces, 2014. **6**(4): p. 3016-3022.

25. Qian Zhou, L.L.,* Guoxiong Guo, Zichao Yan, Jinli Tan, Zhifeng Huang, Xiaoying Chen and Xianyou Wang*, *Sandwich-like cobalt sulfide–graphene composite-an anode material with an excellent electrochemical performance for sodium ion batteries.* RSC Advances, 2015. **5**: p. 71644–71651.

26. Mahmood, N., et al., *Multifunctional Co3S4/graphene composites for lithium-ion batteries and oxygen reduction reaction.* Chemistry, 2013. **19**(16): p. 5183-90.

27. Shi, W., et al., *Controlled synthesis of carbon-coated cobalt sulfide nanostructures in oil phase with enhanced li storage performances.* ACS Appl Mater Interfaces, 2012. **4**(6): p. 2999-3006.

28. Feng, C., et al., *One-Pot Synthesis of Copper Sulfide Nanowires/Reduced Graphene Oxide Nanocomposites with Excellent Lithium-Storage Properties as Anode Materials for Lithium-Ion Batteries.* ACS Appl Mater Interfaces, 2015. **7**(29): p. 15726-34.

29. Dong, C.C., et al., *Enhanced the electrochemical performance of FeS coated by Ag as an anode for lithium-ion batteries.* Applied Surface Science, 2013. **265**: p. 114-119.

30. Xia, J., et al., *Facile synthesis of FeS2 nanocrystals and their magnetic and electrochemical properties.* RSC Advances, 2013. **3**(17): p. 6132-6140.

31. Qiu, W.D., et al., *L-Cysteine-Assisted Synthesis of Cubic Pyrite/Nitrogen-Doped Graphene Composite as Anode Material for Lithium-ion Batteries.* Electrochimica Acta, 2014. **137**: p. 197-205.

32. Hu, Z., et al., *Pyrite FeS2 for high-rate and long-life rechargeable sodium batteries.* Energy & Environmental Science, 2015. **8**(4): p. 1309-1316.

33. Walter, M., T. Zund, and M.V. Kovalenko, *Pyrite (FeS2) nanocrystals as inexpensive high-performance lithium-ion cathode and sodium-ion anode materials.* Nanoscale, 2015. **7**(20): p. 9158-63.

34. Zhang, K.L., et al., *A potential pyrrhotite (Fe7S8) anode material for lithium storage.* RSC Advances, 2015. **5**(19): p. 14828-14831.

35.   Meng, X., et al., *Gallium Sulfide-Single-Walled Carbon Nanotube Composites: High-Performance Anodes for Lithium-Ion Batteries*. Advanced Functional Materials, 2014. **24**(34): p. 5435-5442.

36.   Xu, X., et al., *In Situ Synthesis of MnS Hollow Microspheres on Reduced Graphene Oxide Sheets as High-Capacity and Long-Life Anodes for Li- and Na-Ion Batteries*. ACS Appl Mater Interfaces, 2015. **7**(37): p. 20957-64.

37.   Liu, Y., et al., *Coral-like α-MnS composites with N-doped carbon as anode materials for high-performance lithium-ion batteries*. Journal of Materials Chemistry, 2012. **22**(45): p. 24026.

38.   Lingappan, N., et al., *Growth of three dimensional flower-like molybdenum disulfide hierarchical structures on graphene/carbon nanotube network: An advanced heterostructure for energy storage devices*. Journal of Power Sources, 2015. **280**: p. 39-46.

39.   Xie, X., et al., *MoS2/Graphene Composite Anodes with Enhanced Performance for Sodium-Ion Batteries: The Role of the Two-Dimensional Heterointerface*. Advanced Functional Materials, 2015. **25**(9): p. 1393-1403.

40.   Mahmood, N., C. Zhang, and Y. Hou, *Nickel sulfide/nitrogen-doped graphene composites: phase-controlled synthesis and high performance anode materials for lithium-ion batteries*. Small, 2013. **9**(8): p. 1321-8.

41.   Chen, Q., et al., *l-Cysteine-assisted hydrothermal synthesis of nickel disulfide/graphene composite with enhanced electrochemical performance for reversible lithium storage*. Journal of Power Sources, 2015. **294**: p. 51-58.

42.   Qin, W., et al., *Layered nickel sulfide-reduced graphene oxide composites synthesized via microwave-assisted method as high performance anode materials for sodium-ion batteries*. Journal of Power Sources, 2016. **302**: p. 202-209.

43.   Park, G.D., J.S. Cho, and Y.C. Kang, *Sodium-ion storage properties of nickel sulfide hollow nanospheres/reduced graphene oxide composite powders prepared by a spray drying process and the nanoscale Kirkendall effect*. Nanoscale, 2015. **7**(40): p. 16781-8.

44.   Yu, D.Y., H.E. Hoster, and S.K. Batabyal, *Bulk antimony sulfide with excellent cycle stability as next-generation anode for lithium-ion batteries*. Sci Rep, 2014. **4**: p. 4562.

45.   Zhao, Y. and A. Manthiram, *Bi0.94Sb1.06S3 Nanorod Cluster Anodes for Sodium-Ion Batteries: Enhanced Reversibility by the Synergistic Effect of the Bi2S3–Sb2S3 Solid Solution*. Chemistry of Materials, 2015. **27**(17): p. 6139-6145.

46.   Cai, J., Z. Li, and P.K. Shen, *Porous SnS nanorods/carbon hybrid materials as highly stable and high capacity anode for Li-ion batteries*. ACS Appl Mater Interfaces, 2012. **4**(8): p. 4093-8.

47.   Zhou, T.F., et al., *Enhanced Sodium-Ion Battery Performance by Structural Phase Transition from Two-Dimensional Hexagonal-SnS2 to Orthorhombic-SnS.* ACS Nano, 2014. **8**(8): p. 8323-8333.

48.   Chen, C.-Y., et al., *One-Step Hydrothermal Synthesis of SnS2/SnO2/C Hierarchical Heterostructures for Li-ion Batteries Anode with Superior Rate Capabilities.* Electrochimica Acta, 2015. **183**: p. 78-84.

49.   Zhang, Q., et al., *SnS2/reduced graphene oxide nanocomposites with superior lithium storage performance.* Electrochimica Acta, 2014. **115**: p. 425-433.

50.   Liu, Y.C., et al., *Exfoliated-SnS2 restacked on graphene as a high-capacity, high-rate, and long-cycle life anode for sodium ion batteries.* Nanoscale, 2015. **7**(4): p. 1325-1332.

51.   Wang, J., et al., *Solid-State Fabrication of SnS2/C Nanospheres for High-Performance Sodium Ion Battery Anode.* ACS Appl Mater Interfaces, 2015. **7**(21): p. 11476-81.

52.   Xu, X., et al., *Lithium reaction mechanism and high rate capability of VS4–graphene nanocomposite as an anode material for lithium batteries.* Journal of Materials Chemistry A, 2014. **2**(28): p. 10847.

53.   Sun, R., et al., *Vanadium Sulfide on Reduced Graphene Oxide Layer as a Promising Anode for Sodium-Ion Batteries.* ACS Appl Mater Interfaces, 2015. **7**(37): p. 20902-8.

54.   Chen, D., et al., *In situ nitrogenated graphene-few-layer WS2 composites for fast and reversible Li+ storage.* Nanoscale, 2013. **5**(17): p. 7890-6.

55.   Liu, Y., et al., *WS2 Nanowires as a High-Performance Anode for Sodium-Ion Batteries.* Chemistry, 2015. **21**(33): p. 11878-84.

56.   Su, D., S. Dou, and G. Wang, *WS(2)@graphene nanocomposites as anode materials for Na-ion batteries with enhanced electrochemical performances.* Chem Commun (Camb), 2014. **50**(32): p. 4192-5.

57.   Fu, Y., et al., *ZnS nanoparticles embedded in porous carbon matrices as anode materials for lithium-ion batteries.* RSC Adv., 2015. **5**(106): p. 86941-86944.

58.   Su, D., K. Kretschmer, and G. Wang, *Improved Electrochemical Performance of Na-Ion Batteries in Ether-Based Electrolytes: A Case Study of ZnS Nanospheres.* Advanced Energy Materials, 2015: p. 1-13.

59.   Peng, S., et al., *Cobalt sulfide nanosheet/graphene/carbon nanotube nanocomposites as flexible electrodes for hydrogen evolution.* Angew Chem Int Ed Engl, 2014. **53**(46): p. 12594-9.

60.   Wang, H., et al., *Co(1-x)S-graphene hybrid: a high-performance metal chalcogenide electrocatalyst for oxygen reduction.* Angew Chem Int Ed Engl, 2011. **50**(46): p. 10969-72.

61.   Yang, J., et al., *High catalytic activity and stability of nickel sulfide and cobalt sulfide hierarchical nanospheres on the counter electrodes for dye-sensitized solar cells.* Chem Commun (Camb), 2014. **50**(37): p. 4824-6.

62.   Huo, J., et al., *A high performance cobalt sulfide counter electrode for dye-sensitized solar cells.* Electrochimica Acta, 2015. **159**: p. 166-173.

63.   Liu, J., et al., *MOF-Derived Hollow Co9S8 Nanoparticles Embedded in Graphitic Carbon Nanocages with Superior Li-Ion Storage.* Small, 2016. **12**(17): p. 2354-64.

64.   Du, Y., et al., *Co3S4 porous nanosheets embedded in graphene sheets as high-performance anode materials for lithium and sodium storage.* J. Mater. Chem. A, 2015. **3**(13): p. 6787-6791.

65.   Zhou, Y., et al., *Multiwalled carbon nanotube@a-C@Co9S8 nanocomposites: a high-capacity and long-life anode material for advanced lithium-ion batteries.* Nanoscale, 2015. **7**(8): p. 3520-5.

66.   Zhang, J., L. Yu, and X.W.D. Lou, *Embedding CoS2 nanoparticles in N-doped carbon nanotube hollow frameworks for enhanced lithium storage properties.* Nano Research, 2017.

67.   Zeng, P., et al., *In Situ Formation of Co9S8/N-C Hollow Nanospheres by Pyrolysis and Sulfurization of ZIF-67 for High-Performance Lithium-Ion Batteries.* Chemistry, 2017.

68.   Wang, Y.H., et al., *Synthesis of Micro/nanostructured Co9S8 Cubes and Spheres as High-Performance Anodes for Lithium-Ion Batteries.* Electrochimica Acta, 2017. **230**: p. 299-307.

69.   Shadike, Z., et al., *Improved electrochemical performance of CoS2-MWCNT nanocomposites for sodium-ion batteries.* Chem Commun (Camb), 2015. **51**(52): p. 10486-9.

70.   Zhang, Z., et al., *Cobalt sulfides/dodecahedral porous carbon as anode materials for Na-ion batteries.* RSC Adv., 2015. **5**(125): p. 103410-103413.

71.   Bao, S.-J., et al., *Biomolecule-assisted synthesis of cobalt sulfide nanowires for application in supercapacitors.* Journal of Power Sources, 2008. **180**(1): p. 676-681.

72.   Yang, Z., C.-Y. Chen, and H.-T. Chang, *Supercapacitors incorporating hollow cobalt sulfide hexagonal nanosheets.* Journal of Power Sources, 2011. **196**(18): p. 7874-7877.

73.   You, B., et al., *Microwave vs. solvothermal synthesis of hollow cobalt sulfide nanoprisms for electrocatalytic hydrogen evolution and supercapacitors.* Chem Commun (Camb), 2015. **51**(20): p. 4252-5.

74.   Apostolova, R.D., et al., *Study of electrolytic cobalt sulfide Co9S8 as an electrode material in lithium accumulator prototypes.* Russian Journal of Electrochemistry, 2009. **45**(3): p. 311-319.

75.   Wang, J., et al., *Synthesis and characterization of nanosize cobalt sulfide for rechargeable lithium batteries.* Journal of Power Sources, 2006. **159**(1): p. 287-290.

76.   Wu, R., et al., *In-situ formation of hollow hybrids composed of cobalt sulfides embedded within porous carbon polyhedra/carbon nanotubes for high-performance lithium-ion batteries.* Adv Mater, 2015. **27**(19): p. 3038-44.

77.   Wang, Z., L. Zhou, and X.W. David Lou, *Metal Oxide Hollow Nanostructures for Lithium-ion Batteries.* Advanced Materials, 2012. **24**(14): p. 1903-1911.

78.   Jeong, J.M., et al., *Hierarchical hollow spheres of Fe2O3 @polyaniline for lithium-ion battery anodes.* Adv Mater, 2013. **25**(43): p. 6250-5.

79.   Jin, R., et al., *Hierarchical worm-like CoS2 composed of ultrathin nanosheets as an anode material for lithium-ion batteries.* J. Mater. Chem. A, 2015. **3**(20): p. 10677-10680.

80.   Zhou, Y., et al., *Hollow nanospheres of mesoporous Co9S8 as a high-capacity and long-life anode for advanced lithium-ion batteries.* Nano Energy, 2015. **12**: p. 528-537.

81.   Peng, S., et al., *Hollow nanospheres constructed by CoS2 nanosheets with a nitrogen-doped-carbon coating for energy-storage and photocatalysis.* ChemSusChem, 2014. **7**(8): p. 2212-20.

82.   Geim, A.K. and K.S. Novoselov, *The rise of graphene.* Nature Materials, 2007. **6**(3): p. 183-191.

83.   Zhao, Y., et al., *Significant impact of 2D graphene nanosheets on large volume change tin-based anodes in lithium-ion batteries: A review.* Journal of Power Sources, 2015. **274**: p. 869-884.

84.   Han, Y., Z. Xu, and C. Gao, *Ultrathin Graphene Nanofiltration Membrane for Water Purification.* Advanced Functional Materials, 2013. **23**(29): p. 3693-3700.

85.   Biju, V., *Chemical modifications and bioconjugate reactions of nanomaterials for sensing, imaging, drug delivery and therapy.* Chem Soc Rev, 2014. **43**(3): p. 744-64.

86.   Chen, Y., et al., *Two-dimensional graphene analogs for biomedical applications.* Chem Soc Rev, 2015. **44**(9): p. 2681-701.

87.   Chen, D., et al., *Graphene and its derivatives for the development of solar cells, photoelectrochemical, and photocatalytic applications.* Energy & Environmental Science, 2013. **6**(5): p. 1362.

88.   Zheng, Y., et al., *Graphitic carbon nitride materials: controllable synthesis and applications in fuel cells and photocatalysis.* Energy & Environmental Science, 2012. **5**(5): p. 6717.

89.   Bonaccorso, F., et al., *Graphene, related two-dimensional crystals, and hybrid systems for energy conversion and storage.* Science, 2015. **347**(6217).

90.   Choi, H.-J., et al., *Graphene for energy conversion and storage in fuel cells and supercapacitors.* Nano Energy, 2012. **1**(4): p. 534-551.

91.   Brownson, D.A.C., D.K. Kampouris, and C.E. Banks, *An overview of graphene in energy production and storage applications.* Journal of Power Sources, 2011. **196**(11): p. 4873-4885.

92. Gwon, H., et al., *Flexible energy storage devices based on graphene paper.* Energy & Environmental Science, 2011. **4**(4): p. 1277.

93. Huang, G., et al., *Synthesis and electrochemical performances of cobalt sulfides/graphene nanocomposite as the anode material for Li-ion battery.* Journal of Power Sources, 2013. **235**: p. 122-128.

94. Zhao, Y., et al., the *Significant impact of 2D graphene nanosheets on large volume change tin-based anodes in lithium-ion batteries: A review.* Journal of Power Sources, 2015. **274**: p. 869-884.

95. Wang, Q., et al., *Facile Synthesis of Ultrasmall CoS2 Nanoparticles within Thin N-Doped Porous Carbon Shell for High-Performance Lithium-Ion Batteries.* Small, 2015. **11**(21): p. 2511-7.

96. Su, Q.M., et al., *In Situ Transmission Electron Microscopy Observation of Electrochemical Sodiation of Individual Co9S8-Filled Carbon Nanotubes.* ACS Nano, 2014. **8**(4): p. 3620-3627.

97. Peng, S., et al., *Unique Cobalt Sulfide/Reduced Graphene Oxide Composite as an Anode for Sodium-Ion Batteries with Superior Rate Capability and Long Cycling Stability.* Small, 2016. **12**(10): p. 1359-68.

98. Zhou, Q., et al., *Sandwich-like cobalt sulfide–graphene composite – an anode material with an excellent electrochemical performance for sodium ion batteries.* RSC Adv., 2015. **5**(88): p. 71644-71651.

99. Ko, Y.N., and Y.C. Kang, *Co9S8–carbon composite as anode materials with improved Na-storage performance.* Carbon, 2015. **94**: p. 85-90.

100. Zhou, L., et al., *Structural and chemical synergistic effect of CoS nanoparticles and porous carbon nanorods for high-performance sodium storage.* Nano Energy, 2017. **35**: p. 281-289.

101. Gu, W., et al., *Noble-metal-free Co3S4–S/G porous hybrids as an efficient electrocatalyst for oxygen reduction reaction.* Chem. Sci., 2016.

102. Feng, Y.J., T. He, and N. Alonso-Vante, *In situ free-surfactant synthesis and ORR-Electrochemistry of carbon-supported Co3S4 and CoSe2 nanoparticles.* Chemistry of Materials, 2008. **20**(1): p. 26-28.

103. Chen, Q., et al., *In situ shape and phase transformation synthesis of Co3S4 nanosheet arrays for high-performance electrochemical supercapacitors.* RSC Advances, 2013. **3**(45): p. 22922.

104. Xu, B., L. Pan, and Q. Zhu, *Synthesis of Co3S4 Nanosheets and Their Superior Supercapacitor Property.* Journal of Materials Engineering and Performance, 2016. **25**(3): p. 1117-1121.

105. Strauss, E., et al., *Lithium polymer electrolyte pyrite rechargeable battery: a comparative characterization of natural pyrite from different sources as cathode material.* Journal of Power Sources, 2000. **88**(2): p. 206-218.

106. Wu, H. and Y. Cui, *Designing nanostructured Si anodes for high energy lithium ion batteries.* Nano Today, 2012. **7**(5): p. 414-429.

107. Fan, H.H., et al., *Metastable Marcasite-FeS2 as a New Anode Material for Lithium Ion Batteries: CNFs-Improved Lithiation/Delithiation Reversibility and Li-Storage Properties.* ACS Appl Mater Interfaces, 2017. **9**(12): p. 10708-10716.

108. Liu, B., et al., *Low temperature synthesis of carbon encapsulated Fe7S8 nanocrystals as high performance anode for lithium-ion batteries.* Materials Chemistry and Physics, 2015. **151**: p. 60-65.

109. Wen, X., et al., *Self-assembled FeS2cubes anchored on reduced graphene oxide as an anode material for lithium ion batteries.* J. Mater. Chem. A, 2015. **3**(5): p. 2090-2096.

110. Xue, H., et al., *Pyrite FeS2microspheres wrapped by reduced graphene oxide as high-performance lithium-ion battery anodes.* J. Mater. Chem. A, 2015. **3**(15): p. 7945-7949.

111. Wen, X., et al., *Self-assembled FeS2 cubes anchored on reduced graphene oxide as an anode material for lithium ion batteries.* J. Mater. Chem. A, 2015. **3**(5): p. 2090-2096.

112. Liu, W.L., et al., *Solvothermal synthesis of pyrite FeS2nanocubes and their superior high rate lithium storage properties.* RSC Adv., 2014. **4**(90): p. 48770-48776.

113. Hu, Z., et al., *FeS2microspheres with an ether-based electrolyte for high-performance rechargeable lithium batteries.* J. Mater. Chem. A, 2015. **3**(24): p. 12898-12904.

114. Zheng, J., et al., *Facile synthesis of Fe3S4hollow spheres with high-performance for lithium-ion batteries and water treatment.* J. Mater. Chem. A, 2014. **2**(46): p. 19882-19888.

115. Li, W., et al., *Pyrite nanocrystals: shape-controlled synthesis and tunable optical properties via reversible self-assembly.* Journal of Materials Chemistry, 2011. **21**(44): p. 17946.

116. Hu, Z., et al., *Pyrite FeS2for high-rate and long-life rechargeable sodium batteries.* Energy Environ. Sci., 2015. **8**(4): p. 1309-1316.

117. He, Q., et al., *Fabrication of flexible MoS2 thin-film transistor arrays for practical gas-sensing applications.* Small, 2012. **8**(19): p. 2994-9.

118. Li, Y., et al., *MoS2 nanoparticles grown on graphene: an advanced catalyst for the hydrogen evolution reaction.* J Am Chem Soc, 2011. **133**(19): p. 7296-9.

119. Ou, J.Z., et al., *Ion-driven photoluminescence modulation of quasi-two-dimensional MoS2 nanoflakes for applications in biological systems.* Nano Lett, 2014. **14**(2): p. 857-63.

120. Radisavljevic, B., et al., *Single-layer MoS2 transistors.* Nat Nanotechnol, 2011. **6**(3): p. 147-50.

121. Lopez-Sanchez, O., et al., *Ultrasensitive photodetectors based on monolayer MoS2.* Nat Nanotechnol, 2013. **8**(7): p. 497-501.

122. Acerce, M., D. Voiry, and M. Chhowalla, *Metallic 1T phase MoS2 nanosheets as supercapacitor electrode materials*. Nature Nanotechnology, 2015. **10**(4): p. 313-318.

123. Wu, W., et al., *Piezoelectricity of single-atomic-layer MoS2 for energy conversion and piezotronics*. Nature, 2014. **514**(7523): p. 470-4.

124. Roy, K., et al., *Graphene-MoS2 hybrid structures for multifunctional photoresponsive memory devices*. Nat Nanotechnol, 2013. **8**(11): p. 826-30.

125. Gao, P., et al., *Facile synthesis of MoS2/MWNT anode material for high-performance lithium-ion batteries*. Ceramics International, 2015. **41**(1): p. 1921-1925.

126. Yang, E., H. Ji, and Y. Jung, *Two-Dimensional Transition Metal Dichalcogenide Monolayers as Promising Sodium Ion Battery Anodes*. The Journal of Physical Chemistry C, 2015. **119**(47): p. 26374-26380.

127. Li, H., et al., *MoS2/Graphene Hybrid Nanoflowers with Enhanced Electrochemical Performances as Anode for Lithium-Ion Batteries*. The Journal of Physical Chemistry C, 2015. **119**(14): p. 7959-7968.

128. Zhang, L., et al., *Hierarchical MoS2 microboxes constructed by nanosheets with enhanced electrochemical properties for lithium storage and water splitting*. Energy Environ. Sci., 2014. **7**(10): p. 3302-3306.

129. Ma, L., et al., *Cationic surfactant-assisted hydrothermal synthesis of few-layer molybdenum disulfide/graphene composites: Microstructure and electrochemical lithium storage*. Journal of Power Sources, 2014. **264**: p. 262-271.

130. Li, J., et al., *A three-dimensionally interconnected carbon nanotube/layered MoS2 nanohybrid network for lithium ion battery anode with superior rate capacity and long-cycle-life*. Nano Energy, 2015. **16**: p. 10-18.

131. Chang, K., et al., *Ultrathin MoS2/Nitrogen-Doped Graphene Nanosheets with Highly Reversible Lithium Storage*. Advanced Energy Materials, 2013. **3**(7): p. 839-844.

132. Bang, G.S., et al., *Effective liquid-phase exfoliation and sodium ion battery application of MoS2 nanosheets*. ACS Appl Mater Interfaces, 2014. **6**(10): p. 7084-9.

133. Hu, Z., et al., *MoS2 Nanoflowers with Expanded Interlayers as High-Performance Anodes for Sodium-Ion Batteries*. Angewandte Chemie, 2014. **126**(47): p. 13008-13012.

134. Choi, S.H., et al., *3D MoS2-Graphene Microspheres Consisting of Multiple Nanospheres with Superior Sodium Ion Storage Properties*. Advanced Functional Materials, 2015. **25**(12): p. 1780-1788.

135. Li, Y., et al., *Enhancing sodium-ion battery performance with interlayer-expanded MoS2–PEO nanocomposites*. Nano Energy, 2015. **15**: p. 453-461.

136.   Tang, Y., et al., *Ultrasmall MoS2 Nanosheets Mosaiced into Nitrogen-Doped Hierarchical Porous Carbon Matrix for Enhanced Sodium Storage Performance.* Electrochimica Acta, 2017. **225**: p. 369-377.

137.   Jiang, X., et al., *In situ assembly of graphene sheets-supported SnS2 nanoplates into 3D macroporous aerogels for high-performance lithium ion batteries.* Journal of Power Sources, 2013. **237**: p. 178-186.

138.   Wu, Q., et al., *One-pot synthesis of three-dimensional SnS2 hierarchitectures as anode material for lithium-ion batteries.* Journal of Power Sources, 2013. **239**: p. 89-93.

139.   Bhaskar, A., M. Deepa, and T.N. Rao, *Tin Disulfide Nanoflowers versus Nanosheets as Anodes in Lithium-ion Batteries: How the Nanostructure Controls Performance.* Electrochimica Acta, 2015. **184**: p. 239-249.

140.   Zhu, C., et al., *A General Strategy to Fabricate Carbon-Coated 3D Porous Interconnected Metal Sulfides: Case Study of SnS/C Nanocomposite for High-Performance Lithium and Sodium Ion Batteries.* Advanced Science, 2015: p. n/a-n/a.

141.   Mei, L., et al., *Superior electrochemical performance of ultrasmall SnS2 nanocrystals decorated on flexible RGO in lithium-ion batteries.* Journal of Materials Chemistry A, 2013. **1**(30): p. 8658.

142.   Qu, B., et al., *Layered SnS2-reduced graphene oxide composite--a high-capacity, high-rate, and long-cycle life sodium-ion battery anode material.* Adv Mater, 2014. **26**(23): p. 3854-9.

143.   Liu, S.A., et al., *Chemical bath deposition of SnS2 nanowall arrays with improved electrochemical performance for lithium ion battery.* Materials Letters, 2010. **64**(21): p. 2350-2353.

144.   Zhu, Y.Q., Y.Q. Chen, and L.Z. Liu, *Effect of ethylene glycol on the growth of hexagonal SnS2 nanoplates and their optical properties.* Journal of Crystal Growth, 2011. **328**(1): p. 70-73.

145.   Petkov, N., et al., *Confined growth and crystallography of one-dimensional Bi2S3, CdS, and SnSx nanostructures within channeled substrates.* Journal of Physical Chemistry C, 2008. **112**(19): p. 7345-7355.

146.   Lin, Y.T., et al., *Synthesis and Characterization of Tin Disulfide (SnS2) Nanowires.* Nanoscale Research Letters, 2009. **4**(7): p. 694-698.

147.   Feng, J.J., et al., *Two-dimensional hexagonal SnS2 nanoflakes: fabrication, characterization, and growth mechanism.* Applied Physics a-Materials Science & Processing, 2011. **103**(2): p. 413-419.

148.   Shi, W. and B.A. Lu, *Nanoscale Kirkendall Effect Synthesis of Echinus-like SnO2@SnS2 Nanospheres as High Performance Anode Material for Lithium Ion Batteries.* Electrochimica Acta, 2014. **133**: p. 247-253.

149. He, M., L.X. Yuan, and Y.H. Huang, *Acetylene black incorporated three-dimensional porous SnS2 nanoflowers with high performance for lithium storage (vol 3, pg 3374, 2013).* RSC Advances, 2013. **3**(48): p. 26474-26474.

150. Sun, H., et al., *SnS2 nanoflakes decorated multiwalled carbon nanotubes as high performance anode materials for lithium-ion batteries.* Materials Research Bulletin, 2014. **49**: p. 319-324.

151. Wang, L., et al., *High-rate performance of SnS2 nanoplates without carbon-coating as anode material for lithium ion batteries.* Electrochimica Acta, 2013. **112**: p. 439-447.

152. Li, J., et al., *Mesoporous carbon anchored with SnS2 nanosheets as an advanced anode for lithium-ion batteries.* Electrochimica Acta, 2013. **111**: p. 862-868.

153. Luo, B., et al., *Two dimensional graphene–SnS2 hybrids with superior rate capability for lithium ion storage.* Energy Environ. Sci., 2012. **5**(1): p. 5226-5230.

154. Jiang, Z., et al., *In situ synthesis of SnS2@graphene nanocomposites for rechargeable lithium batteries.* Journal of Materials Chemistry, 2012. **22**(19): p. 9494.

155. Kong, D., et al., *A novel SnS2@graphene nanocable network for high-performance lithium storage.* RSC Advances, 2014. **4**(45): p. 23372.

156. Wang, G., et al., *Two-dimensional SnS2@PANI nanoplates with high capacity and excellent stability for lithium-ion batteries.* J. Mater. Chem. A, 2015. **3**(7): p. 3659-3666.

157. Wu, L., et al., *Improved sodium-storage performance of stannous sulfide@reduced graphene oxide composite as high capacity anodes for sodium-ion batteries.* Journal of Power Sources, 2015. **293**: p. 784-789.

158. Prikhodchenko, P.V., et al., *Nanocrystalline tin disulfide coating of reduced graphene oxide produced by the peroxostannate deposition route for sodium ion battery anodes.* Journal of Materials Chemistry A, 2014. **2**(22): p. 8431.

159. Liu, Y., et al., *Homogeneously assembling like-charged WS2 and GO nanosheets lamellar composite films by filtration for highly efficient lithium-ion batteries.* Nano Energy, 2014. **7**: p. 25-32.

160. Wang, S., et al., *Synthesis and Characterization of Cobalt-Doped WS2 Nanorods for Lithium Battery Applications.* Nanoscale Res Lett, 2010. **5**(8): p. 1301-6.

161. Feng, C., et al., *Synthesis of tungsten disulfide (WS2) nanoflakes for a lithium-ion battery application.* Electrochemistry Communications, 2007. **9**(1): p. 119-122.

162. Liu, H., et al., *An ordered mesoporous WS2 anode material with superior electrochemical performance for lithium ion batteries.* Journal of Materials Chemistry, 2012. **22**(34): p. 17437.

163.   Shiva, K., et al., *Employing synergistic interactions between few-layer WS2 and reduced graphene oxide to improve lithium storage, cyclability and rate capability of Li-ion batteries.* Nano Energy, 2013. **2**(5): p. 787-793.

164.   Du, Y., et al., *Improving the Anode Performance of WS2 through a Self-Assembled Double Carbon Coating.* The Journal of Physical Chemistry C, 2015. **119**(28): p. 15874-15881.

165.   Zhu, C., et al., *Engineering nanostructured electrode materials for high-performance sodium ion batteries: a case study of a 3D porous interconnected WS2/C nanocomposite.* J. Mater. Chem. A, 2015. **3**(41): p. 20487-20493.

166.   Chen, D., et al., *3-D graphene cross-linked with mesoporous MnS clusters with high lithium storage capability.* Scripta Materialia, 2014. **76**: p. 1-4.

167.   Riha, S.C., et al., *Atomic Layer Deposition of MnS: Phase Control and Electrochemical Applications.* ACS Appl Mater Interfaces, 2016. **8**(4): p. 2774-80.

168.   Mahmood, N., C. Zhang, and Y. Hou, *Nickel Sulfide/Nitrogen-Doped Graphene Composites: Phase-Controlled Synthesis and High-Performance Anode Materials for Lithium Ion Batteries.* Small, 2013. **9**(8): p. 1321-1328.

169.   Hou, H., et al., *One-Dimensional Rod-Like Sb(2)S(3)-Based Anode for High-Performance Sodium-Ion Batteries.* ACS Appl Mater Interfaces, 2015. **7**(34): p. 19362-9.

170.   Du, X., et al., *Core-shell structured ZnS-C nanoparticles with enhanced electrochemical properties for high-performance lithium-ion battery anodes.* Electrochimica Acta, 2017. **225**: p. 129-136.

171.   Su, D., K. Kretschmer, and G. Wang, *Improved Electrochemical Performance of Na-Ion Batteries in Ether-Based Electrolytes: A Case Study of ZnS Nanospheres.* Advanced Energy Materials, 2016. **6**(2): p. n/a/a.

172.   Li, J., et al., *In situ growth of Sb2S3 on multiwalled carbon nanotubes as high-performance anode materials for sodium-ion batteries.* Electrochimica Acta, 2017. **228**: p. 436-446.

173.   Dong, S., et al., *ZnS-Sb2S3@C Core-Double Shell Polyhedron Structure Derived from Metal-Organic Framework as Anodes for High-Performance Sodium Ion Batteries.* ACS Nano, 2017. **11**(6): p. 6474-6482.

174.   Liu, X., et al., *A binary metal-organic framework derived hierarchical hollow Ni3S2/Co9S8/N-doped carbon composite with superior sodium storage performance.* J. Mater. Chem. A, 2017. **5**(23): p. 11781-11787.

175.   Chen, Z., et al., *Construction of Hybrid Hollow Architectures by In-situ Rooting Ultrafine ZnS Nanorods within Porous Carbon Polyhedra for Enhanced Lithium Storage Properties.* Chemical Engineering Journal, 2017.

176.   Qiu, B., X. Zhao, and D. Xia, *In situ synthesis of CoS2/RGO nanocomposites with enhanced electrode performance for lithium-ion batteries*. Journal of Alloys and Compounds, 2013. **579**: p. 372-376.

177.   Xing, C., et al., *In situ growth of FeS micro sheet networks with enhanced electrochemical performance for lithium-ion batteries*. J. Mater. Chem. A, 2015. **3**(16): p. 8742-8749.

178.   Xu, C., et al., *Controlled Soft-Template Synthesis of Ultrathin C@FeS Nanosheets with High-Li-Storage Performance*. ACS Nano, 2012. **6**(6): p. 4713-4721.

179.   Zhang, K., et al., *A potential pyrrhotite (Fe7S8) anode material for lithium storage*. RSC Adv., 2015. **5**(19): p. 14828-14831.

180.   Zhou, X., et al., *Facile synthesis and electrochemical properties of two dimensional layered MoS2/graphene composite for reversible lithium storage*. Journal of Power Sources, 2014. **251**: p. 264-268.

181.   Zhang, C., et al., *Facile synthesis of carbon-coated MoS2 nanorods with enhanced lithium storage properties*. Electrochemistry Communications, 2012. **20**: p. 7-10.

182.   Pan, L., et al., *Delicate ternary heterostructures achieved by hierarchical co-assembly of Ag and Fe3O4 nanoparticles on MoS2 nanosheets: morphological and compositional synergy in reversible lithium storage*. J. Mater. Chem. A, 2015. **3**(6): p. 2726-2733.

183.   Zhian Zhang, Y.G., Yanqing Laia,*, Xiaodong Shia, Wei Chena, Jie Li, *<Cobalt sulfides/dodecahedral porous carbon as anode materials for Na-ion batteries.pdf>*. RSC Advances, 2015: p. 1-4.

184.   Qin, W., et al., *MoS2-reduced graphene oxide composites via microwave assisted synthesis for sodium ion battery anode with improved capacity and cycling performance*. Electrochimica Acta, 2015. **153**: p. 55-61.

185.   Xu, W., et al., *SnS2@Graphene nanosheet arrays grown on carbon cloth as freestanding binder-free flexible anodes for advanced sodium batteries*. Journal of Alloys and Compounds, 2016. **654**: p. 357-362.

186.   Yu, D.Y., et al., *High-capacity antimony sulphide nanoparticle-decorated graphene composite as anode for sodium-ion batteries*. Nat Commun, 2013. **4**: p. 2922.

187.   Rout, C.S., et al., *Synthesis and characterization of patronite form of vanadium sulfide on graphitic layer*. J Am Chem Soc, 2013. **135**(23): p. 8720-5.

188.   Choi, S.H. and Y.C. Kang, *Synergetic compositional and morphological effects for improved Na(+) storage properties of Ni(3)Co(6)S(8)-reduced graphene oxide composite powders*. Nanoscale, 2015. **7**(14): p. 6230-7.

189.   Xiangbo Meng a, S.C.R.b., Joseph A. Libera a, Qingliu Wu c, Hsien-Hau Wang b, and J.W.E.a. Alex B.F. Martinson b, *, *Tunable core-shell single-walled carbon nanotube-Cu2S networked nanocomposites as high-performance cathodes for lithium-ion*

batteries. Journal of Power Sources, 2015. **280**: p. 612-629.

190.   Meng, X., X.Q. Yang, and X. Sun, *Emerging applications of atomic layer deposition for lithium-ion battery studies.* Adv Mater, 2012. **24**(27): p. 3589-615.

191.   Meng, X., *Towards high-energy and durable lithium-ion batteries via atomic layer deposition: elegantly atomic-scale material design and surface modification.* Nanotechnology, 2015. **26**(2): p. 020501.

192.   Zou, R., et al., *Three-dimensional-networked NiCo2S4 nanosheet array/carbon cloth anodes for high-performance lithium-ion batteries.* NPG Asia Materials, 2015. **7**(6): p. e195.

Chapter 3

3. Experimental procedures

3.1. Synthesis process

In this chapter, different synthesis approaches, including wet chemical process, hydrothermal, method and chemical vapor deposition, were used to design different nanomaterials and nanostructures. These three methods will be defined and described in this chapter. Also, the appropriate techniques were used to study the physical and electrochemical performance.

3.1.1. Wet chemical process

The wet chemical process represents several methods including sol-gel process, hydrothermal synthesis, spray drying, aerosol spray pyrolysis, etc. to synthesize nanostructured materials. It is a liquid phase process where different powders are dissolved in a various solvent (e.g., nitrides, chlorides) at room temperature or relatively higher temperature to obtain a solid material. During the process, different parameters such as time, temperature, reactant concentration, and stirring speed, etc. can be precisely controlled to achieve the controllable nanostructure materials. The advantages of this approach can be list as: well-defined structures can be obtained, the controllable parameter could be maintained, safe at room temperature or relatively higher, cheap.

3.1.2. Hydrothermal synthesis
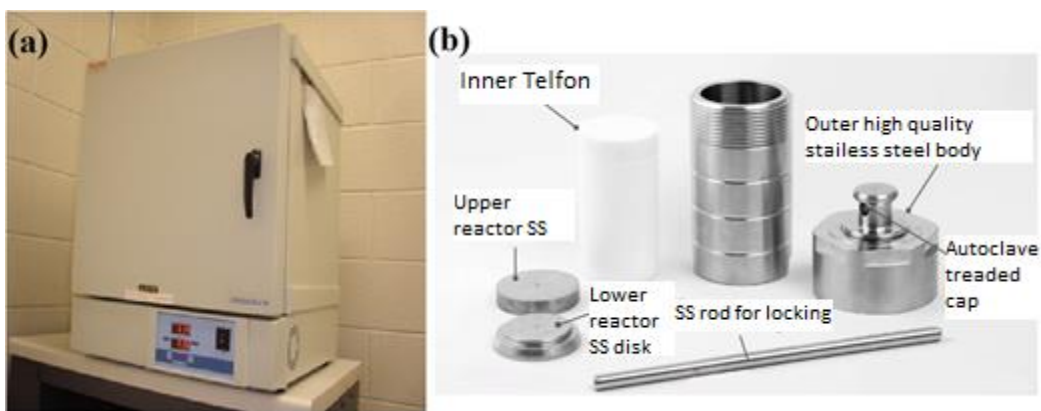
Figure 3-1 (a) hydrothermal oven (b) Teflon lined hydrothermal reactor [3].

Besides the general wet chemical process, it is considered that the extra pressure will also affect the final products during the reaction. In this case, hydrothermal/ solvothermal methods are developed to fabricate nanostructure materials. The specific reactor made of Polytetrafluoroethylene (PTFE) is placed inside Teflon Lined Stainless Steel Autoclave as shown

in **Figure 3.1b** and the heating ovens will be used to obtain relatively high temperature and pressure (see **Figure 3.1a**). The advantages of this approach could be highlighted as the ability to synthesize high crystallinity materials with very uniform morphologies, highly controllable process.

3.1.3. Chemical vapor decomposition (CVD)
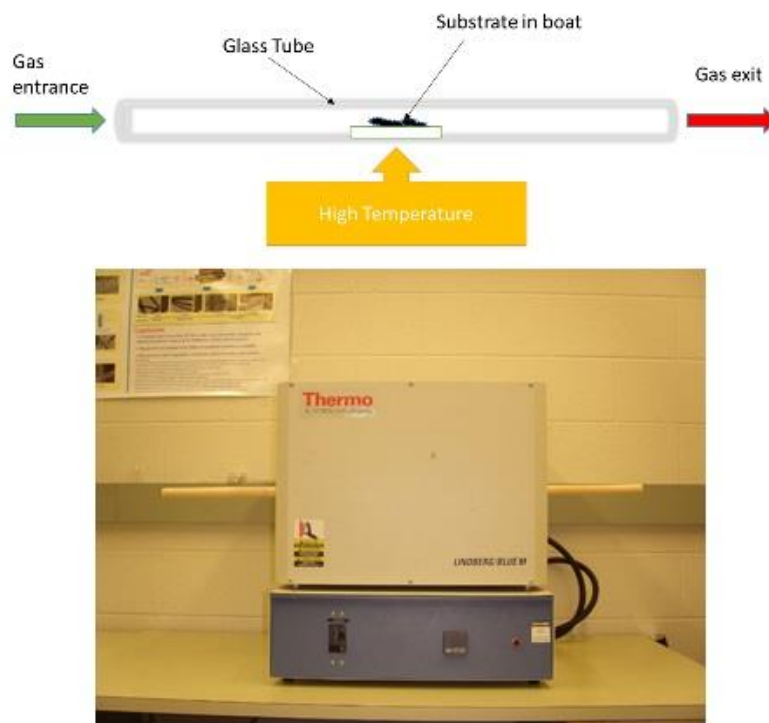
Figure 3-2 schematic illustration of chemical Vapor deposition process and the oven used for it

CVD is a process that is suitable to synthesize the vast amount of different materials such as metal, carbon materials including nanotubes and nanowires, composite materials and ceramics. It is a process in which the substrate is exposed to one or more volatile precursors flowing within a carrier gas to be deposited on the surface at a high temperature of between 600 and 800°C and using glass for example in an oven that is shown in **Figure 3.2.** The substrate is put in a small boat and heated up to specific temperature based on the different materials and reactions in the presence of precursor that is introduced into the flowing gas.

3.2. Characterization Method
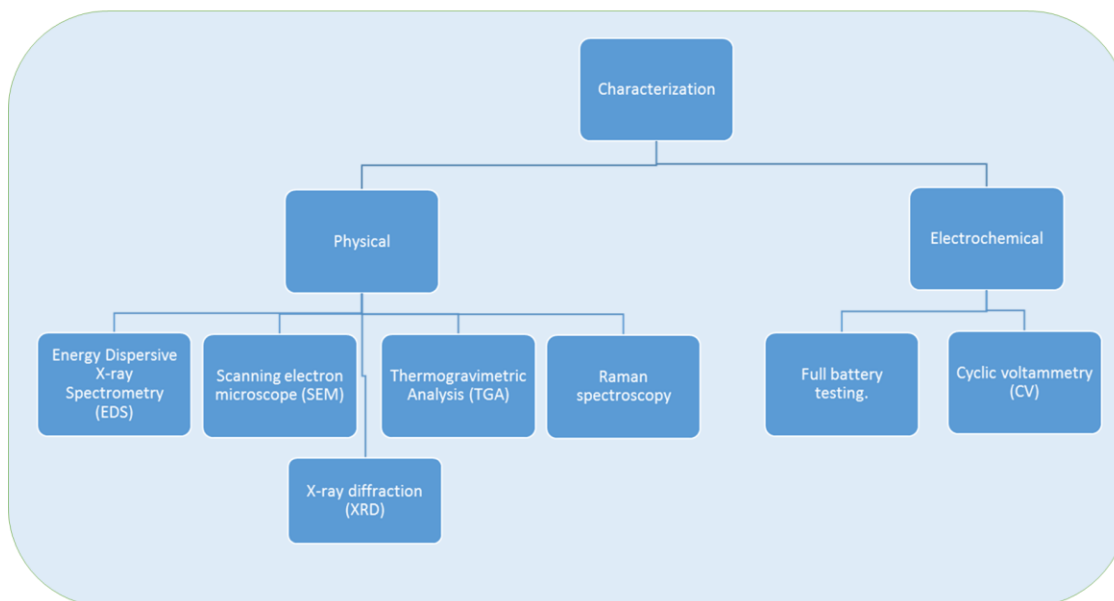
Figure 3-3 Flowchart shows characteristic techniques in this work

Characterization method, in general, is divided into two parts in this thesis: physical characterization and electrochemical characterization. Firstly, physical properties including morphologies, chemical composition, and structural properties, are investigated using several powerful techniques such as Scanning Electron Microscope (SEM), Energy Dispersive X-ray Spectrometry (EDS), Raman spectroscopy (Raman), X-ray diffraction (XRD), and Thermogravimetric Analysis (TGA). Secondly, the electrochemical characterization is the way to evaluating the batteries performance using cyclic voltammetry (CV), and full battery testing as all classification is shown in the flow chart below (**see Figure 3.3**).

3.2.1. Physical Characterization techniques

3.2.1.1. Scanning electron microscopy (SEM)
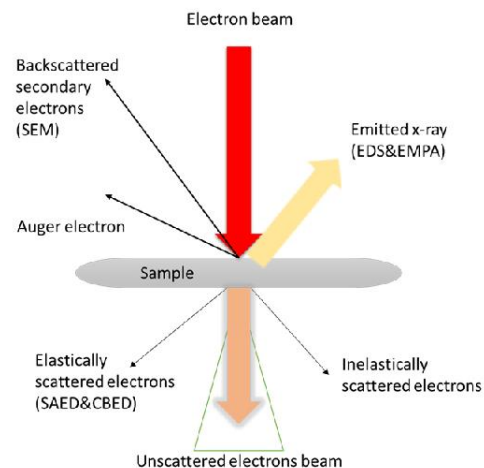
Figure 3-4 on the left, Digital photo of SEM (Hitachi, S-4800) machine; on the right, Types of interactions between electrons and a sample.

SEM is a scanning device using an electron beam to image the surface of materials. The detectors receive signals with the surface information as a result of electrons interaction with sample's atoms. As it is shown in **Figure 2.4**, On the right side, a narrow electron beam is released from the electron gun at a very high voltage to interact with the sample surface. When penetrating into the material, different electrons are produced and reflected in different directions which are X-rays, Auger electrons, backscattered, secondary electrons, elastically scattered electrons, and inelastically scattered electrons. Mainly, the backscattered electrons are the one responsible for imaging SEM information. Detectors collect the information and convert it to TV scanner to produce the image. The morphological studies in this research are performed by Hitachi S-4800 field-emission scanning electron microscope **(SEM) (see Figure 3.4)**. The produced electrons and characteristic x-ray can be detected using various detectors providing information about the morphology and composition of the samples.

3.2.1.2. Energy Dispersive X-ray Spectrometry (EDX)

Energy Dispersive X-ray Spectrometry (EDX) is an analytical technique that is used to obtain a localized chemical analysis and element distribution images or "maps" by scanning the beam in a television-like raster and displaying the intensity of a selected X-ray line. The scanning

electron microscope (SEM) is designed primarily for producing electron images, but can also be in conjunction with EDX and used for element mapping, and even point analysis if an X-ray spectrometer is added which is the case in the SEM (Hitachi, S-4800) machine shown in **Figure 3.4.**

3.2.1.3. Raman spectroscopy
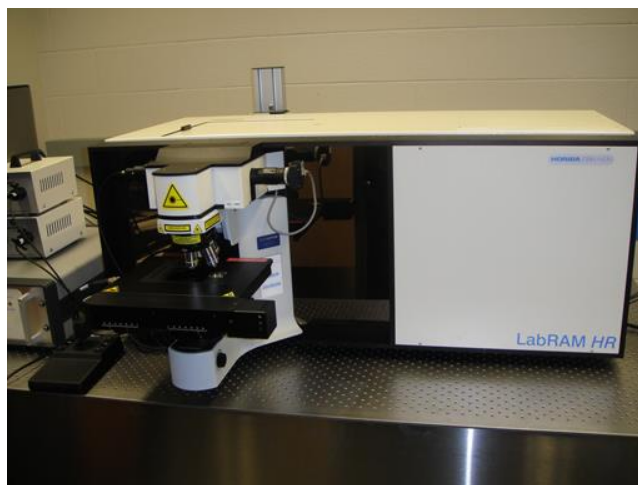
Figure 3-5 Digital photo of HORIBA Scientific LabRAM HR Raman spectrometer.

Raman spectroscopy is a spectroscopic technique used to provide information about the chemical structure and physical forms by investigating the photon energy shift that is caused by the interaction between the laser light and the molecular vibrations to study the vibrational, rotational information of chemical bonds in materials. When light interacts with the molecule, a temporary state called "virtual state" is produced which is not a real state of the molecules, and it is not stable which photon is quickly re-radiated. Raman scattering spectra were collected on a HORIBA Scientific LabRAM HR Raman spectrometer system equipped with a 532.4 nm laser, as shown in **Figure 3.5**. Raman spectrum is presented as an intensity versus wavelength shift, and its spectra could be recorded over a range of 4000–10 cm^{-1}(10) and the ratio between peaks at ~ 1345 cm^{-1} (D band) and ~ 1570 cm^{-1} (G band) is used to evaluate the disorder in the carbon materials.

3.2.1.4. X-ray diffraction (XRD)

Figure 3-6 Digital photo of Bruker D8 Advance XRD machine.

X-ray diffraction (XRD) is a technique used to examine detailed information of crystal structure, chemical composition and physical properties of materials. These X-rays are produced by a cathode ray tube, filtered to generate concentrated monochromatic radiation and focused on the sample. The interaction of the monochromatic x-ray beam with the sample produces diffracted ray when it satisfies the relationship shown in Bragg's Law (nλ=2d sin θ). Where; λ is the wavelength, n is the diffraction angle, and d is the spacing of the lattice planes, and these diffracted x-rays are detected, counted, processed and converted to a count rate which is being sent to a device such as a printer or a computer monitor. The XRD patterns were obtained from a Bruker D8 Discover diffractometer employing a Co- Kα source, as shown in **Figure 3.6**.

3.2.1.5. Thermogravimetric Analysis
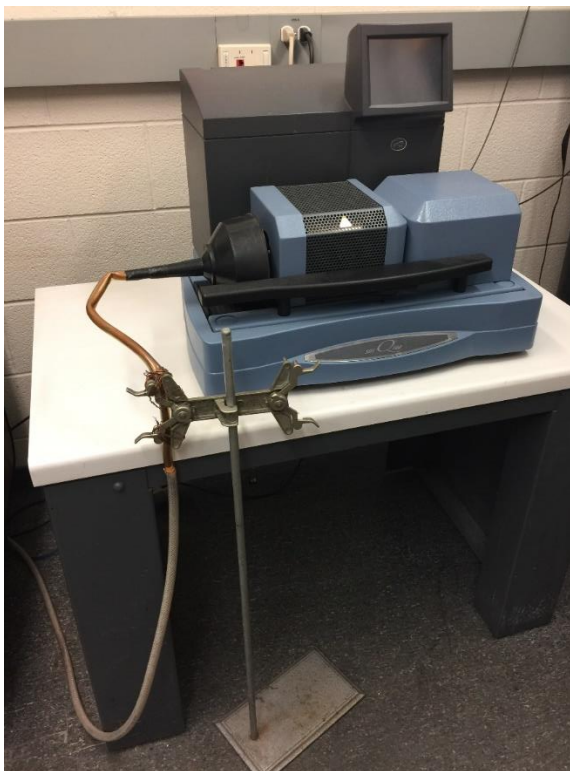
Figure 3-7 Digital photo of Thermogravimetric Analysis device taken at the lab.

Thermogravimetric Analysis is a technique in which the mass of a substance is examined as a function of temperature or time in different environments to know the content of the material. Herein, the material is heated up to a specific temperature for a particular time under nitrogen or air stream to investigate the physical and chemical properties such as the carbon content of the material in the pristine materials contain carbon for example by monitoring the weight lost during the process **(See Figure 3.7)**.

3.2.2. Electrochemical characterizations

3.2.2.1. Battery assembly

Figure 3-8 Digital photo of Lithium battery glove box.

Coin-type half-cells consist of a prepared electrode as an anode, a polypropylene separator (Celgard 2400). The battery assembly was done using coin cells in a glove box in Vacuumed Atmospheres under a dry argon atmosphere (concentrations of moisture and oxygen are below 1 ppm) (**See Figure 3.8**). The electrode was prepared using a weight ratio of 7:2:1 of active electrode material, carbon black, and binder all mixed in Dimethylformamide (DMF) solvent. After the uniform slurry is obtained, it is painted on copper foil. Lithium foil as the cathode for LIB and the electrolyte used in LIB consists of 1M $LiPF_6$ dissolved in ethylene carbonate (EC): diethyl carbonate (DEC): ethyl methyl carbonate (EMC) in a volume ratio of 1:1:1.

Sodium foil as a cathode for SIBs and the electrolyte used in SIBs consist of 1.0 m $NaCF_3 SO_3$ in diethylene glycol dimethyl ether (DEGDME)[1].

3.2.2.2. Electrochemical cycling test

Figure 3-9 Digital photo of Arbin BT-2000 battery test station.

Cycling performance was performed at the same parameter for both batteries at current density 100 mA g^{-1} in a voltage range between 0.0-3V. For rate tests, current densities of 100, 200, 300, 500, and 1000mA g^{-1} are employed to all batteries rate performances. Cycling stability and rate capability of the anode materials are investigated in an Arbin BT-2000 battery test station **(See Figure 3.9).**

3.2.2.3. Cyclic Voltammetry (CV)
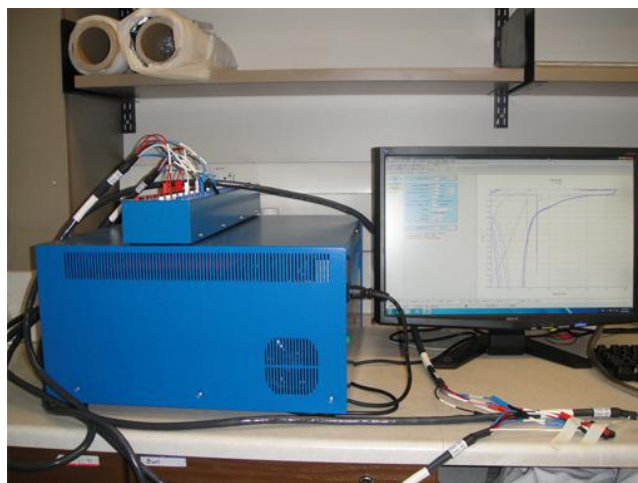
Figure 3-10 A picture of VMP3 Potentiostat/Galvanostat/EIS system.

Cyclic Voltammetry (CV) is an electrochemical technique that measures the current that develops in an electrochemical cell under conditions where the voltage is fixed in a specific range [2]. CV is a technique rely on measuring the current by cycling the potential. CV performance of the anode materials of both LIBs and SIBs in this research is evaluated over a voltage range of 0.0-3V in a VMP3 Potentiostat/Galvanostat/EIS system shown in Figure 2.10.

References

1.Peng, S., et al., Unique Cobalt Sulfide/Reduced Graphene Oxide Composite as an Anode for Sodium-Ion Batteries with Superior Rate Capability and Long Cycling Stability. Small, 2016. 12(10): p. 1359-68.

2.Heineman, P.T.K.a.W.R., Cyclic voltammetry. J. Chem. Educ, 1983. (9)(60): p. 702.

3.   http://www.toptiontech.com/laboratory-reactor/hydrothermal-reactor/teflon-lined-hydrothermal-synthesis-autoclave.html

Chapter 4

4. Fabrication of Different Types of Metal-Organic Frameworks

Abstract

This chapter emphasizes the experimental procedures to synthesize different types of metal-organic frameworks (MOFs) such as zeolitic imidazolate framework-8 (ZIF-8) and (ZIF-67) and Materials from Institut Lavoisier(MIL-88). Primarily, the fabrication of MIL-88 has been discussed in detail with different effects and parameters such as temperature, time, solvent, reactant concentration, and additives on the material structures and morphology. A visual study using scanning electron microscopy (SEM) is performed to observe different changes of MIL-88 morphology due to adjusting different parameters. Finally, the best condition and parameters of preparing MIL-88 with high crystallinity, uniform distribution and small particle size were given to conclude this work.

4.1. Introduction

Metal-organic frameworks (MOFs) is a combination of metal ions linked by organic ligands owing crystal structures with high porosity. This material has unique properties such as the nearly highest surface areas reported in the literature, high thermal stability up to 500˚C because of their strong bonds, as well as the wide range of different structures and metals [1, 2]. These attractive properties render this material and their derivatives for many applications including chemical separation, filtering, sensing, energy storage and conversion, and catalysis.

However, the controllable synthesis of MOFs with defined structures and morphologies are still significant challenges. Controlling the morphology features such as surface area, porosity, and crystallinity involves adjusting different parameters such as the solvent used in the reactions, the reactions temperature, time, and others which could have a considerable influence on the synthesis process. All these challenges show that this field needs more effort to be done to explore this class of materials and have a better understanding of their chemical and thermal stability during the preparation. [3].

One of the favorite applications of MOFs is for energy storage and conversion especially as electrodes for batteries. This field has become a very hot area for research due to the urgent need to the reliable storage device for clean energy storing. Recently, MOFs and MOFs derived materials have been employed as electrodes materials for lithium ion, sodium ion, and lithium-sulfur batteries, etc., showing very promising potential. [4-7].

In this chapter, synthesis of different types of MOFs (ZIF8, ZIF67, MIL88) is explained and synthetic parameter effect is studied. Also, some characterization investigation was carried out to evaluate the success of the preparation process and determine the chemical-physical and properties of the materials.

4.2. Experimental procedures

4.2.1. Synthesis of Zeolitic imidazolate frameworks (ZIF-8)

6.1467 g of zinc nitrate $(Zn(NO_3)_2).6H_2O$ was dissolved in 250ml of methanol, forming solution A. Then, 6.7873g of 2-methylimidazole was dissolved in another 250ml of methanol, forming solution B. After that, solution A was dropwisely added into solution B under stirring at room temperature. After stirring for 1h, the reaction was aged overnight at room temperature. The White resultant precipitate was collected using a centrifuge and washed many times with ethanol.

4.2.2. Synthesis of Zeolitic imidazolate frameworks (ZIF-67)

6.0132g of zinc nitrate $(Co(NO_3)_2).6H_2O$ in 250ml of methanol, dropwise is added to 6.7873g of 2-methylimidazole in 250ml methanol under stirring at room temperature. After stirring for 1hr, the reaction is aged overnight at room temperature. The resultant purple precipitate is collected using a centrifuge and washed several times with ethanol. The particle size of ZIF67 obtained from this route was between 200-300nms. Smaller particle size is obtained from the slightly different route that is mixing 3.0066g of $(Co(NO_3)_2).6H_2O$ and 3.393g of 2-methylimidazole in 500ml of methanol that was put in an oil bath at 70°C under stirring for 15mins. Then the reaction is aged at room temperature over the night, and the Purple precipitate is collected the same previous method. An average particle size of 150nm is successfully obtained through this method. As shown in

4.2.3. Synthesis of Iron-based MOF (MIL-88)

0.2903g of $FeCl_3.6H_2O$ 0.1661g of 1,4-benzene dicarboxylic acid (H_2bdc) were dissolved in 10 ml of DMF in the reactor and stirred until the solution is obvious. The reactor was moved into the Teflon-lined autoclave and heated up to specified temperature and for a specified time. The detailed parameters including temperature, Time, Solvent type and concentration, and additives will be discussed in the following sections.

4.3. Results and discussion

4.3.1. Characterization for ZIF-8 and ZIF-67

Schematic illustration of ZIF-8 is shown in **Figure 4.1**, and the morphology of ZIF-8 was confirmed and demonstrated using the SEM images. As shown in **Figure 4.1**, SEM images of ZIF-8 shows a uniform distribution of rhombic dodecahedral structure with an average size of 200nm is observed. As-prepared ZIF-8 will be further used as the template for ZnS in the following chapters.
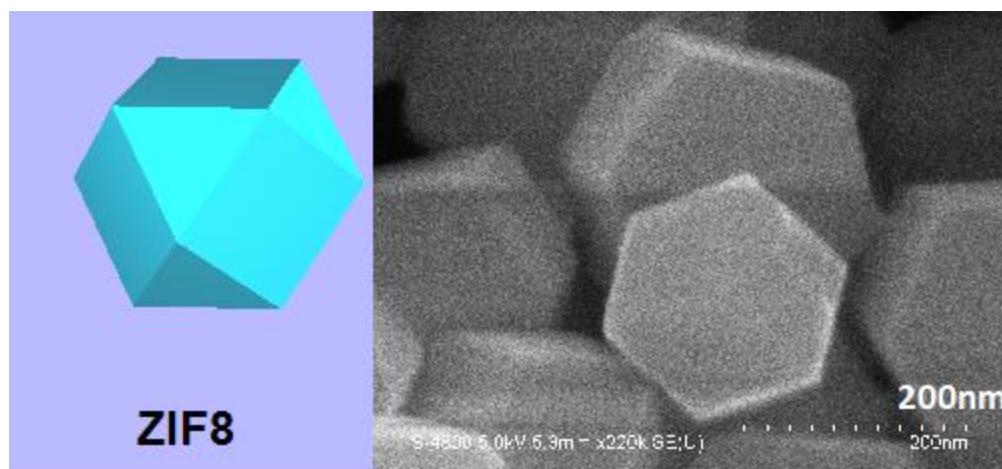
Figure 4-1 Schematic diagram of Zeolitic imidazolate frameworks (ZIF-8) with SEM image.

The SEM images of ZIF-67 was shown in Figure.3.2. From the SEM images, it can be observed that the ZIF-67 delivers the similar polyhedral morphology with ZIF-8 with a particle size range between 100-200nm and very smooth surface and uniform distribution. XRD tests were employed to confirm the structure and phase purity of ZIF-67. The XRD patterns of ZIF-67 matched the PDF card number in the index and previous publications. ZIF-67 is cobalt based MOF material that has been successfully used as a template to design nanostructures of cobalt oxides and cobalt sulfides with some inherited properties of MOFs such as high surface area, thermal stability, and morphology[8].
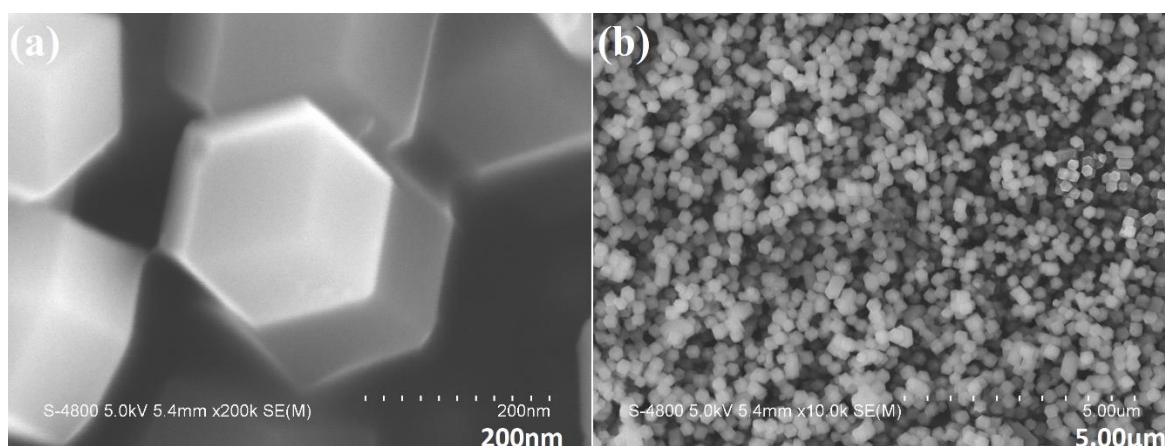
Figure 4.1-2 SEM images of Zeolitic imidazolate frameworks (ZIF-67); (a) high resolution (b) low resolution.

4.3.2.   The fabrication and detailed parameters for MIL-88

Iron (III) based MOFs is fascinating material that has been reported and applied in many application such as energy applications[9, 10], chemical adsorption and delivery [11], and dye degradation[12]. Iron-based MOFs consist of iron metal oxide cluster connected by organic linkers in three dimensions. MIL-88 is one of the critical type of iron-based MOFs with the diamond-like shape prepared using the hydrothermal method. Synthesis process and study of the synthetic parameter effect on the morphology is discussed in this section. As shown in **Figure 4.3**, schematic demonstration of the typical morphology of diamond-like MIL-88 and on the right side of the figure is SEM image of the prepared MIL-88 after synthesis optimization.
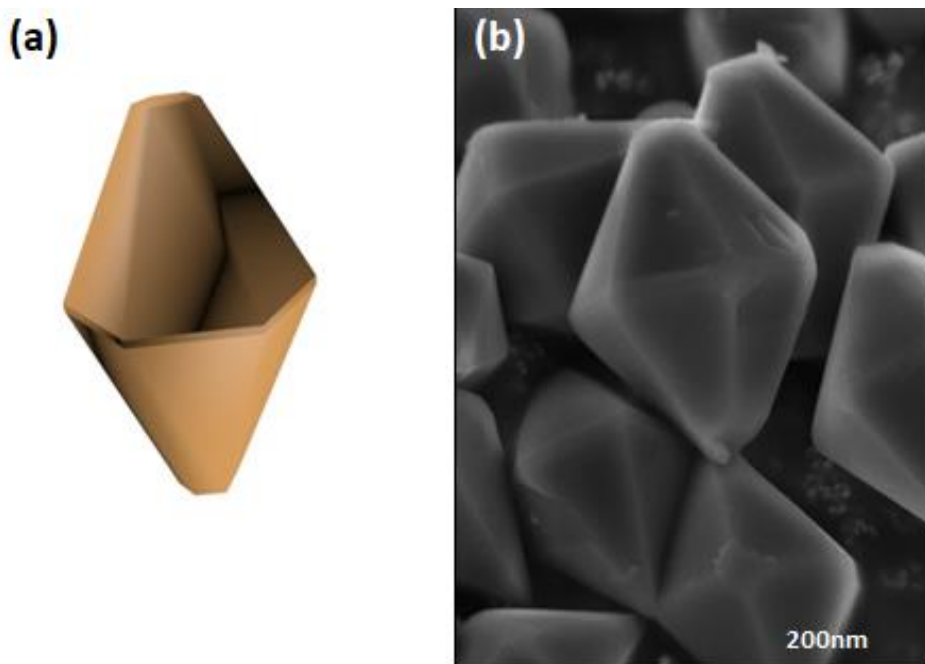
Figure 4-3 (a) Schematic diagram of Iron-based MOFs (MIL-88); (b) high magnification SEM image of Iron-based MOFs (MIL-88).

As discussed above, this section focuses on the study of the effects of changing the synthesis process of MIL-88 on the morphology of the material to optimize the procedure and obtain the typical morphology. Parameters such as process time, temperature, solvent type and concentration, and additives experimented, and the results are discussed in the following sections. The structural crystanality is as important as the morphology when synthesising this material and XRD test was

performed to confirm the structure obtained and chemical composition. **Figure 4.4** shows XRD pattern of MIL88 which is consistent with the results reported in the literature.
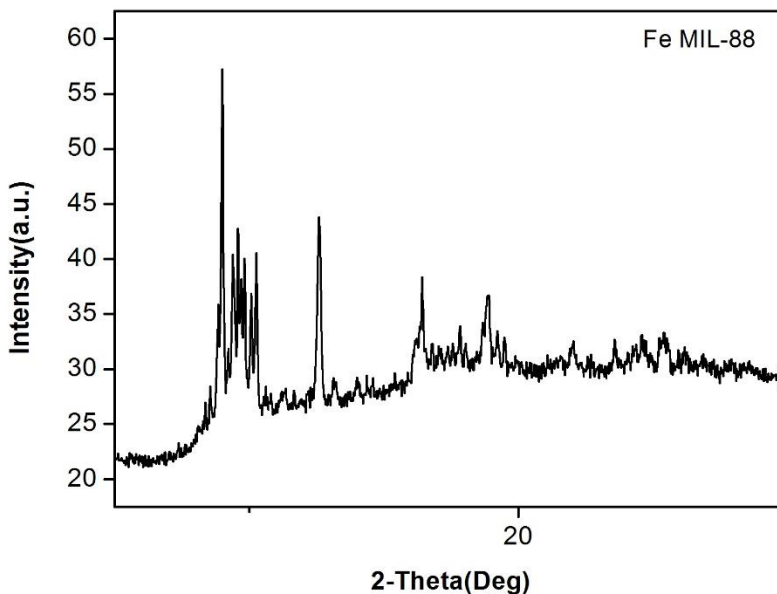
Figure 4-4 XRD pattern of MIL88 synthesized at 140°C for 20hrs.

4.3.2.1. Effect of different temperatures

During the hydrothermal process, the temperature is one of the key factors to control the structures of the final products. Herein, the hydrothermal temperature from 100-140 °C is investigated as the first parameter of the effects on the growth and morphologies of MIL-88. **Figure.4.5** shows the SEM images of MIL-88 synthesized for 20 hours at different temperatures. It can be seen from the SEM demonstration in **Figure 4.5** going from the top to the bottom pictures that with the increase of the process temperature, the complete crystallinity is observed, and entirely shaped MIL-88 is obtained. This conclusion coincides with previous studies in which is confirmed that the overall dimensionality of MOFs entirely develops with the increase of the reaction temperature[13].

As shown in **Figure 4.5 a and b**, the particles of as-synthesized MIL-88 at 100°C are still in the growth stage towards developing the final morphology. This can be observed form the different sizes of the microparticles as well as the shape of the small particles is not defined that might be

evidence of the continues structure evolution process. When the temperature was elevated to 120 ˚C, more defined particles of MIL-88 are obtained with relatively rough surface indicating the low crystalline structure **(see Figure 4.5 c and d).** MIL-88 particles obtained at 120 ˚C are uniformly distributed with similar particle size. Finally**,** as shown in **Figure 4.5 e and f** when 140 ˚C was applied during hydrothermal, the most uniform structure was delivered with the well-defined morphology of MIL-88 owing average particle size of 1.3μm representing the effect of temperature on the growth of MIL-88 on its morphology, particle size, surface and distribution and accord the studies have been done before. Thus, the optimized temperature for the hydrothermal process of the procedure of MIL-88 is 140 ˚C.
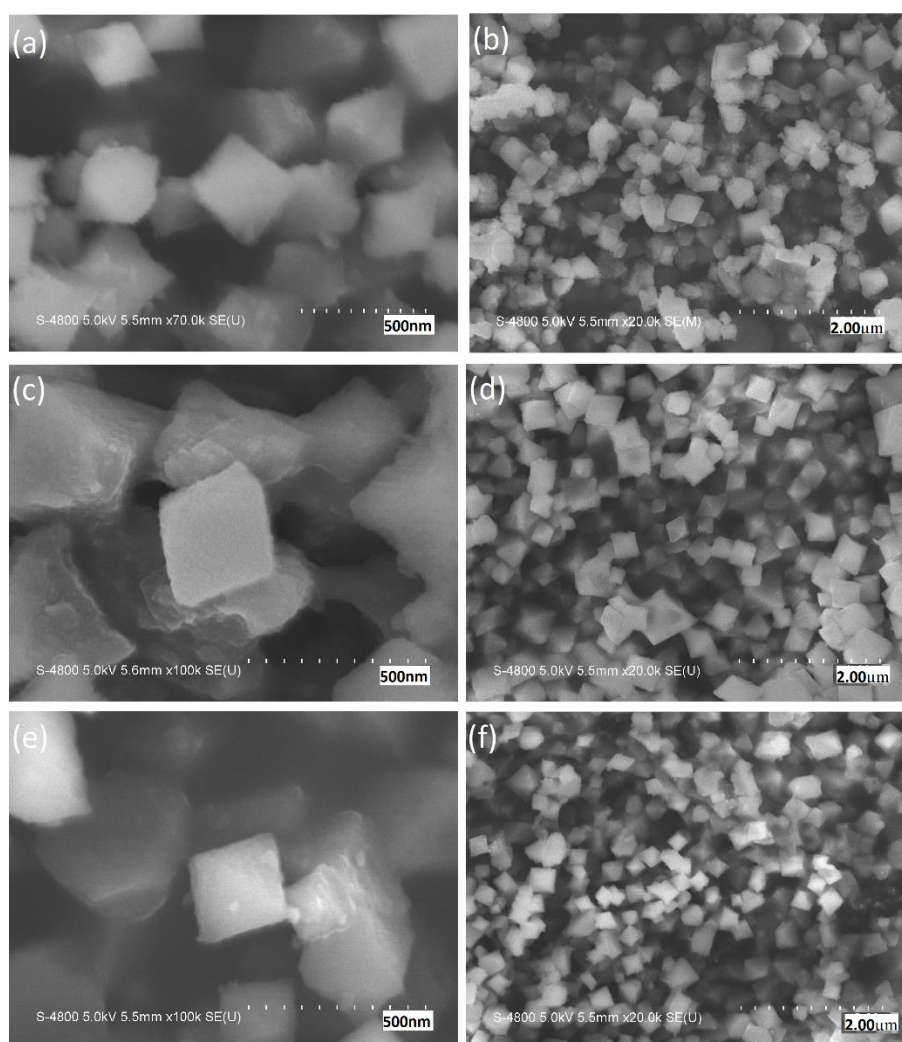
Figure 4-5 SEM of MIL-88 synthesized for 20 hours at different temperatures; (a) 100˚C; (b) 120˚C; (c) 140˚C.

4.3.2.2. Effect of different reaction times

Besides the hydrothermal temperatures, another critical parameter for the growth of MOFs structure and other materials is process time. The different samples with a different hydrothermal time of 6 h, 12 h, 20 h were synthesized at 120˚C with the same parameters used in the experiments sections. As shown in **Figure 4.6 a and b**, MIL-88 with 6 h has very rough surface and general morphology due to such short time for the different solvent to react and format the final product. However, with longer time of 12 h, the products show the improved structure features of MIL-88 with a large particle size of several microns and irregular surface **(see Figure 4.6 c and d)**. When the much longer time of 20 h was performed, the process exhibited the best reaction condition delivering the full growth of MIL-88 particle with uniform structure coherence, but the surface is relatively rough which could be related to the need of using surface modification additives (**see Figures 4.6 e and f)**.

To sum up, in this part, the hydrothermal time for the fabrication of MIL-88 has been optimized with 20 h. It is believed that the most extended process time is the best for full growth of MIL-88 where definite shape, uniform size, and distribution can be obtained. It is also found that the morphology and structure remains the same when process time exceed 16hrs indicating the optimization of the process time at 140˚C.
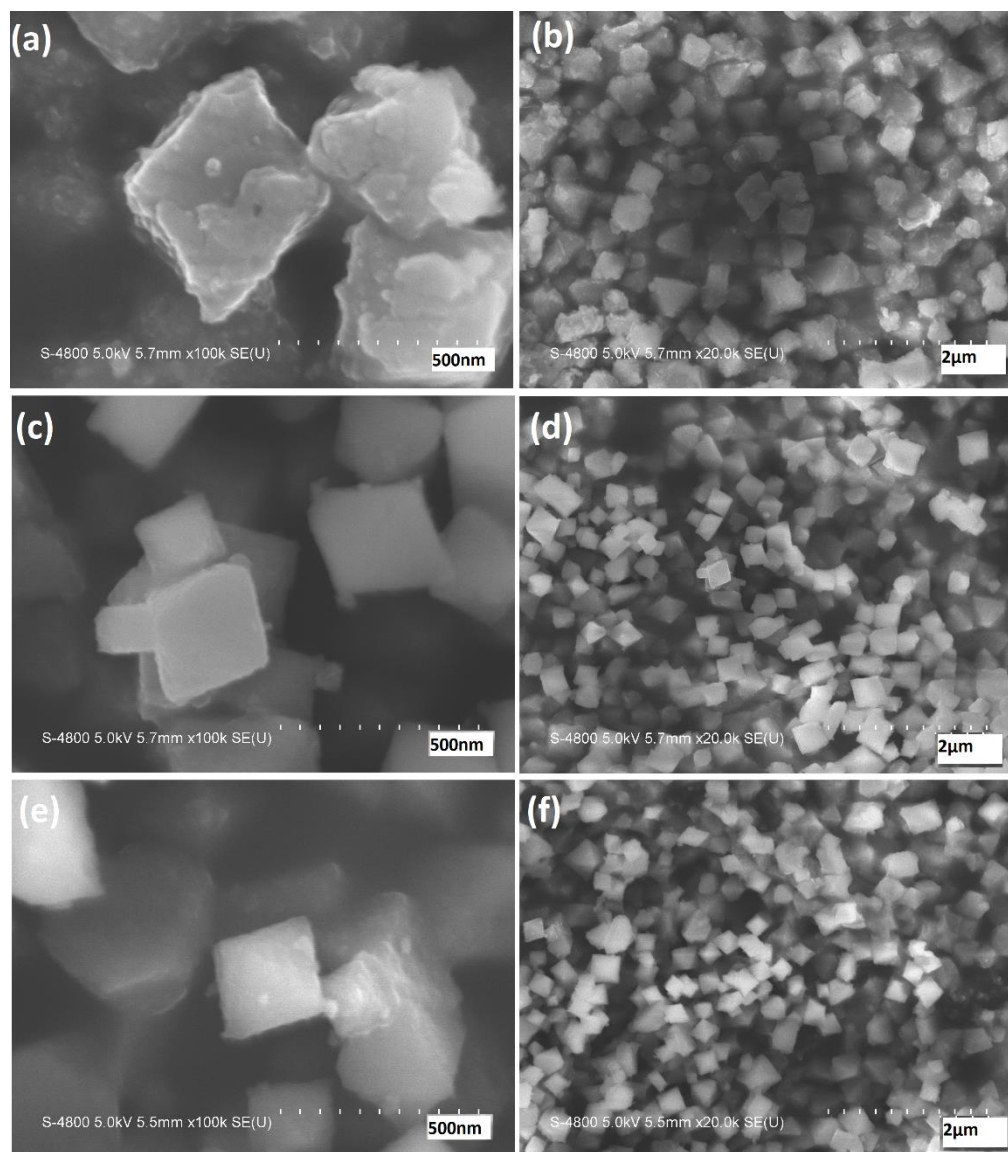
Figure 4-6 SEM images of MIL88 synthesized at 140C for (a&b) 6hours; (c&d) 12hours; (e&f) 20hours.

4.3.2.3. Effect of different solvent

In our first design, the solvent used in the process is high purity DMF. It is believed that the different solvent also has a noticeable influence on the morphologies of MIL-88. In this case, the different solvents have been applied in the hydrothermal process with the optimized parameters of the temperature of 140 °C and time of 20 h. In this part, another two solvents of ethanol of water are used as a comparison, in which the mixture of DMF and water used as for the first sample and the mixture of DFM, water, and ethanol used as the second samples. **Figure. 4.7** show the SEM images of the MIL88 synthesis at 140C for 20hrs in **(a, b)** DMF and water **(c, d)** DMF, water, and

ethanol. As seen from the SEM results, it is found that the two samples have different morphologies compared to the products using pure DMF solvent. As is shown in **Figure 4.7 a and b**, the first sample (using DMF and water as solvent) exhibits the aggregated particles with the uniform shapes indicating imperfect or unfinished growth process. Also, the SEM images of the second sample (using DMF, ethanol, and water as solvent) are shown in **Figure.4.7 (c, d)**. It is apparently seen that the morphologies are not homogenous which has some particles with the similar shape as the ideal MIL-88; on the other hand, it also has some particles with an entirely new form which interestingly is flower-like microparticles.

Therefore, it was found that using a different solvent such as water and ethanol entirely change the result and influence the morphology by delivering new structures and imperfection to the process. From this experiment, high purity DMF is believed to be the suitable solvent to synthesis MIL-88 with the targeted characteristics.
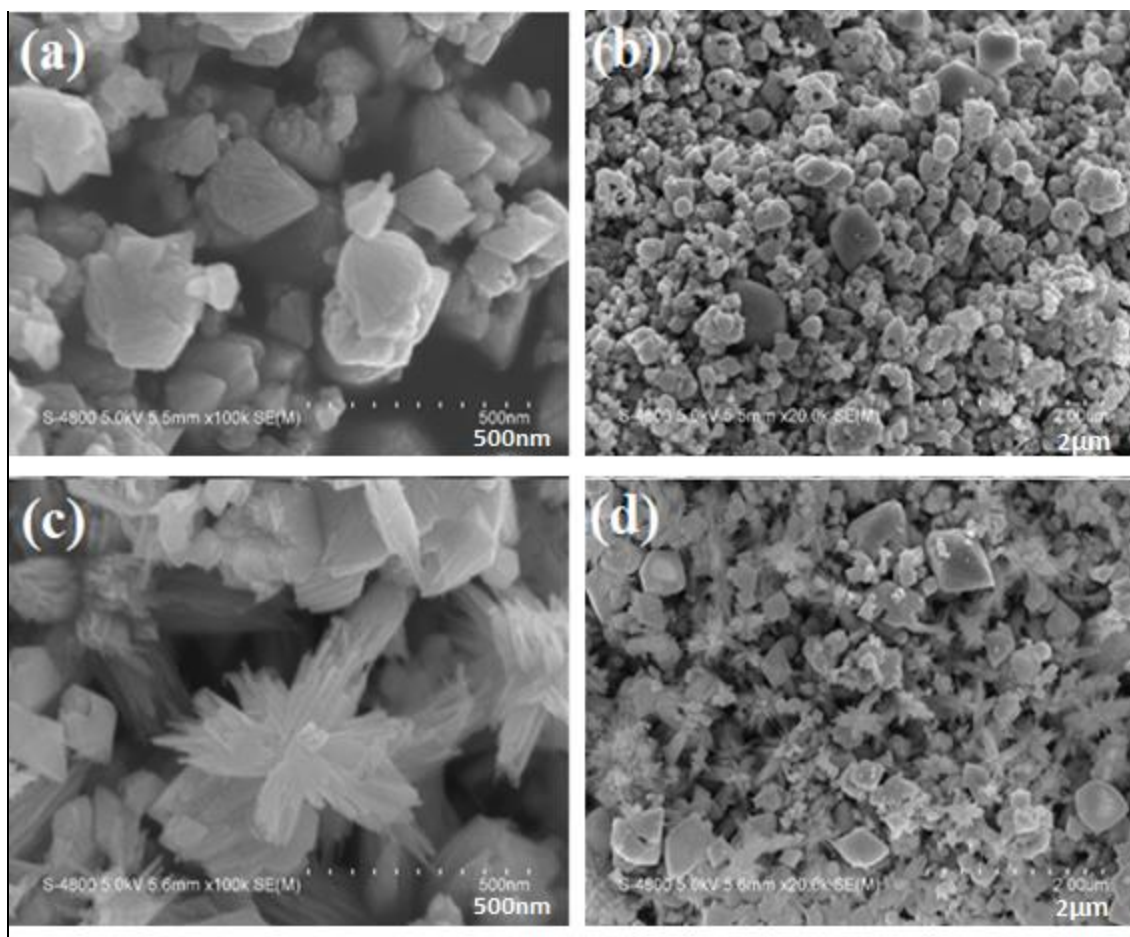
Figure 4.1-7 SEM images of MIL88 synthesis at 140C for 20hrs in (a, b) DMF and Water (c, d) DMF, Water, and Ethanol.

4.3.2.4. Effect of different weight concentration ratio of the precursor in the organic solvent

The concentration of the reactants is also an essential factor besides the temperature, time, and other parameters can be adjusted for the best results and directly affect the morphology, surface degree, and porosity of materials[1]. Based on this theory, the concentration of the reactants to the solvent of MIL-88 was changed, and the impact of this adjustment was investigated. 50% and 75% of reactants were used with the regular amount of the DMF solvent used before to synthesis MIL-88, and they were prepared at 140°C for 20hrs. When SEM tests were accomplished, it was found from the results that MIL-88 sample with less reactant concentration of 50% has full-grown microparticles with very soft surface and distinct structure as shown in **Figure 4.8 a and b.** nevertheless, MIL-88 with higher reactant concentration confirmed less uniform structure with a rough surface (**See Figure 4.8 c and d)**
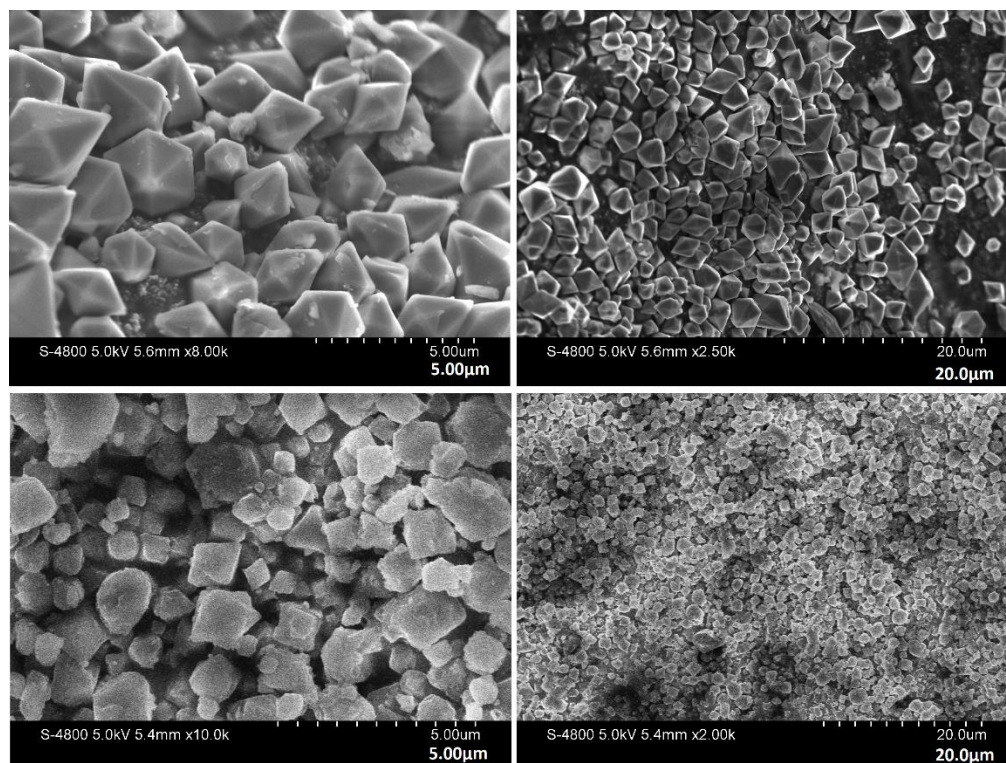
Figure 4-8 SEM images of different weight concentration ratio of the precursor in the organic solvent (a&b) 50% (c&d) 75% of the regular weight.

To conclude this part, reactant concentration is a significant parameter to optimize the synthesis process of MIL-88 which has a distinctly remarkable effect on the morphology of the MIL-88. However, studying other physical characteristics such as chemical composition using other techniques like XRD and Raman is vital to confirm the material composition after changing the reactants concentration.

4.3.2.5. Surfactant effect

Another effective strategy to control morphology and contain the synthesis process is using a surfactant that has effects on particle size and surface. In this part, one of the preferred surfactants of Pluronic F127 was used to control the structures and morphologies of MIL-88 further.

The sample with the addition of F127 exhibited excellent particle shape and uniform particle size. Also, particle size considerably dropped from few micrometers to few hundreds nanometer which apparently due to using F127 which agree with the reports where it is believed that F127 impact the particle size significantly. As shown in **Figure 4.9 a and b**, MIL-88 has very smooth surface and uniform particle size in a range of 800nm where it was synthesized at 140°C for 20hrs. PVP also was applied as an additive since it was reported in the literature that PVP could work as stabilizer and particle size controller, but the results showed no improvement on the MIL-88 morphology (see Figure 3.9 c and d). F127 can be easily removed by washing the sample with ethanol few times.

Hence, MIL-88 synthesized with the addition of F127 showed a very uniform structure with much smaller particle size and surface properties in comparison to MIL-88 prepared without any additive shown in **Figure 4.9 c and d**. The conclusion is drawn that the synthesis process of MIL-88 is optimized and could be controlled referring to our work and the influence of each factor is investigated for further applications.
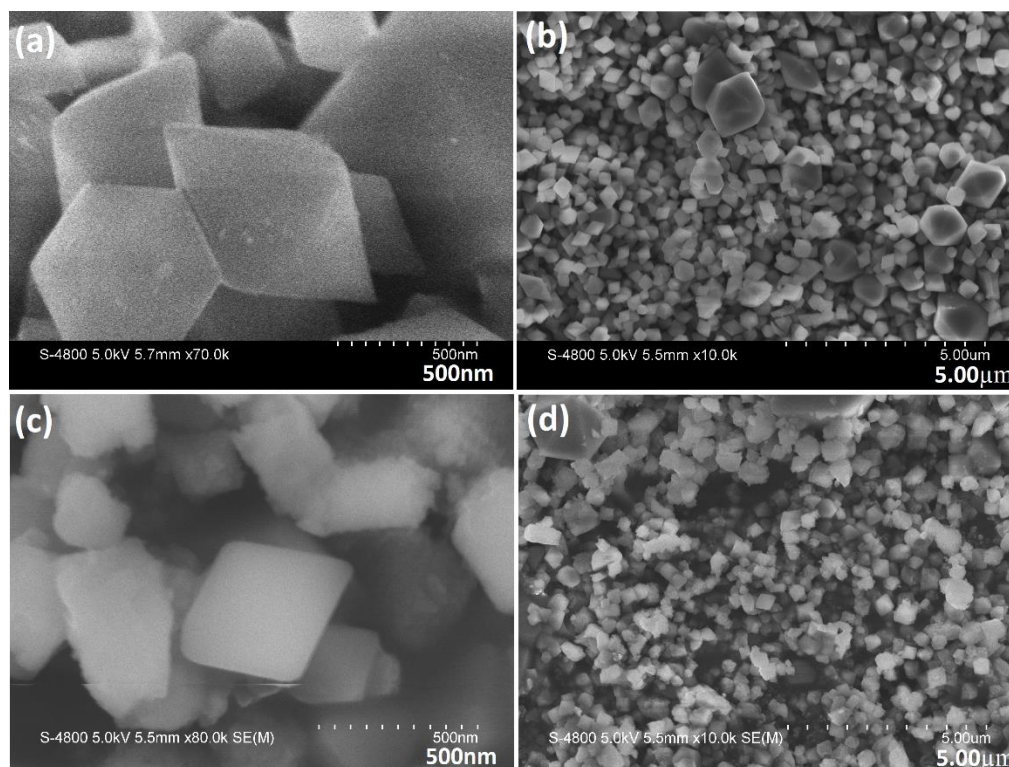
Figure 4-9 SEM images of MIL-88 synthesized at 140°C for 20hrs (a and b) with F127; (c and d) with PVP.

4.4. Summary and conclusion

This chapter mainly focuses on the synthetic procedure of preparing different types of MOFs including ZIF-8, ZIF-67, and MIL-88. The particular study was done on the optimization of the preparation method of MIL-88, and the effect of different parameters was investigated in details. For the ZIF-8, the preparation process was not changed from what has been reported in the literature. On the other hand, the ZIF-67 process was modified to obtain smaller particle size, and it was successfully achieved by using very simple rout we mentioned in the section 1.2.2. In details.

Finally, a comprehensive study was performed to understand the effect of different parameters such as time, temperature, reactant concentration, reaction medium, and additives on the morphology of MIL-88. It was found that the best condition to synthesis MIL-88 with very uniform structure, small particle size, and soft surface is performing the process at 140°C for 20hr, in DMF as a solvent and the addition of Pluronic F127 to control the particle size and stabilize the reaction. Further investigation is needed to study the chemical and thermal stability of the product for further applications which will be mentioned in chapter 5 as well.

References

1. Furukawa, H., et al., *The chemistry and applications of metal-organic frameworks*. Science, 2013. **341**(6149): p. 1230444.

2. Wu, D. and A. Navrotsky, *Thermodynamics of metal-organic frameworks*. Journal of Solid State Chemistry, 2015. **223**: p. 53-58.

3. Janosch Cravillon, S.M.n., † Sven-Jare Lohmeier,† Armin Feldhoff,‡ Klaus Huber,§ and Michael Wiebcke*,, *Rapid Room-Temperature Synthesis and Characterization of Nanocrystals of a Prototypical Zeolitic Imidazolate Framework*. Chemistry of Materials, 2009. **21(Issue8)**(08974756): p. 1410-1412.

4. Morozan, A. and F. Jaouen, *Metal organic frameworks for electrochemical applications*. Energy & Environmental Science, 2012. **5**(11): p. 9269.

5. Zhao, Y., et al., *Metal organic frameworks for energy storage and conversion*. Energy Storage Materials, 2016. **2**: p. 35-62.

6. Wang, L., et al., *Metal–organic frameworks for energy storage: Batteries and supercapacitors*. Coordination Chemistry Reviews, 2016. **307**: p. 361-381.

7. Xia, W., et al., *Metal–organic frameworks and their derived nanostructures for electrochemical energy storage and conversion*. Energy Environ. Sci., 2015. **8**(7): p. 1837-1866.

8. Wu, R., et al., *In-situ formation of hollow hybrids composed of cobalt sulfides embedded within porous carbon polyhedra/carbon nanotubes for high-performance lithium-ion batteries*. Adv Mater, 2015. **27**(19): p. 3038-44.

9. Li, M., et al., *Large-scale fabrication of porous carbon-decorated iron oxide microcuboids from Fe–MOF as high-performance anode materials for lithium-ion batteries*. RSC Adv., 2015. **5**(10): p. 7356-7362.

10. Yu, H., et al., *General Approach for MOF-Derived Porous Spinel AFe2O4 Hollow Structures and Their Superior Lithium Storage Properties*. ACS Appl Mater Interfaces, 2015. **7**(48): p. 26751-7.

11. McKinlay, A.C., et al., *Nitric Oxide Adsorption and Delivery in Flexible MIL-88(Fe) Metal–Organic Frameworks*. Chemistry of Materials, 2013. **25**(9): p. 1592-1599.

12. Wu, Y., H. Luo, and H. Wang, *Synthesis of iron(iii)-based metal–organic framework/graphene oxide composites with increased photocatalytic performance for dye degradation*. RSC Adv., 2014. **4**(76): p. 40435-40438.

13.   Sun, Y.-X. and W.-Y. Sun, *Influence of temperature on metal-organic frameworks.* Chinese Chemical Letters, 2014. **25**(6): p. 823-828.

14. Serre, C., et al., A route to the synthesis of trivalent transition-metal porous carboxylates with trimeric secondary building units. Angew Chem Int Ed Engl, 2004. 43(46): p. 6285-9.

15.   Yu, D., et al., Precisely tailoring ZIF-67 nanostructures from cobalt carbonate hydroxide nanowire arrays: toward high-performance battery-type electrodes. J. Mater. Chem. A, 2015. 3(32): p. 16688-16694.

Chapter 5

5. Carbon coated Cobalt Sulfides for LIBs and SIBs Anode Material

Abstract

In this chapter, Carbon coated cobalt sulfides derived from MOF (C@Co$_9$S$_8$) was synthesized via simple precipitation method, and the electrochemical performance of this material as an anode in sodium-ion and lithium-ion cells was investigated. Physical characterizations are carried out using scanning electron microscopy (SEM), Energy Dispersive X-ray Spectrometry (EDX), Raman spectroscopy, X-ray diffraction, Thermogravimetric Analysis, Structure characterization shows that the structure has high thermal stability, high surface area and high content of carbon. Electrochemical cyclic measurements indicate that this material has a high potential for batteries applications due to its stable performance and high reversible capacity for lithium and sodium storage.

Note: This chapter will be submitted as a paper by Ali Abdulla, Yang Zhao, Xueliang Sun; entitled: Carbon coated Cobalt Sulfides for LIBs and SIBs Anode material

5.1. Introduction

The development of advanced Lithium-ion battery has received significant attention for the last two decades due to the high energy density of lithium, high battery capacity which is successfully taken place for electric vehicle applications and portable devices[1, 2]. However, lithium abundance in the earth crust is alerting the fact that researchers have considered it which is going to rise the fabrication cost of this battery[3, 4]. Sodium ion battery is a promising alternative energy storage device that has been considerably studied because of the high sodium element availability on the earth, therefore low applicable cost of the element supply, low electrode fabrication cost and low redox potential[5, 6]. Sodium device is preferably considered for large-scale energy applications such as stationary power generation. Although sodium ion battery has the similar principle of work and mechanism of a lithium-ion battery, different challenges face the advancement of this battery due to the large size of sodium ion which is the primary factor for many issues such as low capacity and poor cycling. As it is known that sodium ion battery has not been commercialized yet and one of the difficulties that prevent this achievement is finding suitable host anode material for sodium ions because of the large ion size of sodium which is about 55% larger than lithium ion. In this regards, many research groups hardly work in this area, and some promising accomplishments have been conducted but challenges to find host material with high capacity and long cycling reversibility still need more effort. Using carbon nanostructures, metal oxides, and sulfides, and alloys for anode material have been reported in sodium storage[7].

Transitional metal sulfides have explicitly been studied due to their high theoretical capacity, sizeable gravimetric energy density, their volume change is less than that in metal oxides and also the product Na_2S is reversible in compare to other chemical product that results from the electrochemical reaction during charge/ discharge process[8]. For example, metal sulfides with layered structures such as MoS_2[9, 10] and SnSs[11] have been proven for anode materials in SIBs. It was suggested that such a layered structure could be used for SIBs anode due to the interlayers distance of about 0.615nm, which is almost twice the graphite interlayer space. Other metal sulfides have been studied such as iron sulfides[12], Tungsten sulfides[13], Zinc sulfides[14].

Mainly, cobalt sulfides (CoS, CoS_2, Co_3S_4, Co_9S_8, etc.) are among many metal sulfides that have attracted significant attention for their applications as an anode in LIBs and SIBs systems because of their chemical, physical and electrical properties. However, a material that contains such significant amount of sulfur has a very poor electrical conductivity which comes a challenging to obtain excellent rate capability. The second issue in this material is the volume change during cycling that leads to structural collapse and loss of the reaction reliability.

Many approaches have been studied to solve these problems such as using carbon materials as a matrix to improve the electrical conductivity, accommodate the volume extension and results to more structure and electrochemical performance reliability. For instance, Ko et al. fabricated a composite of Co_9S_8 nanoparticles and amorphous carbon and tested for SIBs anode where delivered high capacity of 404 mA h g^{-1} after 50 cycles. Wu and co-worker synthesized peapod-like carbon encapsulate cobalt chalcogenide nanowires (NWs) and investigated for SIBs' anode. Zhou et al. also reported the fabrication of a sandwich-like cobalt sulfides–reduced graphene oxide (CoS/rGO) composite using a hydrothermal method[15]. CoS/rGO was tested for SIBs anode and maintained a discharge capacity of 230 mA h g^{-1} after 100 cycles. Cobalt sulfides (CoS) nanoplates on reduced graphene oxide (CoS@rGO) was successfully synthesized via hydrothermal method by Peng et al.[16]. CoS@rGO was evaluated for SIBs anode performance and could retain the high specific capacity of 420 mAh g^{-1} at 1 A g^{-1} after 1000 cycles and extraordinary rate capability with a specific capacity of 306 mAh g^{-1} at a high current density of 10 A g^{-1}.

In LIBs, cobalt sulfides have been widely investigated for Anode materials and have shown high capability. For instance, CoS_2 is one of the most reported cobalt sulfides that has been reported in the literature for battery applications due to its high theoretical capacity of 871.21mAh g^{-1} and its significant electrical conductivity. Wang and co-workers investigated the electrochemical performance of LIBs anode made of Ultrasmall CoS_2 Nanoparticles within thin N-doped porous carbon shell, and fascinating results were conducted in their paper[17]. CoS_2 was synthesized using MOF template, and it exhibited a capacity of 560mAh g^{-1} after 50. Co_9S_8 synthesized using the hydrothermal method and supported on nickel foam and tested for battery performance[18]. Co_9S_8 delivered a capacity of 720mAhg^{-1} at a current density of 100mAg^{-1} over 100cycles. Many reports about cobalt sulfides have been published representing different techniques to solve the reduced cycling performance and rate capability of the electrodes[19, 20].

Here in, we successfully fabricated a cobalt sulfides $C@Co_9S_8$ derived from MOF template and coated with carbon. The products' characteristics are investigated to evaluate its physical and chemical properties and further tested as anode material in SIBs and LIBs where $C@Co_9S_8$ showed outstanding performance in comparison to pristine CoS and annealed Co_9S_8.

5.2. **Experimental section: Preparation of hollow mesoporousCo_9S_8**

5.2.1. Synthesis of ZIF-67 template

Cobalt nitrate (Co $(NO_3)_2$ ▪ $6H_2O$, 3.0066 g) and 2-methylimidazole (3.39365 g) were added at the same time to 500 ml of methanol. The entire reaction process was performed at 70 ℃ with agitated stirring. After stirring for 15-20 mins, the reaction was aged at room temperature without any interruption overnight. The resulting purple precipitate was centrifuged and washed several times with methanol before drying in an oven at 60 °C.

5.2.2. Synthesis of hollow mesoporous cobalt sulfides Co_9S_8

0.1 g of the as-prepared template was transferred into a round-bottomed flask containing 0.22g thioacetamide and 100 mL ethanol and 100 μL water. Then the mixture was refluxed for 1h under stirring. At last, the product was collected by centrifugation, washed with anhydrous ethanol and dried at 60 °C

5.2.3. Synthesis of Co_9S_8@Ar

the as prepared hollow mesoporous cobalt sulfide was transferred to calcination boat for post annealing process under Ar at 650˚C for 5hr.

5.2.4. Synthesis of carbon coated hollow mesoporous cobalt sulfides $C@Co_9S_8$

Co_9S_8 was treated at 650°C for 5h in $Ar/H_2/CH_4$, producing carbon coated hollow of mesoporous Co_9S_8.

5.3. Characterization

5.3.1. Physical Characterizations.

The morphology was studied using Hitachi S-4800 field-emission scanning electron microscope (SEM) operated at 10 kV. N_2 adsorption/desorption isotherms were obtained using a Folio Micromeritics TriStar II 3020 Surface Area and Pore Size Analyzer. The surface area of the product was calculated by the Brunauer, Emmett, and Teller (BET) model. Raman data were collected using a HORIBA Scientific LabRAM HR Raman spectrometer. For the X-ray diffraction (XRD) measurements, (Bruker, D8 Advance) was employed to characterize the structures of the prepared samples.

5.3.2. Electrochemical measurements

CR-2032 type coin cells were assembled in the argon-filled glove box. Li foil was used as the counter electrode and the reference electrode, a polypropylene separator (Celgard 2400), and as-prepared electrode as Anode. The electrolyte in LIBs was a solution of 1 M LiPF6 in a mixture

of ethylene carbonate (EC), dimethyl carbonate (DMC) and diethyl carbonate (DEC) (1: 1: 1, v/v/v). In SIBs the electrolyte consists of 1.0 m $NaCF_3 SO_3$ in diethylene glycol dimethyl ether (DEGDME). Each coin-cell we added 3-5 drops of electrolyte which are around 0.20 ml/cell. The Arbin BT-2000 Battery Tester was used to evaluate the electrochemical performance of the CR2032-type coin cells at room temperature. Charge/discharge tests were carried out on Arbin BT2000 with a voltage range of 0.0–3.0 V. Cyclic voltammetry (CV) experiments were studied using a Bio-logic multichannel potentiostat 3/Z (VMP3) with a scanning rate of 0.1 mV s^{-1} and at a potential range of 0.0–3.0 V (vs. Li^+/Li) in LIBs and (vs. Na^+/Na) in SIBs. Electrochemical impedance spectroscopy (EIS) tests were measured between the frequency range of 0.01 Hz to 100 kHz by versatile multichannel potentiostat 3/Z (VMP3).

5.4. Results and discussion

Carbon-coated cobalt sulfides MOF derived was prepared through a novel approach and further calcination process where all are shown in the schematic **Figure 5.1**. ZIF-67 as a sacrificial template to deliver Co_9S_8 was synthesized following reported method[21]. To obtain the final product, chemical vapor deposition setup was used to perform a simple calcination process for Co_9S_8 at 650°C for 5hr in $Ar/H_2/CH_4$ environment. The porous nanocages of $C@Co_9S_8$ formation could be referred to the Kirkendall effect reported in the references[22]. **Figure 5.2 a**. Shows the XRD results of which it can be confirmed that mesoporous $C@Co_9S_8$ and the $Co_9S_8@Ar$ peaks are corresponding to the high crystallinity of Co_9S_8 that could be indexed as cubic-phase Co_9S_8 (JCPDS Card, No. 65-1765), while the as prepared Co_xS_y XRD pattern has no peaks owing amorphous structure. Raman spectra were conducted to study the carbonization state of the material in Figure 2b. The ID/IG ratio in the Raman test was found to be low which might be attributed to higher percentage of graphitic carbon than non-graphitic (non-crystalline) carbon since it can be seen in the figure that the pristine cobalt sulfides have higher intensity graphitic D and G bands Raman peaks than the final product [23].
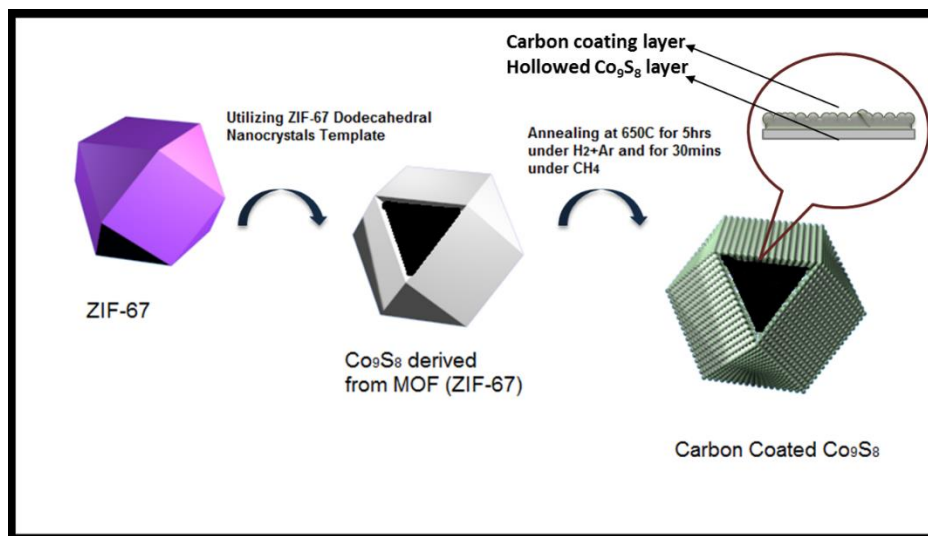
Figure 5-1 Schematic diagram of the synthesis of carbon-coated carbon sulfides.

The surface area and pore size of $C@Co_9S_8$, $Co_9S_8@Ar$, and pristine CoS were measured using the Brunauer–Emmett–Teller (BET) method. As it is shown in **Figure 5.2c,** BET surface area of $C@Co_9S_8$, $Co_9S_8@Ar$, and pristine CoS are 82.2347 m²/g, 42.1138 m²/g, 346.3035 m²/g; respectively. The highest surface area of the pristine cobalt sulfides is inherited from the MOF ZIF-67 template which is known for its high surface area that is also confirmed by the amorphous structure of CoS. The decrease of the surface area after the first annealing process could be attributed to the phase change after calcination process. BET surface area increased in in the $C@Co_9S_8$ which is ascribed to the collaboration of carbon coating in the structure. In **Figure 5.2d**. Pore size distribution also indicated that cobalt sulfides with carbon coating have the larger pore

volume of 0.175310 cm³/g while pristine CoS has a pore volume of 0.346955 cm³/g.
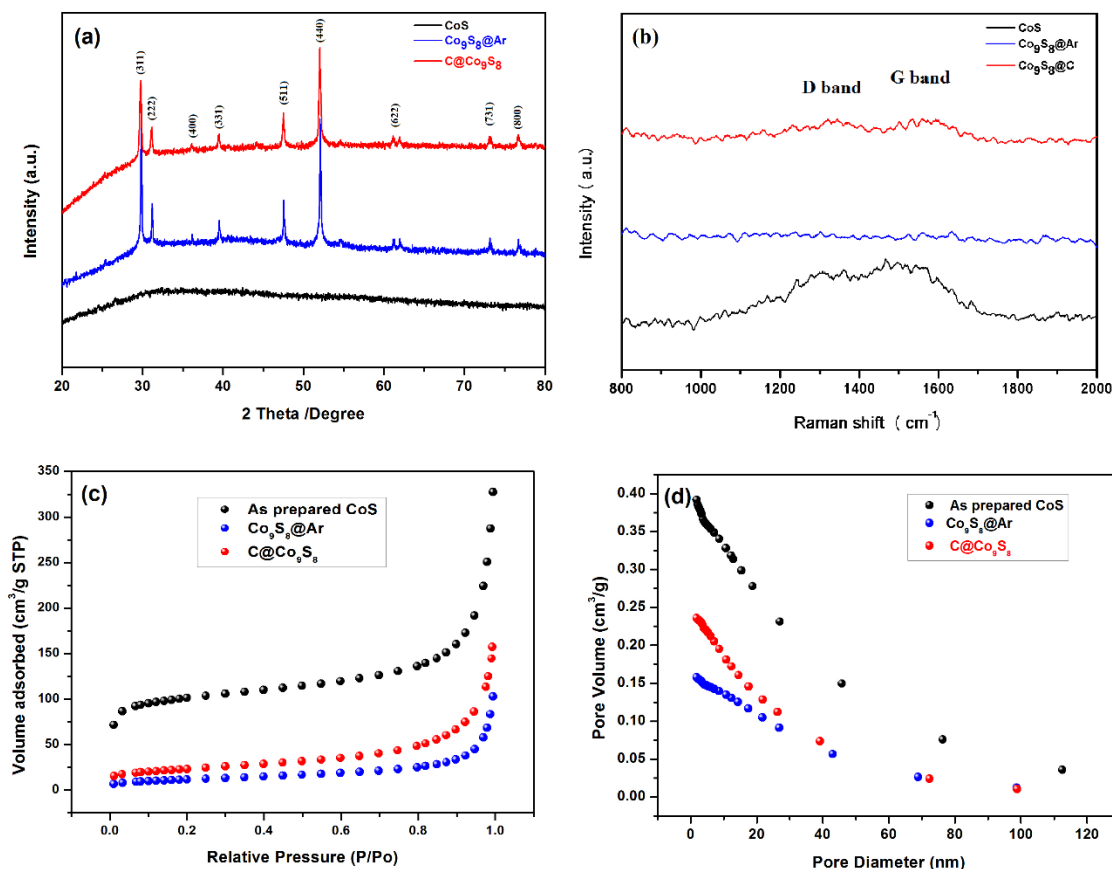
Figure 5-2 XRD pattern of the products C@ Co_9S_8, Co_9S_8@A , and Co_xS_y; (b) Raman spectrum; (c) Nitrogen gas adsorption-desorption isotherm and (d) pore size distribution of the Co_xS_y Co_9S_8@Ar.

The morphology of the materials starting from the ZIF-67 and ending up to the C@Co_9S_8 was carried out with SEM images. **Figure 5.3** a-f show that the structure remains the same as the template structure throughout the process except for when the utilization of Co_9S_8 which leads to creating holes in the nanoparticles and adds advantages to facilitating the lithiation process by increasing the electrolyte contact with the active materials. As shown in Figure 3a and b, high and low magnification SEM images of the as-prepared ZIF-67 with very uniform morphology owing polyhedral particle shape with an average size range between 100-200nm. In figure 3 c and d, it is evident that CoS retained the polyhedral morphology after the wet chemical process at 80˚C demonstrating excellent thermal stability. Interestingly, this structure has some holes in the particles due to Kirkendall effect which could attribute to easier lithium and sodium ions

penetration and more electrolyte accessibility to the active materials. The structure maintains its shape even after the calcination process as shown in Figure 3 e and f in which also the structure is very porous and consist of tiny particles connected with each other. From the EDS element mapping, uniform distribution of the elements can be observed indicating the successful material design and composition (**see Figure 5.3** g-j). All elements including C, O_2, Co, and S are homogeneously distributed within the material indicating well chemical composition.
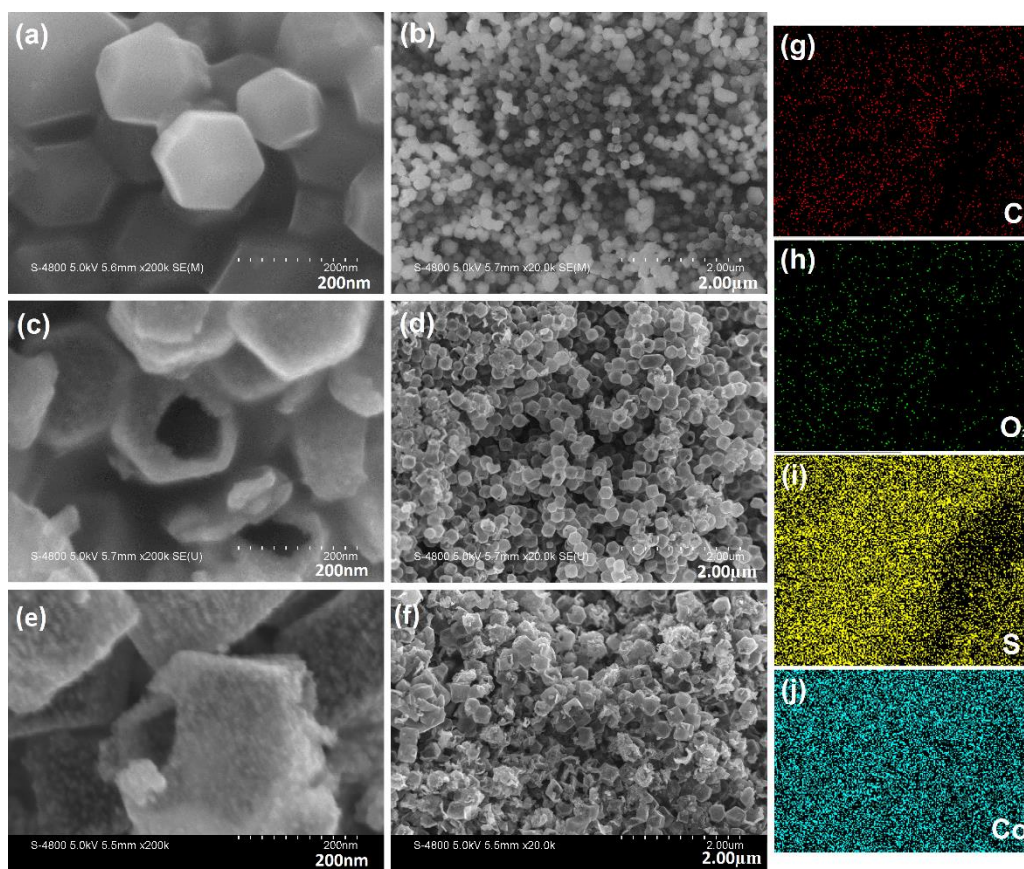
Figure 5-3 SEM images of (a-b) ZIF-67, (c-d) Co_xS_y, and (e-f) $C@Co_9S_8$, (g-j) EDS elemental mapping of the C@ Co_9S_8.

The electrochemical performance of the as-prepared cobalt sulfides (CoS, Co_9S_8, and $C@Co_9S_8$) was evaluated as anode material in SIBs and LIBs. **In a sodium ion cell**, **Figure 5.4 a**, shows the first 5 cycles of the cyclic voltammetry (CV) for $C@Co_9S_8$ with a scan rate of 0.1 mV s^{-1} in the potential range 0−3.0 V. The main cathodic peak at $\approx$ 0.6V is assigned to the electrochemical conversion reaction of $C@Co_9S_8$ which can be expressed by the following equation:

$$Co_9S_8 + 16Na^+ + 16e \leftrightarrow 9Co + 8Na_2S \qquad\qquad (1)$$
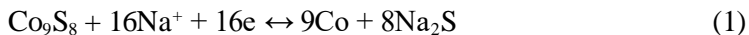
The main peak of the first discharge process consists of the reduction of the Co_9S_8 and the formation of the solid-electrolyte-interface (SEI) layers at the same time in which process the sodium starts to make their channels thro the Co_9S_8 structure at low potentials. after the first cycles, the main cathodic peak at 0.6V is positively shifted to 0.9V and overlapped in the last four cycles implying the repeated Na^+ insertion and extraction processes. Moreover, the electrochemical reaction during cycling can be further observed from the selected galvanostatic charge/discharge curves of the $C@Co_9S_8$ material at a current density of 0.1A g^{-1} shown in the **Figure 5.4b.** The discharge plateau at around 0.6V in the first cycles inconsistent with the CV peaks as well as the following cycles in which the reduction peaks is positively shifted to the higher potential of around 0.9V. The small cathodic peak at 0.65V started to constantly appear on the CV curve from the 2nd to the 5th cycles could be assigned to different phase reaction which contributes to more specific capacity.

Figure 5-4 **For sodium-ion battery** (a) CV curves of the $C@Co_9S_8$ at a scan rate of 0.1 mV s^{-1}; (b) Discharge and charge voltage profiles of the $C@Co_9S_8$; (c) Cycling performance of

the $Co_9S_8@Ar$ and $C@Co_9S_8$ electrodes cycled at a current density of 100 mA g^{-1}; (d) Rate capability performance of the C@ Co_9S_8 at various current densities.
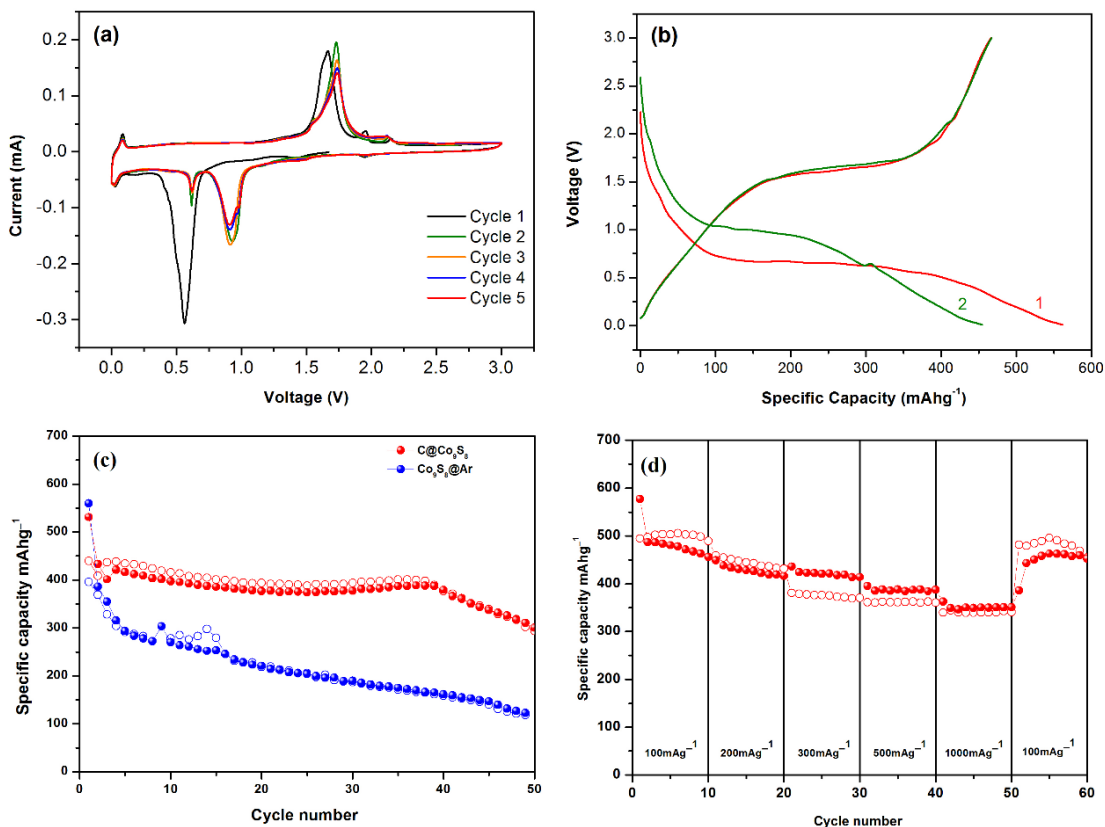
The cycling performance was further investigated for $C@Co_9S_8$, $Co_9S_8@Ar$, and pristine CoS in which $C@Co_9S_8$ shows a very stable cycling performance after the first cycle at a current density of 100 mA g^{-1}. $C@Co_9S_8$ maintained a discharge capacity of ≈ 400 mAh g^{-1} after 35 cycles whereas $Co_9S_8@Ar$ experienced a continues capacity fading after the first discharge capacity. The stable cycling of $C@Co_9S_8$ is contributed to the structural integrity which retains opened Na^+ ions pathways and guarantee and continues insertion and extraction for N^+ in the structure during cycling. also

Rate performance test was conducted to express the advantage of the carbon coating more. The product shows outstanding rate capability at different current densities. $C@Co_9S_8$ exhibited discharge capacities of 455.96, 416.21, 414.12, 387.54, and 351.14mAh g^{-1} at current densities of 100, 200, 300, 500, 1000 mA g^{-1}, respectively. Carbon coating and the unique structure of $C@Co_9S_8$ played a critical role in the reliable electrochemical performance utilizing three important properties; first, the hollow structure of the cobalt sulfides derived from MOF is very stable, and its high porosity facilitates the Na^+ insertion/extraction within the structure. Secondly, carbon coating improved the electrical conductivity of the cobalt sulfides that led to obtaining high rate capability. Finally, carbon coating also eliminates the negative impact of the volume extension by providing high flexibility and accommodating the strain caused by such phenomenon.

In the lithium-ion cell, the same three materials were electrochemically investigated as anode material in LIBs for comparison and showing the effectiveness of the carbon coated cobalt sulfides. The cyclic voltammetry (CV) for $C@Co_9S_8$ with a scan rate of 0.1 mV s^{-1} in the potential range 0−3.0 V is shown in **Figure 5.5a**. $C@Co_9S_8$ experienced two reduction peaks at 1.6V, and 1.0V in the first cycle is assigned to the formation of the SEI layer and the reduction of Co_9S_8 to Li_2S and Co metal; respectively. There was another reduction peak observed at 0.6V could be referred to the second phase of cobalt sulfides. In the charging process, one oxidation peak is observed at 2.1V assigned to the reformation of Co_9S_8 from reversible reaction of Co and Li_2S. These results are also consistent with the charge, and discharge curves of $C@Co_9S_8$ cycled at 100mA g^{-1}.
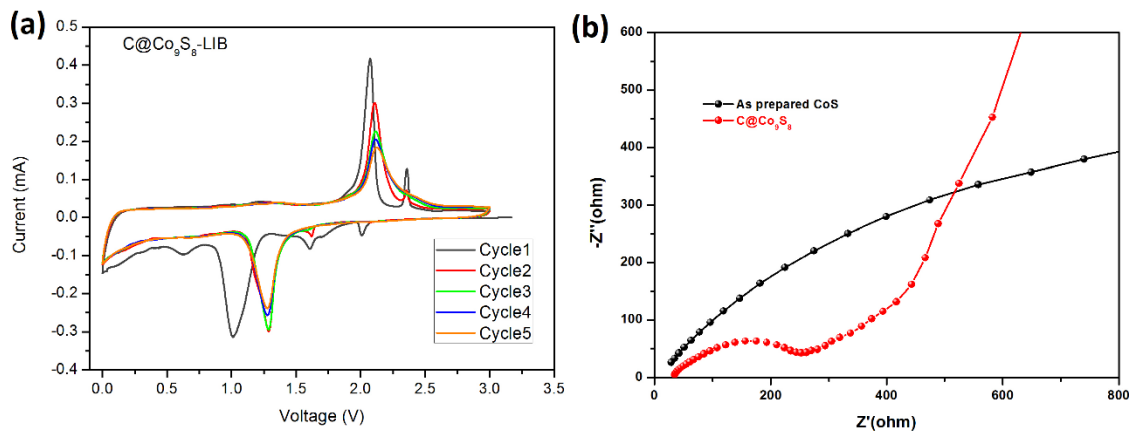
Figure 5-5 (a) CV curves of the C@Co$_9$S$_8$ at a scan rate of 0.1 mV s^{-1}; (b) Nyquist plots of C@ Co$_9$S$_8$ and Co$_x$S$_y$ after 100 cycles;

Moreover, To evaluate the electrochemical cycling, C@Co$_9$S$_8$, Co$_9$S$_8$@Ar, and pristine CoS were cycled at a current density of 0.1Ag^{-1} for 100 cycles and the significant improvement of cycling performance of C@Co$_9$S$_8$ can be noticed. C@Co$_9$S$_8$ retained a high discharge capacity of 693.37mAh g^{-1} after 100 cycles owing high electrochemical reversibility while a severe capacity fade happened for the Co$_9$S$_8$@Ar, and pristine CoS and low capacities of 176.35 and 108.39mAh g^{-1} were delivered after 100cycles as are shown in **Figure 5.6b**. Pristine CoS and Co$_9$S$_8$@Ar experienced a sharp capacity drop that is attributed to the particles aggregation after cycling due to the volume change and structural damage. It has been reported that metal sulfides suffer from poor rate performance due to the low electronic conductivity. Carbon coating is one of the active strategies that has been applied to overcome this challenge in which carbon coating can improve structure flexibility and help accommodating volume expansion effects as well as increases the material electric conductivity.

The enhancement of the electrochemical performance of C@Co$_9$S$_8$ due to the function of carbon coating is highlighted in the rate performance results at various current densities in **Figure 5.6c**. C@Co$_9$S$_8$ can deliver specific capacity of 649.99, 585.98, 551.48, 509.32, and 435.85mAh g^{-1} at current density of 100, 200, 300, 500, and 1000mA g^{-1}; respectively, while Co$_9$S$_8$@Ar exhibited a specific capacity of 243.79, 165.78, 133.59, 94.50, and 45.25mAh g^{-1} at current density of 100, 200, 300, 500, and 1000mA g^{-1}. The pristine CoS exhibited almost the near the same poor rate performance of Co$_9$S$_8$@Ar where the advantage of the carbon coating can be highlighted for comparison. Moreover, to investigate the rule of the carbon coating, long cycling performance of C@Co$_9$S$_8$ at high current densities was tested and shown in **Figure 5.6d** where it can be seen that

$C@Co_9S_8$ retained a specific capacity of 332.77 and 184.24mAh g^{-1} after 1000 cycles at a current density of 1 and 2A g^{-1}; respectively.
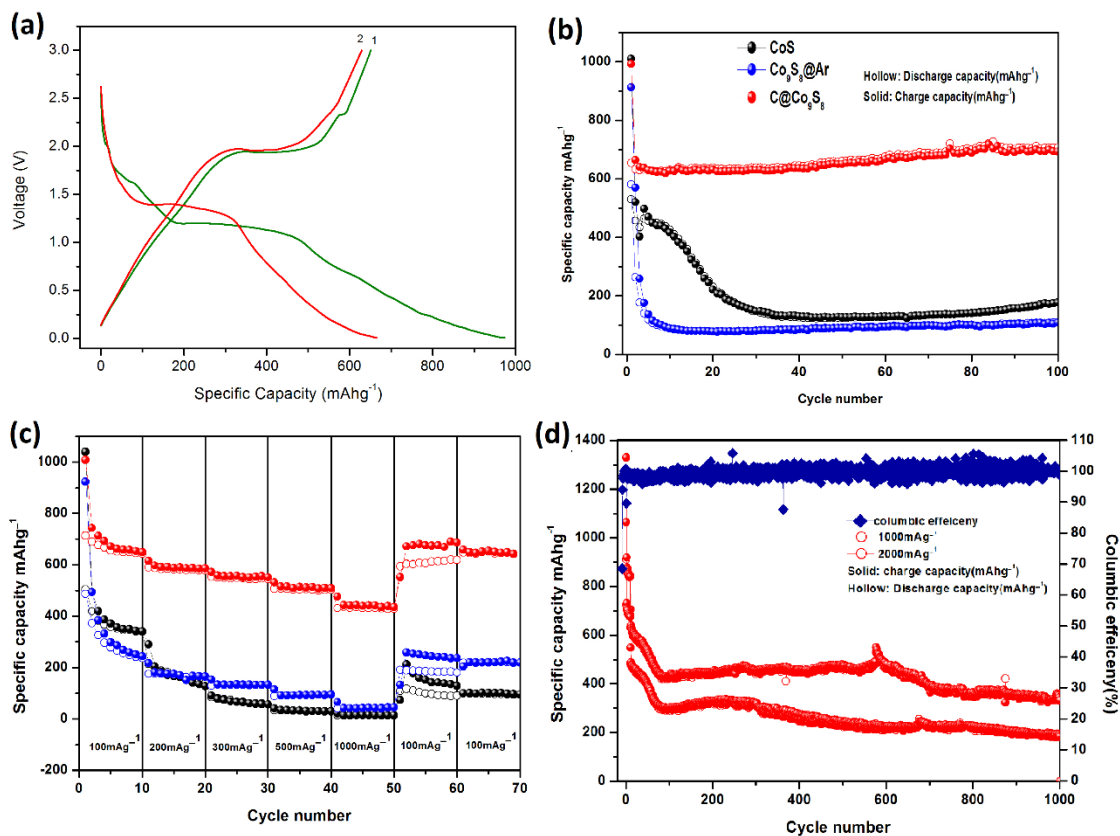
Figure 5-6**. For Lithium-ion battery;** (a) Discharge and charge voltage profiles of the $C@Co_9S_8$; (b) Cycling performance of the $Co_9S_8@Ar$ and $C@Co_9S_8$ electrodes cycled at a current density of 100 mA g^{-1}; (c) Rate capability performance of the C@ Co_9S_8 at various current densities. (d) Long cycling performance of $C@Co_9S_8$ at 1000mAg^{-1} and 2000mAg^{-1} for 1000 cycles;

5.5. Conclusion

In summary, MOF-derived Cobalt sulfides with carbon coating have been successfully synthesized using ZIF-8 as a template in one step reaction and subsequent calcination process. Benefiting from the porous structure and carbon coating, the product exhibited high capacity of 400 after 30cycles in sodium ion cell and as high discharge capacity as 693.37mAh g^{-1} after 100 cycles in the lithium-ion cell. Carbon coating is an effective strategy to resist the volume changes and keep its adverse effects at a minimum as well as improving the electrical conductivity which

can be observed from the high rate capability of the cobalt sulfides. In the future, another carbon matrix can be used to resolve the poor electrical conductivity and buffer the volume extension for the cobalt sulfides derived from MOF. Introducing MOF derived materials especially metal sulfides as anode material without any further treatment is still challenge and needs more investigation.

References

1. Larcher, D. and J.M. Tarascon, *Towards greener and more sustainable batteries for electrical energy storage.* Nature Chemistry, 2014. **7**(1): p. 19-29.

2. Chan, C.K., et al., *High-performance lithium battery anodes using silicon nanowires.* Nat Nanotechnol, 2008. **3**(1): p. 31-5.

3. Palomares, V., et al., *Na-ion batteries, recent advances and present challenges to become low cost energy storage systems.* Energy & Environmental Science, 2012. **5**(3): p. 5884.

4. Slater, M.D., et al., *Sodium-Ion Batteries.* Advanced Functional Materials, 2013. **23**(8): p. 947-958.

5. Nithya, C. and S. Gopukumar, *Sodium ion batteries: a newer electrochemical storage.* Wiley Interdisciplinary Reviews: Energy and Environment, 2015. **4**(3): p. 253-278.

6. Yabuuchi, N., et al., *Research development on sodium-ion batteries.* Chem Rev, 2014. **114**(23): p. 11636-82.

7. Kim, S.-W., et al., *Electrode Materials for Rechargeable Sodium-Ion Batteries: Potential Alternatives to Current Lithium-Ion Batteries.* Advanced Energy Materials, 2012. **2**(7): p. 710-721.

8. Bommier, C. and X. Ji, *Recent Development on Anodes for Na-Ion Batteries.* Israel Journal of Chemistry, 2015. **55**(5): p. 486-507.

9. Li, Y., et al., *Enhancing sodium-ion battery performance with interlayer-expanded MoS2–PEO nanocomposites.* Nano Energy, 2015. **15**: p. 453-461.

10. Xie, X., et al., *MoS2/Graphene Composite Anodes with Enhanced Performance for Sodium-Ion Batteries: The Role of the Two-Dimensional Heterointerface.* Advanced Functional Materials, 2015. **25**(9): p. 1393-1403.

11. Prikhodchenko, P.V., et al., *Nanocrystalline tin disulfide coating of reduced graphene oxide produced by the peroxostannate deposition route for sodium ion battery anodes.* Journal of Materials Chemistry A, 2014. **2**(22): p. 8431.

12.   Walter, M., T. Zund, and M.V. Kovalenko, *Pyrite (FeS2) nanocrystals as inexpensive high-performance lithium-ion cathode and sodium-ion anode materials.* Nanoscale, 2015. **7**(20): p. 9158-63.

13.   Liu, Y., et al., *WS2 Nanowires as a High-Performance Anode for Sodium-Ion Batteries.* Chemistry, 2015. **21**(33): p. 11878-84.

14.   Su, D., K. Kretschmer, and G. Wang, *Improved Electrochemical Performance of Na-Ion Batteries in Ether-Based Electrolytes: A Case Study of ZnS Nanospheres.* Advanced Energy Materials, 2015: p. 1-13.

15.   Zhou, Q., et al., *Sandwich-like cobalt sulfide–graphene composite – an anode material with an excellent electrochemical performance for sodium ion batteries.* RSC Adv., 2015. **5**(88): p. 71644-71651.

16.   Peng, S., et al., *Unique Cobalt Sulfide/Reduced Graphene Oxide Composite as an Anode for Sodium-Ion Batteries with Superior Rate Capability and Long Cycling Stability.* Small, 2016. **12**(10): p. 1359-68.

17.   Wang, Q., et al., *Facile Synthesis of Ultrasmall CoS2Nanoparticles within Thin N-Doped Porous Carbon Shell for High Performance Lithium-Ion Batteries.* Small, 2015. **11**(21): p. 2511-2517.

18.   Jin, R., et al., *Co 9 S 8 nanosheet arrays supported on nickel foam for enhanced performance as anode material for Li-ion batteries.* Materials Letters, 2016. **163**: p. 183-186.

19.   Qiu, B., X. Zhao, and D. Xia, *In situ synthesis of CoS2/RGO nanocomposites with enhanced electrode performance for lithium-ion batteries.* Journal of Alloys and Compounds, 2013. **579**: p. 372-376.

20.   Huang, Z.X., et al., *Synthesis of self-assembled cobalt sulphide coated carbon nanotube and its superior electrochemical performance as anodes for Li-ion batteries.* Electrochimica Acta, 2015. **167**: p. 388-395.

21.   Jiang, Z., et al., *Synthesis of novel ZnS nanocages utilizing ZIF-8 polyhedral template.* Chem Commun (Camb), 2012. **48**(30): p. 3620-2.

22.   Hu, L. and Q. Chen, *Hollow/porous nanostructures derived from nanoscale metal-organic frameworks towards high performance anodes for lithium-ion batteries.* Nanoscale, 2014. **6**(3): p. 1236-57.

23.   Nomso Hintsho, A.S., Hilary Masenda, Deena Naidoo, Dave Billing, Paul Franklyn, and a.S. Durbach, *Direct synthesis of carbon nanofibers from South African coal fly ash.* Nanoscale Research Letters, 2014. **9**(387).

Chapter 6

6. Metal sulfides derived from MOFs: synthesis, characterization, electrochemical performances

Abstract

Metal sulfides have been intensively studied in different applications due to their availability, different unique structures including 2-dimensional and 3-dimensional structures, and their ability to form folded structures. They have been used in many applications and energy storage is one of the hottest areas of the study of this class of materials. ZnS, SnS_2, and Fe_xS_y are synthesized via calcination process using CVD method using MOFs as templates. The morphology and structures were characterized by scanning electron microscopy (SEM), X-ray diffraction (XRD) and thermogravimetric analysis (TGA). Electrochemical performances were studied by cyclic voltammograms (CV) and cycling performance and rate capability for lithium ion and sodium ion batteries. In this chapter, ZnS showed high performance as robust candidate anode in LIBs and SIBs by delivering high capacities and long cycling stability.

6.1. Introduction

As discussed in the introduction, transition metal sulfides (TMSs) such as ZnS, SnS_2, FeS_2 have been in favor to use for energy storage and conversion due to their high energy density, high theoretical capacity, and affordability. However, metal sulfides suffer from irreversible capacity fading after the first cycle that caused by several reasons such as the phase change during the electrochemical process and the volume change. In addition, low electric conductivity is a challenge that renders their applications in LIBs and SIBs and affects their cycling performance. Volume change in metal sulfides could reach up to 250% in some metals which damage the structure and block the charging ions from penetrating into the material besides that fact that active material de-attach from the current collector in the electrode leading to permanent loss of the capacity. Particularly, nanomaterials and their composites derived from MOFs have attracted increasing attention as electrodes for LIBs and SIBs due to the physical and chemical properties.

Zinc sulfides are one of metal sulfides candidates that have been investigated for batteries applications due to its high theoretical capacity, affordability, natural abundance and environmentally friendly nature. There are not many reports about ZnS for sodium ion batteries though meaning more research is required in this area to explore more about its potential. Among other metal sulfides, Fe_xS_y is widely reported material for batteries and other applications. F_xS_y is a cheap material that is available in a tremendous amount in the crust beside that fact that this material is very friendly to the environment.

In this chapter, different MOFs including ZIF-8, Sn-MOFs and MIL-88 are used as a template to synthesize different metal sulfides (ZnS, SnS_x, and FeS_x) with unique structures and properties. Furthermore, the as-prepared metal sulfides are tested as anode materials for both LIBs and SIBs.

6.2. Experimental procedures

6.2.1. Zinc sulfides derived from ZIF-8

ZIF-8 is used as templates for the following experiment, in which the synthesis process of ZIF-8 has been shown in Chapter.3. Two different approaches have been used to prepare ZnS, one is CVD method, and another one is a wet chemical method. For the CVD method, Zinc sulfides were synthesized by mixing the as prepared ZIF8 with sulfur powder with a weight ratio of 1:1 and moved into calcination boat. The mixture was heated up to 155°C for 5 hrs in the presence of Ar gas. For the wet chemical method, 0.1 g of the ZIF-8 was transferred into a round-bottomed flask

containing 0.22g thioacetamide and 100 mL ethanol and 100 µL water. Then the mixture was refluxed for 1 h under stirring. At last, the product was collected by centrifugation, washed with anhydrous ethanol and dried at 60 °C.

6.2.2. Tin sulfides derived from Sn-MOFs

Our previous study has reported the synthesis of Sn-based MOFs. In a typical hydrothermal process, 0.8 mmol of $SnCl_2$ and 1.6 mmol of 1,3,5 Benzenetricarboxylic acid were dissolved in 4.2 ml water, 4.2 ml DMF, 4.2 ml ethanol. The solution was transferred to Teflon stainless steel reactor for hydrothermal reaction at 100°C for 12hrs. For the preparing of tin sulfides, Following the previous method to synthesize ZnS by calcination process, Sn-MOF was mixed with sulfur powder with a weight ratio of 1:2. The mixed powder was moved to calcination boat and transferred to the oven to perform annealing process at 155°C for 5hrs, and then the temperature was elevated to 500°C for another 5hrs before the sample was cooled down to room temperature.

6.2.3. Iron sulfides derived from MIL-88

Fe_xS_y is synthesized via annealing process of the as-prepared MIL-88 using simple CVD method. 1g of MIL-88 was synthesized using a weight ratio of 1:2.5 and heated up to 155°C which is the sulfur evaporation temperature. The MIL-88 and sulfur powder were put in separate boats to make the sulfur flow above the MIL-88 which showed useful results better than mixing the two materials in the same boat. By flowing the sulfur over the MIL-88, sulfur reaction was assured after the evaporation of sulfur at 155°C

6.3. Results and discussion

6.3.1. Zinc sulfides derived from ZIF-8
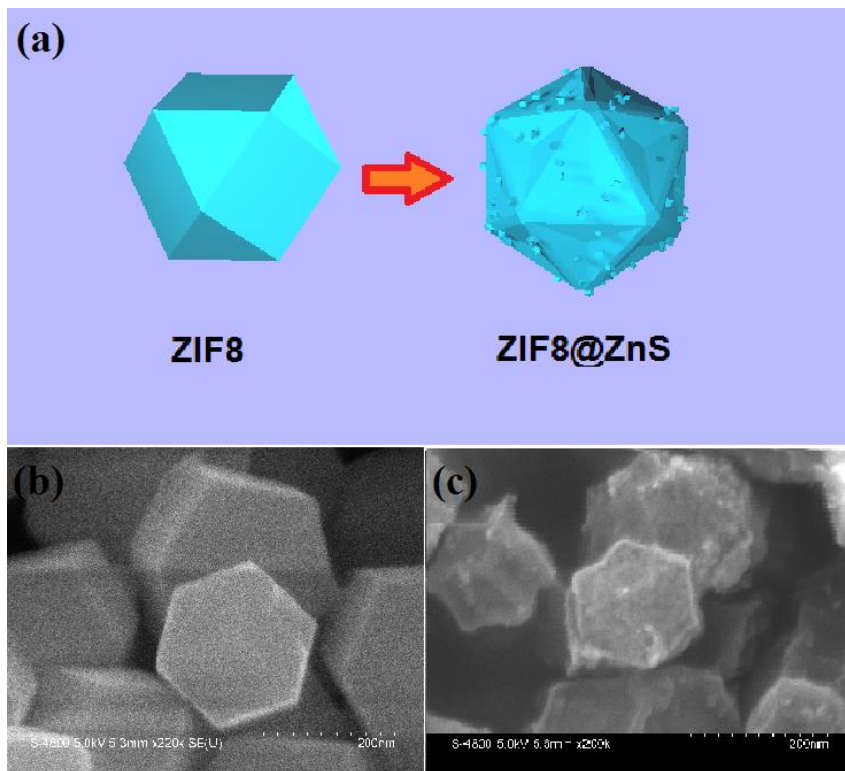
Figure 6-1 (a) Schematic of the synthesis process of ZnS derived from ZIF-8; SEM images of (b) ZIF-8; (c) ZnS.

Two ZnS samples were prepared using different chemical routes, ZnS prepared via calcination process is marked as ZnS-1, and the other sample was prepared through the wet chemical approach is named ZnS-2. The schematic diagram the fabrication process of ZnS derived from ZIF-8 are presented in **Figure. 6.1** (a). During the CVD process, ZnS-1 maintained the same shape of ZIF-8 with some shrinkage in the sides, and small particles were padded on the surface. **Figure 6.1b** and c show the SEM images of ZIF-8 and ZnS-1 derived from ZIF-8 via the annealing process. It shows that the morphology of ZIF-8 with a range of particle size between 200 and 250 nm and very uniform structure. SEM image in **Figure 6.2c** and d shows the ZnS-1 derived from ZIF-8 with the same particle size indicating the thermal stability of the product.
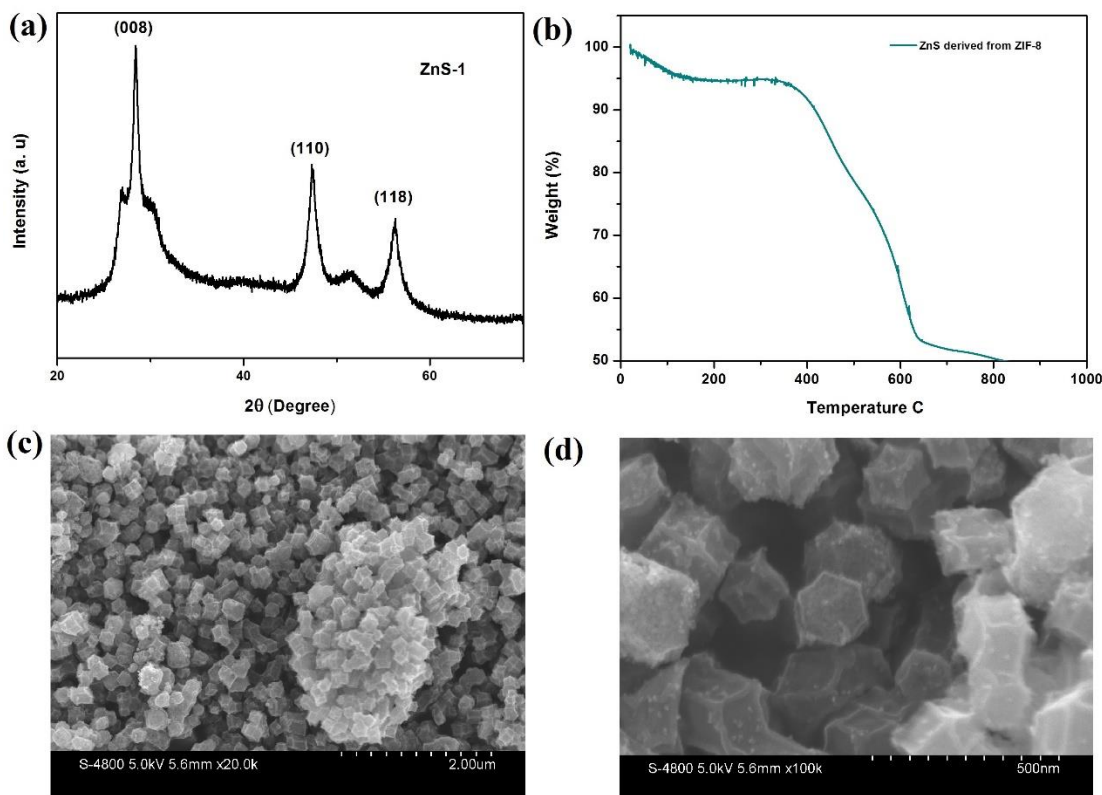
Figure 6-2 (a) XRD pattern of ZnS-1 derived from ZIF-8; (b) TGA test of ZnS-1 derived from ZIF-8. SEM images of ZnS-1 (c) low magnification; (d) high magnification.

XRD test was performed to confirm the structure and chemical composition in which the results were indexed to ZnS-1 (JCPDS card No. 00-039-1363). As shown in **Figure 6.2 a,** the three main diffraction beaks that appear in the XRD pattern $2\Theta = 28.58°$, $47.7°$ and $56.5°$ are well matched to the (008), (110) and (118); respectively, of the cubic structured ZnS-1 crystal face. All peaks are broad indicating that the ZnS-1 nanoparticles comprise of tiny nanoparticles. Thermogravimetric analysis TGA was carried out at a heating rate of $10°C$ min^{-1} from room temperature to $900°C$ in the air. As shown in TGA profile in **Figure 6.2 b**, the slight weight loss under $200°C$ is attributed to the evaporation of the absorbed water. Then, there is about 40% weight loss between $400°C$ and $600°C$ which is ascribed to the burnout of carbon in the material [7]. TGA profile represents the carbon mount within the structure which is very important to know since

carbon is the essential matrix for supporting electrodes materials by improving the electric conductivity and accommodate volume change by improving the overall structure strain.
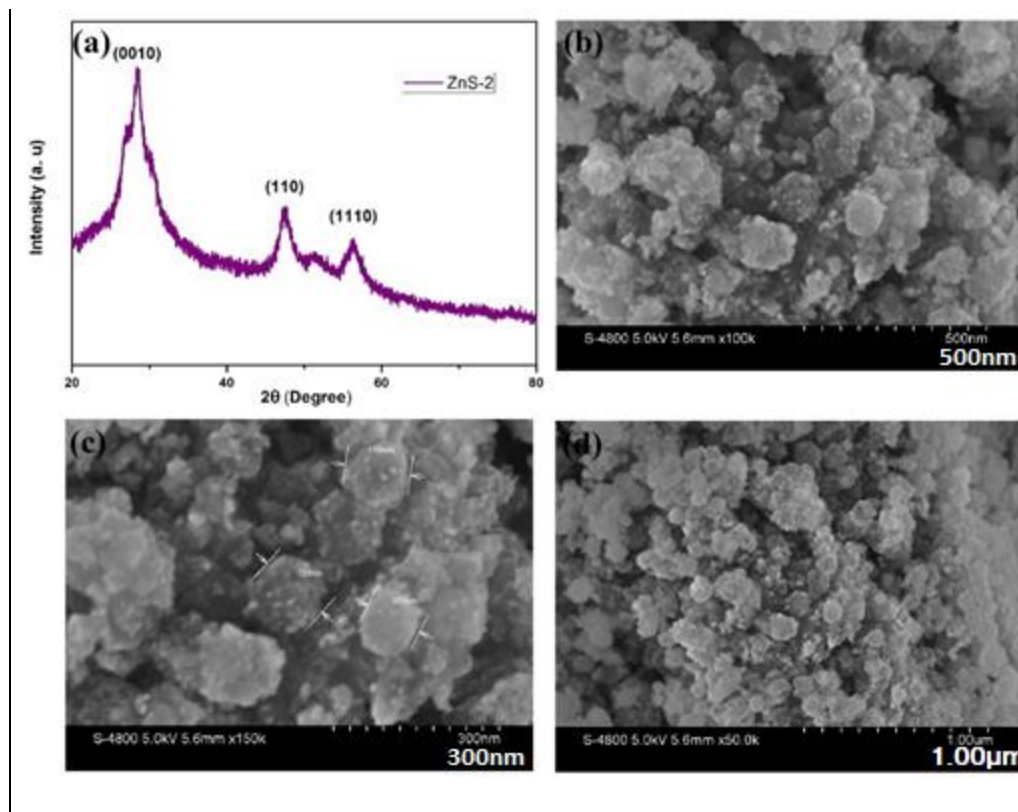
Figure 6-3 **(A)** SEM images of ZnS-1 with different magnification (b, c) high; (b) low.

For comparison, another ZnS-2 sample was prepared using the wet chemical method to investigate the possibility of obtaining the same morphology of ZIF-8 and better electrochemical properties. ZnS-2 was synthesized by transferring 0.1 g of the as-prepared ZIF-8 into a round-bottomed flask containing 0.22 g thioacetamide and 100 mL ethanol and 100 µL water; then, the mixture was refluxed for 1h under stirring. At last, the product was collected by centrifugation, washed with anhydrous ethanol and dried at 60°C. As shown in **Figure 6.3a** XRD test was conducted out to assure the successful design of ZnS-2. All the main peaks were well indexed to the PDF No. 00-012-0677, and the main peaks at $2\Theta = 28.58°$, $47.72°$, and $56.55°$ were matched to (0010), (110), (1110) planes; respectively. SEM was used to take images of ZnS-2 morphology and confirm the structure. As shown in **Figure 6.3 b, c, and d**, High and low magnification SEM images of the ZnS-2 were taken, and the morphology of the obtained ZnS-2 is nanosphere particles consist of small nanoparticles. It is different from the morphology was expected which is the ZIF-

8 dodecahedral indicating chemical instability when using this synthesis method to prepare ZnS-2. XRD pattern was carried out confirming the cubic ZnS-2 structure indicating the successful synthesis of ZnS-2.

To sum up, synthesizing ZnS-1 using calcination process shows high thermal and structure stability by delivering similar morphology to the ZIF-8 template was used. Structure and chemical composition were confirmed by SEM imaging and XRD testing; however, when the wet chemical route is used to prepare the ZnS-2, different morphology was obtained indicating a deficiency of structure instability although XRD results successfully confirmed the same composite.

The electrochemical properties of the ZnS-1 and ZnS-2 anodes were investigated in a 2032 type Coin half-cells with Li metal as the counter electrode in LIBs and Na metal as the counter electrode in SIBs as mentioned in chapter 2. Both cells were cycled and tested on the Arbin BT-2000 battery test station, and the working electrodes were prepared by mixing the weight ratio of 70:20:10 a ZnS as electrode's active material, carbon black as a conductive additive, and binder in Dimethylformamide as a slurry solvent.

The electrochemical performance of lithium-ion storage based on the ZnS-1 was first evaluated by cyclic voltammograms (CV) and cycling performance shown in Figure 5.4 a and b. As shown in **Figure 6.4 a,** in the first CV cycle, the broad cathodic peak at 1.4 V could be assigned to the reduction of ZnS-1 to the metallic Zn and then the formation of Zn-Li. This peak attributed to the irreversible formation of the solid electrolyte interphase (SEI) layer generated on the electrode and decomposition of the electrolyte which contributes to the capacity drop in the first three cycles. The Subsequent the cathodic CV cycles were consistent with the first cycle indicating an excellent stability during cycles. In the anodic scan, there is one distinct oxidation peak at 0.6 V which could be ascribed to the oxidation of Zn. The faintness of the peaks in the following cycles indicates an irreversible capacity fading which could be attributed to the structural instability and irreversible phase change during lithiation and delithiation process.

The cycling performances of ZnS-1 and ZnS-2 materials are investigated in the lithium-ion battery as anodes. Both electrodes were cycled at a current density 100 mA g^{-1} for 100 cycles in the voltage range of (0.01-3)V. As shown in **Figure 6.4 b**, ZnS-1 exhibited initial discharge capacity of 991.8 mAh g^{-1} whereas ZnS-2 initial discharge capacity was as high as 1036 mAh g^{-1}. However, both electrodes suffered from sharp capacity fading during 5 cycles before it starts to stabilize. The specific capacity of the ZnS-1 dropped by about 65% in the second cycle which is attributed to the decomposition of the electrolyte to form the solid electrolyte interphase (SEI).

After 100 cycles, ZnS-1 still can deliver a specific capacity as high as 280 mAh g^{-1} with a columbic efficiency of 98.6% demonstrating very high cycling stability. This stable performance attribute to the high structural integrity of ZnS-1 with high surface area and porosity that facilitate Li$^+$ insertion and desertion as well as the presence of carbon within the material that enhance the electric conductivity and accommodate the volume expansion. However, ZnS-2 experienced as capacity fade by 62% after the first cycle which maintained a specific capacity of 145.2 mAh g^{-1} after 100 cycles. Also, ZnS-2 has very stable cycling after the first 20 cycles which shows the structure reliability and high charging and discharging reversibility. It was found that ZnS-1 can perform better lithium storage than ZnS-2 which could refer to better structure design and integrity of ZnS-1; yet, there is more space for performance improvement since the first reversible capacity of ZnS-1 is 644.57 mAh g^{-1} which is higher than the theoretical capacity of ZnS (theoretical capacity 550 mAh g^{-1}). After 100 cycles the capacity retained is about 43% of the first reversible capacity. This capacity decreasing could be attributed to an irreversible phase change of ZnS-1 to other phases in addition to the large surface area of ZnS-1 which could contribute to more contact between the electrode material and the electrolyte. Hence, more side reactions could perform with the phase change that results finally to irreversible capacity fading.

Figure 6-4 (a) Cyclic voltammetry curve at 0.1mV S^{-1} scan rate of ZnS-1 in LIBs half-cell; (b) Cycling performance of ZnS-1 and ZnS-2 at a current density of 100mA g^{-1}.

The two samples were also tested as an anode in sodium ion battery for electrochemical evaluation. Cyclic voltammograms (CV) ZnS-1 was firstly recorded in half-cell sodium-ion battery at a potential range of (0.01-3.0)V. As shown in **Figure 6.5a**, in the first cathodic cycle, one broad peak appears at 0.9V, which is assigned to first sodiation process and the formation of solid

electrolyte interphase (SEI) layer due to the decomposition of electrolyte; however, the intensity of this peak decreased in the subsequent cycles indicating a conversion reaction between sodium and ZnS-1 which is alloying reaction[12]. In the anodic cycling, several, one main anodic peak is observed at 0.1V in the first cycle which could be contributed to the first sodium desertion reaction. This sharp peak shifted to a higher voltage at 0.25V in the following cycles signifying high discharge reversibility.

To further verify the cycling performance of the ZnS-1 and ZnS-2 electrodes in for sodium storage, both were cycled for 70 cycles at 100 mAh g^{-1} in voltage rate 0-3V, as depicted in **Figure 6.5b**. ZnS-1 exhibited superior performance which delivered a first discharge capacity of 590mAh g^{-1} and maintained a capacity of 202mAh g^{-1} after 60 cycles. The capacity dropped after the first cycles that could be referred to the formation of the solid electrolyte interphase (SEI) layer and the decomposition of the electrolyte. On the other hand, ZnS-2 delivered only a discharge capacity of 24.77mAh g^{-1} after 60 cycles indicating a large capacity lost after the first discharge capacity of 358mAh g^{-1}. The better performance of ZnS in compare to ZnS-2 could be attributed to the stable structure was obtained for ZnS-1 using the calcination process. Also, ZnS-1 shows proper sodium intake indicating the ability to accommodate such large ion size with less volume expansion effect which is a prevalent issue for metal sulfides. The presence of high percentage of carbon in the structure improves the mechanical strength of the structure as well elevate the electrical conductivity since it has been a challenge for sulfides materials due to the low conductivity of sulfur.
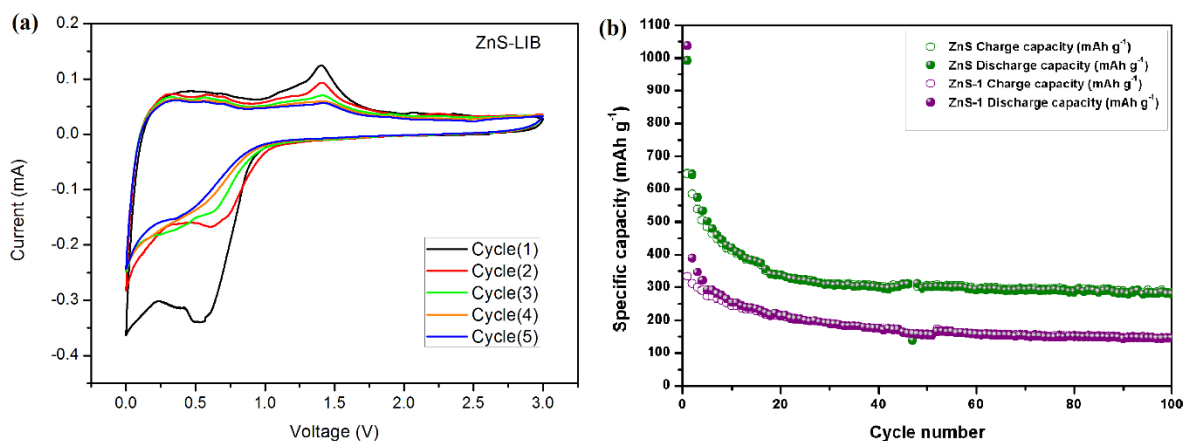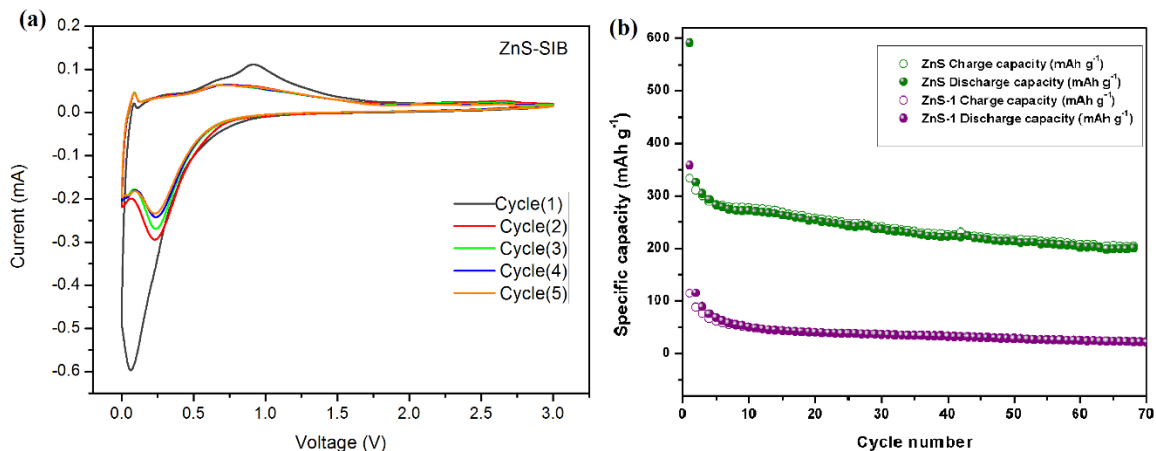
Figure 6-5 (a) Cyclic voltammetry curve at 0.1mV S^{-1} scan rate of ZnS-1 in SIBs half-cell; (b) Cycling performance of ZnS-1 and ZnS-2 at a current density of 100mA g^{-1}.

All in all, in this section, synthesis process of ZnS-1 derived form ZIF-8 was successfully performed, and proper characterization techniques were used to confirm the obtained material. In addition, the electrochemical performance of ZnS-1 prepared through calcination process, and ZnS-2 prepared via wet chemical process was carried out for comparison. ZnS-1 showed superior performance in lithium ion and sodium ion storage owing more stable structure, higher reversible capacity and excellent cycling stability.

6.3.2. Tin sulfides derived from Sn-based MOFs

Tin sulfides amongst many metal sulfides that have drawn high attention in energy storage field due to their excellent electrochemical properties. As the focus of our study is metal sulfides derived material, SnS-MOFs derived is also synthesized and studies in this section. Morphology of Sn-MOFs was demonstrated by the SEM technique showing a unique pyramidal structure with a very soft surface and uniform particles distribution. As shown in Figure 6.6 a and b, high and low-resolution SEM images of Sn-MOF are obtained from our previous study representing the morphology and shape features. EDX elemental mapping was performed to study the chemical composition, and as shown in Figures 6.6 c, d and e that Sn-MOFs obtained a balanced combination of carbon, Oxygen, and Tin elements.
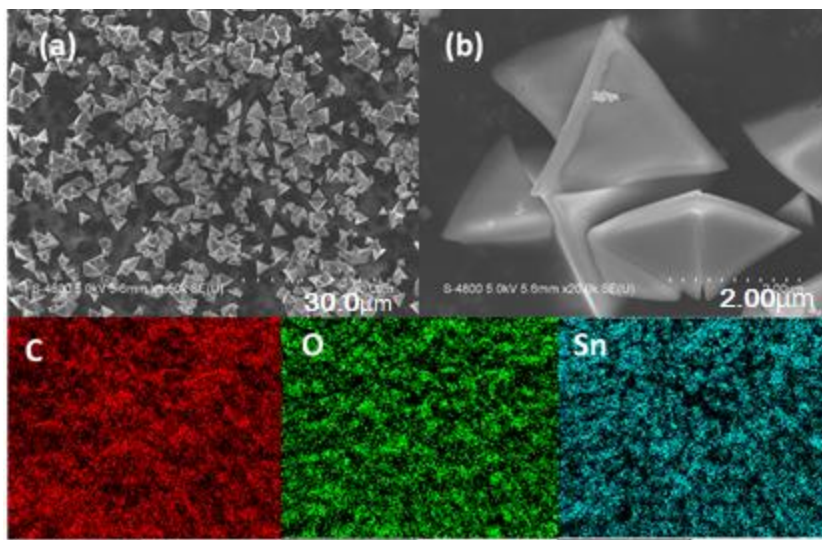
Figure 6-6 SEM images and EDX mapping for Sn-MOFs

XRD pattern was obtained to confirm the successful preparation of Sn-MOFs (see Figure in Supporting information). SEM observation was performed to confirm the morphology of the obtained material. As shown in **Figure 6.7a,** XRD patterns for SnS was investigated to confirm the chemical composition and the structure. It was found that the obtained SnS own impure phase that was indexed to the PDF file (No 01-083-0047). The main peaks at $2\Theta = 30.07°$, $31.08°$, $31.15°$, $31.53°$, and $32°$ were assigned to the crystal planes (004), (200), (020), (113), and (201) respectively. **Figure 6.7**b shows the SnS was obtained after the calcination process which successfully the structure displayed high thermal stability by keeping the same structure.

Figure 6-7 XRD pattern of SnS_2 derived from MOF; (b) SEM image of SnS_2

Electrochemical performance of the as-prepared SnS is investigated as an anode in lithium ion and sodium ion batteries. LIBs and SIBs were tested at th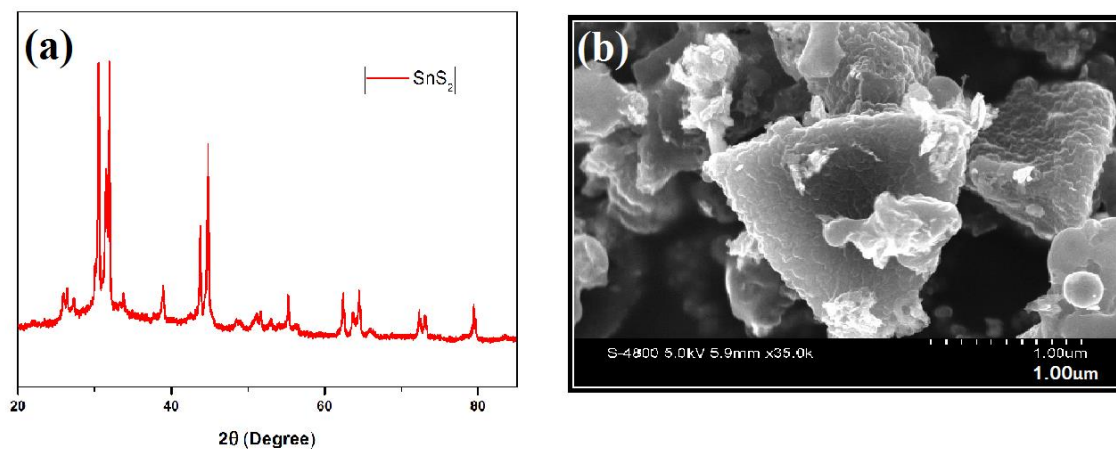e same condition under a current density of 100mA g^{-1} in the voltage range of 0-3V for 100cycles. For SnS electrode in LIBs, as shown in **Figure 6.8** a high initial discharge capacity of 978mAh g^{-1} which is attributed to the first insertion of Li^+ into the SnS structure and the decomposition of the electrolyte that leads to the formation of solid electrolyte interphase (SEI) layer. However, the capacity started to fade suddenly after the first cycle representing irreversible capacity lost which might be due to different reasons such as phase change during cycles that led to other side reactions and because of which some active materials could not contribute to the capacity anymore. Another valid reason is that volume change is severe that led to aggregation of materials. It also changed the structure and blocked Li^+ diffusion paths, so Li^+ cannot travel back in the reversible cycle as well as the active material could de-attached from the current collector after structure damage due to volume change and result in irreversible capacity fading. Moreover, SnS exhibited an initial reversible capacity as high as 716 mAh g^{-1} showing very high potential for this material in batteries applications. More research is needed for this experiment to solve this capacity fading and achieve a better electrochemical capability. First of all, investigate the structure reliability of this material after cycling, and maybe some XRD or other characterization studies could be used after cycling to have better insight into the problem. Another direction is by measuring the electrical conductivity of the material which is very important for stable cycling, and this could be worked using some surface coating techniques or carbon compositions[15]. Finally, study the structures' thermal stability more and see how to maintain the best out of the Sn-MOF properties of high surface area and porosity and obtained SnS_2 pure phase without any impurities
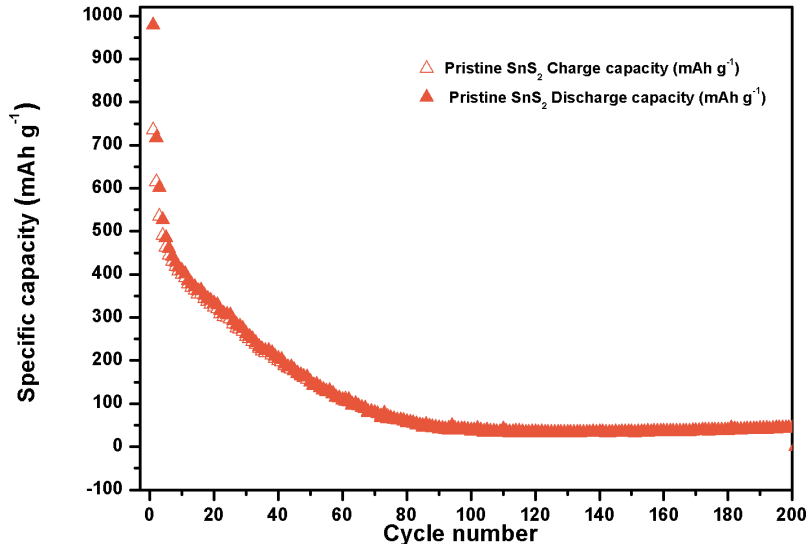
Figure 6-8 Cycling performance of SnS in LIBs half-cell at a current density of 100mA g^{-1}

SnS was also cycled in half-cell SIBs anode at a current density of 100 mA g^{-1} between 0-3V. SnS delivered an initial discharge capacity of 552mAh g^{-1} in the very first cycles indicating successful Na$^+$ insertion and SIE formation after the electrolyte decomposition. However, the capacity decreased in the first reversible cycle to 358mAh g^{-1}, and the battery died after only 6 cycles demonstrating irreversible charging and discharging process. It is believed that the same issue during lithium storage which could be the phase change of SnS leads to side reactions and lose of reversible capacity especially when Na$^+$ is the moving ions since Na$^+$ are much larger than Li$^+$ and much complicated to be hosted.

In conclusion, this part needs more effort to optimise the electrochemical characteristics of SnS$_2$ derived form MOF. What is worth to mention here is that SnS@MOF has not been reported in the literature in batteries applications and it should receive more attention because of the unique properties of this material and the high potential to be applied in energy storage devices. Intensive characterization study is required to better understand the limits of this material and its competency for different applications.

6.3.3. Iron sulfides derived from MIL-88

Fe_xS_y was successfully synthesized through calcination process was explained in details in the experimental section, and characterization techniques were used to confirm the process with the XRD pattern and SEM observation. **Figure 6.9a** shows a schematic illustration of the morphology of MIL-88 before the calcination process and then on the right side is the Fe_xS_y was obtained which has the same frame of the MIL-88. However, it appears to consist of plates or sheets stocked together in a row to form the bigger particle. As shown in **Figure 6,9b**, high magnification SEM observation of MIL-88 before the calcination process which is what demonstrated before in chapter 3. **Figure 6.9c** displays high magnification SEM image of the final product of Fe_xS_y after the annealing process at the mention condition.
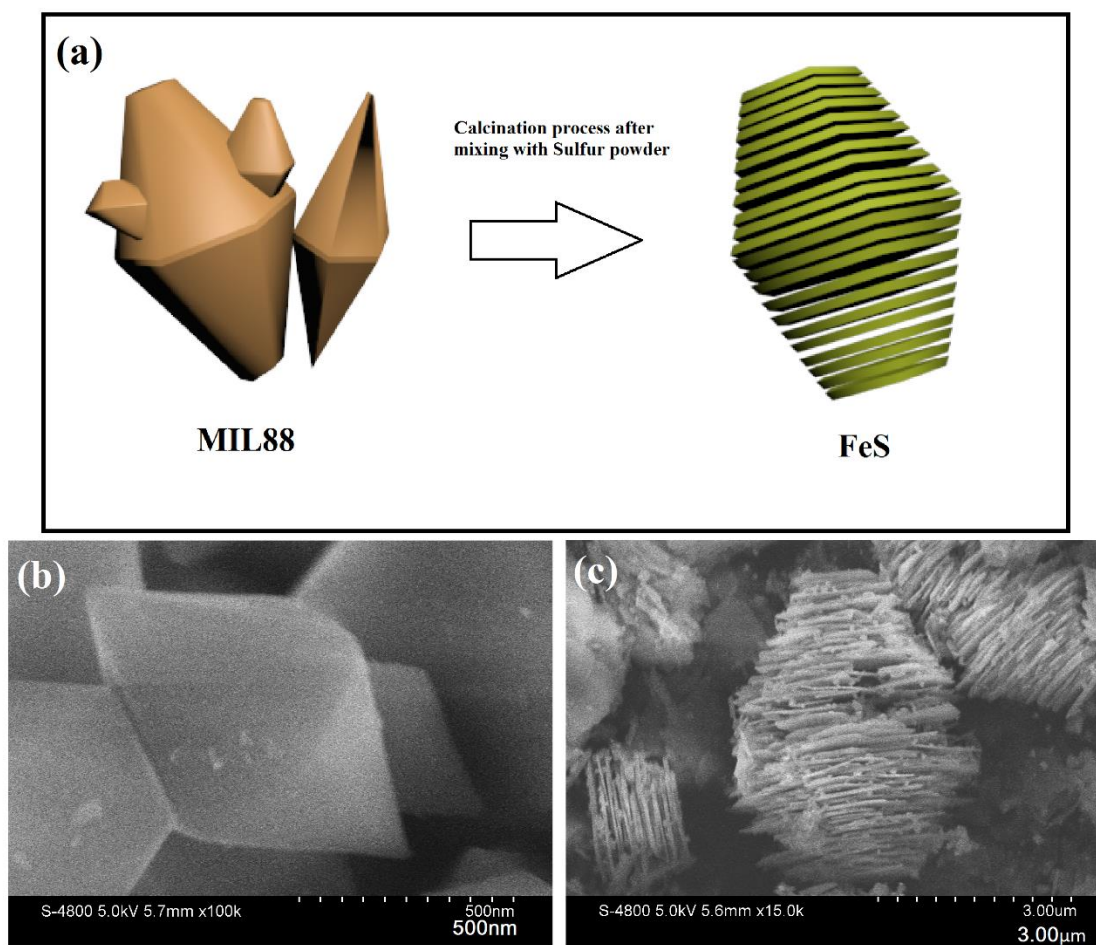

Figure 6-6-9 (a) schematic of the synthesis process of FeS_2 derived from MIL88; SEM images of (b) MIL88; (c) FeS_2.

XRD test was carried out to confirm the successful synthesis of Fe_xS_y and the phase purity. As shown in **Figure 6.10,** Fe_xS_y has a combination of three phases that were located in XRD peaks

Fe_xS_y consist of FeS, Fe_7S_8, Fe_9S_{11} phases at the same time indicating the need for more synthetic optimization of the process to design single phase iron sulfides.
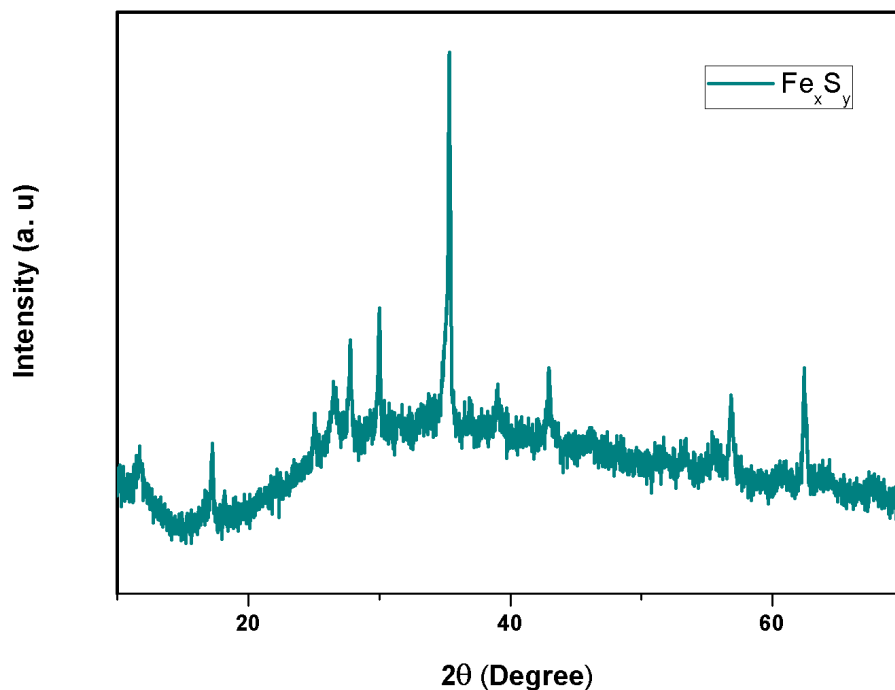
Figure 6-10 XRD pattern of FeS_2 derived from MIL88

The electrochemical evaluation of Fe_xS_y was performed using half-cell type LIBs and SIBs performing rate capability. As shown in **Figure 6.11**, the rate performance of Fe_xS_y is investigated by cycling the electrode at different current densities and calculate the corresponding specific capacity. As displayed in figure 5.8b, Fe_xS_y delivered discharge capacities of 209.2, 129.5, 104.6, 85.3 and 66.4mAh g^{-1} at current density of 100, 200, 300, 500, and 1000mA g^{-1}; respectively. Although the electrode shows high cycling stability, the capacity is relatively low in comparison to the theoretically and practically reported results. After working on this material for a long time, structure configuration is still challenging to guarantee reversible charging and discharging process using this material. The stable performance of every step through the rate test indicates high electrical conductivity which is attributed to the amount of carbon that Fe_xS_y have according to the TGA results.

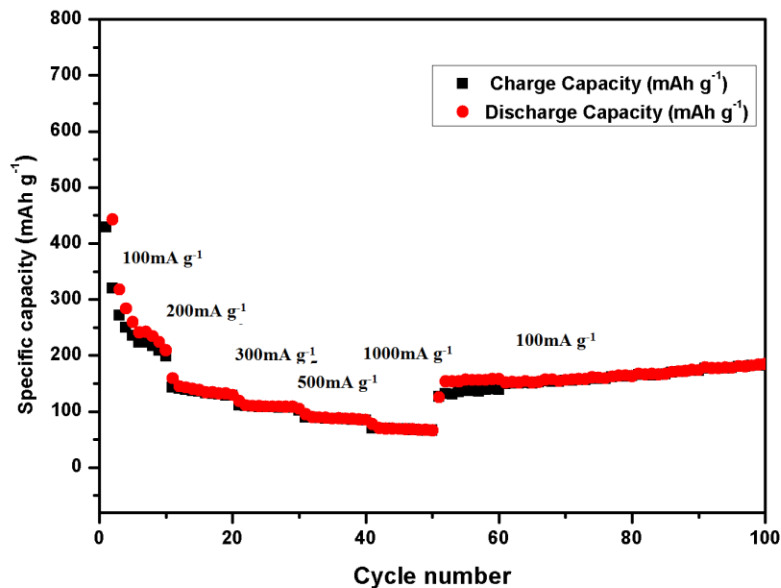Figure 6-6-11 (a) Cyclic voltammetry curve at 0.1mV S^{-1} scan rate of FeS_2 in LIBs half-cell; (b) Rate performance of FeS_2 at different current densities.

In a sodium-ion battery, Fe_xS_y cycling performance was measured firstly at a current density of 100 mAh g^{-1} in a potential range of 0-3V for 100 cycles. Initial capacity of 739.3mAh g^{-1} is delivered in the first cycles due to the first reaction between Na and Fe_xS_y and the formation of formation of solid electrolyte interphase (SEI) as result of the electrolyte decomposition. Then, the electrode experienced a sharp capacity drop after the first cycle which only retained a capacity of 21.84mAh g^{-1} after 100 cycles indicating substantial irreversible capacity fail as represented in **Figure 6.12a**. Rate performance was also investigated to determine the electrode rate capability in sodium storage. As shown in **Figure 6.12b**, Fe_xS_y exhibited discharge capacities of 61.45, 39.16, 29.32, 21.15 and 13.81mAh g^{-1} at current density of 100, 200, 300, 500, and 1000mA g^{-1}. This low performance shows the problem of this material which is in the structure stability since it suffers from serious volume change that affects its reliability during cycling. Another problem is the phase purity could attribute to undesirable reactions that lead to irreversible capacity fading. More characterization after electrochemical testing could help understanding this phenomenon.
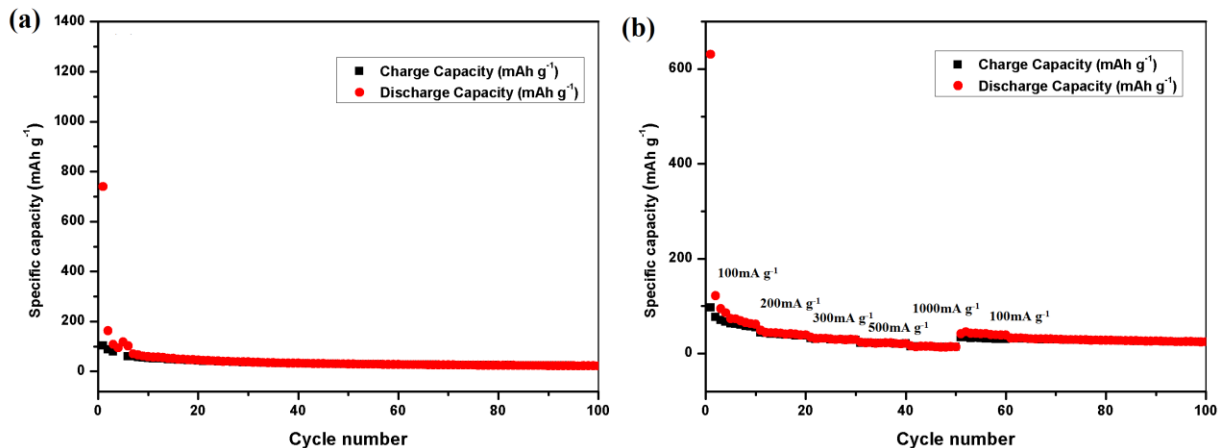
Figure 6-12(a) Cycling performance of Fe_xS_y at a current density of 100mA g^{-1}. (b) Rate performance of Fe_xS_y at Currents' different densities

To sum up this section, Fe_xS_y as a desirable material for battery applications was synthesized via calcination process using MIL-88 MOF template, and the physical characterization was carried out to confirm the success of the process. Electrochemical measurement s was performed by testing the product as anode material in LIBs and SIBs. The as-prepared Fe_xS_y showed very stable cycling and rate performance with low capacities demonstrating large capacity fading after the first cycle in both LIBs and SIBs. It was found that this structure needs more study and work before using as anode materials n order to improve lithium and sodium capacity. This could be done with more in-depth characterization and understanding of the nature and status of the phase and structure before and after cycling. Also, supporting the structure against the negative impact of volume change after cycling by using some protection coating or carbon matrix and improve the conductivity as well.

6.4. Conclusion

In this chapter, other metal sulfides including ZnS, SnS, and Fe_xS_y are synthesized and electrochemically examined as anode materials in LIBs and SIBs. ZnS performed high performance in both batteries with high stability after 100cycles. SnS_2 and F_xS_y tended to have some problems delivering high electrochemical performance due to the low capacity and severe volume change during cycling. Redetermining the structure ability to host Li^+ and Na^+ be urgently needed to be

studied before moving to electrochemical testing. Using some protection such as carbon coating could help accommodate the stress that results from volume expansion after the charging-discharging process. Carbon coating or composites helps to improve the stability by enhancing the electrical conductivity and the flexibility of the structure, so it provides more space for hosting a more significant amount of transporting ions.

References

1. Fu, Y., et al., *ZnS nanoparticles embedded in porous carbon matrices as anode materials for lithium-ion batteries.* RSC Adv., 2015. **5**(106): p. 86941-86944.

2. Mao, M., et al., *The structure control of ZnS/graphene composites and their excellent properties for lithium-ion batteries.* J. Mater. Chem. A, 2015. **3**(25): p. 13384-13389.

3. Wu, Q., et al., *One-pot synthesis of three-dimensional SnS2 hierarchitectures as anode material for lithium-ion batteries.* Journal of Power Sources, 2013. **239**: p. 89-93.

4. Wang, L., et al., *High-rate performance of SnS2 nanoplates without carbon-coating as anode material for lithium ion batteries.* Electrochimica Acta, 2013. **112**: p. 439-447.

5. Liu, W.L., et al., *Solvothermal synthesis of pyrite FeS2 nanocubes and their superior high rate lithium storage properties.* RSC Adv., 2014. **4**(90): p. 48770-48776.

6. Zheng, J., et al., *Facile synthesis of Fe3S4 hollow spheres with high-performance for lithium-ion batteries and water treatment.* J. Mater. Chem. A, 2014. **2**(46): p. 19882-19888.

7. Qin, W., et al., *ZnS nanoparticles embedded in reduced graphene oxide as high performance anode material for sodium-ion batteries.* Electrochimica Acta, 2016. **191**: p. 435-443.

8. Qu, B., et al., *Layered SnS2-reduced graphene oxide composite--a high-capacity, high-rate, and long-cycle life sodium-ion battery anode material.* Adv Mater, 2014. **26**(23): p. 3854-9.

9. Zhu, C., et al., *A General Strategy to Fabricate Carbon-Coated 3D Porous Interconnected Metal Sulfides: Case Study of SnS/C Nanocomposite for High-Performance Lithium and Sodium Ion Batteries.* Adv Sci (Weinh), 2015. **2**(12): p. 1500200.

10. Li, W., et al., *Pyrite nanocrystals: shape-controlled synthesis and tunable optical properties via reversible self-assembly.* Journal of Materials Chemistry, 2011. **21**(44): p. 17946.

11. Hu, Z., et al., *Pyrite FeS2 for high-rate and long-life rechargeable sodium batteries.* Energy Environ. Sci., 2015. **8**(4): p. 1309-1316.

12. Wu, C., J. Maier, and Y. Yu, *Generalizable Synthesis of Metal-Sulfides/Carbon Hybrids with Multiscale, Hierarchically Ordered Structures as Advanced Electrodes for Lithium Storage.* Adv Mater, 2016. **28**(1): p. 174-80.

13. Li, J., et al., *Mesoporous carbon anchored with SnS2 nanosheets as an advanced anode for lithium-ion batteries.* Electrochimica Acta, 2013. **111**: p. 862-868.

14. Jiang, X., et al., *In situ assembly of graphene sheets-supported SnS2 nanoplates into 3D macroporous aerogels for high-performance lithium ion batteries.* Journal of Power Sources, 2013. **237**: p. 178-186.

15. Sun, H., et al., *SnS2 nanoflakes decorated multiwalled carbon nanotubes as high performance anode materials for lithium-ion batteries.* Materials Research Bulletin, 2014. **49**: p. 319-324.

7. Chapter 6 Conclusion and Future work

In this study, ZIF-8 and ZIF-67 MOFs were synthesized, physically characterized and used as templates to design zinc sulfides and cobalt sulfides; respectively. MIL-88 synthesis process was also studied and optimized by changing some parameter to obtain uniform morphology. Metal sulfides derived from MOFs were successfully synthesized and tested for LIBs and SIBs applications. Cobalt sulfides were prepared using a ZIF-67 template and showed outstanding performance when tested as LIBs and SIBs anode. Zinc sulfides were designed by using ZIF-8 as a template and also was tested for LIBs ad SIBs electrochemical performance. Also, Tin sulfides were derived from tin-based MOFs and tested for electrochemical performance. Finally, Iron sulfides were successfully obtained and investigated for battery application after the optimization of its preparation method.

7.1. General conclusions

7.1.1. General conclusion of MOFs

ZIF-8 is successfully obtained with uniform rhombic dodecahedral structure and an average size of 200 nm via wet chemical method at room temperature. Similarly, ZIF-67 was successfully prepared using wet chemical process, and polyhedral particles with a particle size range between 100-200 nm were obtained. MIL-88 was studied, and its preparation process was optimized and emphasized due to the difficulty of the synthetic process to deliver pure phase and unique uniform structure. Different parameter including temperature, time, precursor weight ration or concentration in the solvent, different reaction mediums, and additives were investigated to achieve the uniform morphologies and structures. The optimized condition to obtain uniform MIL-88 with a soft surface and well defined geometric features are under the hydrothermal temperature of 140 ˚C for 20 hrs with the surfactant of F-127. The successful process was confirmed with XRD pattern and SEM study for physical and chemical characterization.

7.1.2. General conclusion of carbon coated Co_9S_8

Cobalt sulfides were synthesized via multi-stage rout using ZIF-67 as the template. Firstly, the wet chemical method was used to obtain Co_xS_y, and then an annealing process of the as-prepared cobalt sulfides was performed successfully using CVD approach. The product was confirmed by XRD test and SEM observation. Further characterization was carried out such as TGA, Raman, and BET to study the carbon content and its graphitization status as well as the surface area and the

material porosity. Unique properties of this material were discovered and then it was tested form electrochemical investigation for LIBs and SIBs electrode. This material showed very high capacity in LIBs and SIBs systems with very stable and high columbic efficiency cycling approving high capability of lithium and sodium storage and opening the door for its application in energy storage. Extended cycling up to 1000 cycles was performed, and high rate capability was observed via testing the anode at different current densities. Through this study, it was approved the affectedness' of using carbon coating to overcome the challenge of volume change effect and low electrical conductivity that directly impact the cycling performance of the battery and by delivering low capacity and poor cycling ability. Also, structures with high porosity have the advantages of providing short diffusion paths for charging ions and electrolyte accessibility to the electrode to obtain very stable reversible charging and discharging. All in all, cobalt sulfides with carbon coating is a very promising candidate as anode material for battery applications.

7.1.3. General conclusion of ZnS, SnS, and Fe_xS_y

Other metal sulfides including ZnS, SnS, and Fe_xS_y were synthesized and tested for batteries performances. ZnS-1 was prepared via calcination process using ZIF-8 as a template, and the similar structure was delivered and confirmed by XRD test and SEM images. ZnS-2 was also synthesized using the wet chemical method to compare the physical, chemical, and electrochemical properties of both materials. ZnS-1 and ZnS-2 were tested for LIBs, and SIBs anode and ZnS-1 show the best performance in comparison to ZnS-1 indicating better structure and chemical stability during the charging and discharging process.

SnS was synthesized using Sn-based MOF template was prepared in the previous study. XRD pattern showed that the obtained product is not pure phase SnS and peaks were indicated and indexed. For battery applications, SnS was employed as an anode in LIBs and SIBs and experiences low capacity and much capacity fading. These issues could be associated with the phase instability of the material that might lead to undesirable reactions that might prevent charging ions from maintaining the stable reversible reaction. Also, volume change is a severe problem that needs to be considered and solved by designing proper structures with high porosity and surface area or using some carbon composites to help to eliminate volume expansion effect.

Fe_xS_y was successfully obtained via calcination process of MIL-88 prepared before. XRD pattern showed multiphase material with FeS, Fe_7S_8, Fe_9S_{11} phases together indicating undesirable reactions or inaccurate synthetic parameters. The material was further examined in LIBs and SIBs anode and show stable performance with low capacity and massive capacity drop. This capacity drop is attributed to the chemical stability of the materials due to the multiphase status of the

product. Different phased material leads to more complicated reactions and unpredictable electrochemical performance which could be hard to understand and monitored.

7.2. Future work

MOFs are a new class of materials with unique characteristics such as high surface area and different structure orientations. This group of materials is a very strong candidate for energy storage applications by delivering other materials as using MOFs as templates for that. More effort is required for better understanding of the synthetic process and structure control of MOFs is urgently needed. Iron MOFs and Tin MOFs and their derived materials have not been very well understood and reported for battery applications.

For cobalt sulfides Co_9S_8, different carbon matrixes could be investigated such us a composite with graphene of carbon nanotubes could be studied which open the opportunity for more improvement.

Pristine ZnS-1 could be more studied and improved by using some coating techniques to upraise its capacity. SnS and Fe_xS_y need more investigation for better electrochemical capability. Several steps could be taken such as optimizing the structure by optimizing the synthesis process especially the reactant concentrations or weight ratio. Also, coating techniques and carbon composites with graphene, for instance, improve the electrical conductivity and rate capability. Using other coating techniques such as atomic layer deposition (ALD) molecular layer deposition (MLD) can be used to modify surface function and increase the mechanical strength against volume expansion consequences.

Curriculum Vitae

Name: **Ali Abdulla**

Post-secondary   **M.E.Sc. (2015-2017)**
Education and   Mechanical & Materials Engineering
Degrees: Western University
                        London, Canada

                        B.E.Sc. (2006-2010)
                        Mechanical Engineering
                        The University of Benghazi Benghazi, Libya

Scholarships: The ministry of Higher education of Libya funding for the Libyan-North
                        American Scholarship Program

Related Work   Teaching Assistant
Experience   Department of Mechanical Engineering
                        The University of Benghazi
                        2012-2014